Ultra-High Repetition Rate Terahertz Time-Domain Spectroscopy

Von der Fakultät für Ingenieurwissenschaften,
Abteilung Elektrotechnik und Informationstechnik
der Universität Duisburg-Essen

zur Erlangung des akademischen Grades

Doktor der Ingenieurwissenschaften

genehmigte Dissertation

von

Kevin Kolpatzeck
aus
Duisburg

Gutachter: Prof. Dr.-Ing. Andreas Czylwik
Gutachter: Prof. Dr. rer. nat. Martin Hofmann
Tag der mündlichen Prüfung: 29. April 2022

PREFACE

This thesis has come into being during my time as a research assistant at the Chair of Communication Systems (Fachgebiet Nachrichtentechnische Systeme, NTS) at the University of Duisburg-Essen under the supervision of Professor Andreas Czylwik.

For the last five years, I have been part of project S01, entitled "Beamforming concepts for THz frequencies", within the Collaborative Research Center / Transregio SFB/TRR 196 "Mobile material characterization and localization by electromagnetic sensing" ("MARIE"). During this time, the focus of my work has been on the development and evaluation of beam steering concepts for the terahertz frequency range, with a particular emphasis on concepts that are suitable for wideband applications. Since Professor Jan C. Balzer joined our group in late 2017, my work has been enriched by the topic of terahertz time-domain spectroscopy with monolithic light sources. My motivation within the last few years was to make a significant contribution to this field through the utilization of methods from the field of communications engineering. The findings I made are the topics of this work. While the majority of the thesis is focused on aspects of terahertz time-domain spectroscopy using monolithic mode-locked laser diodes, the circle is closed in the last chapter with a detailed discussion of the challenges of wideband beam steering at terahertz frequencies and promising solutions that take advantage of the spectral properties of mode-locked laser diodes.

I would like to express my gratitude towards several people who have been instrumental to the success of my work. First and foremost, I would like to thank my supervisor Professor Andreas Czylwik for his continued support of my work, for his mentoring, and for many thought-provoking discussions. I offer my thanks to Profes-

sor Martin Hofmann for his review of this thesis and for numerous helpful comments throughout its development. A special thanks goes to Professor Jan C. Balzer for introducing me to the topic of terahertz time-domain spectroscopy with monolithic light sources and for countless inspiring conversations that have shaped my work on the topic. Furthermore, I would like to thank all the colleagues and collaborators I had the please of working with throughout the years. Not only have they provided substantial technical input and support but also made my work truly enjoyable. I would particularly like to single out my colleague Xuan Liu. She has always had my back, and her creative and critical thinking have been invaluable in keeping my research on track and moving forward. I would also like to acknowledge Dr. Lars Häring, Dr. Stefan Bieder, and Dr. Thorsten Schultze for their academic as well as personal guidance throughout my time in the department.

Last but not least, I would like to express my gratitude towards my family. I thank my parents for always allowing me to follow my interests and for their support in all of my endeavors. I thank my sister for dozens of inspiring conversations on our joint car rides to work. I owe a lot to my late grandparents, who have been a tremendous source of support and motivation but sadly did not get the opportunity to see this thesis come to fruition. Most importantly, this work would not have been possible without the patience and unequivocal support of my fiancée Vivian Blazejewski.

Throughout my time working at the Chair of Communication Systems, I have published results of my work in several peer-reviewed journal and conference papers, and I have had the pleasure of presenting my work at several international conferences. Moreover, I have contributed to numerous more papers, most of which have arisen from the Collaborative Research Center “MARIE”. A categorized chronological list of all publications can be found on the following pages. I would like to thank all of my co-authors for their contributions, and I would like to show my appreciation to all the collaborators who have allowed me to gain an insight and take part in their work.

List of publications

Journal publications (first author)

[1] **K. Kolpatzeck**, X. Liu, K.-H. Tybussek, L. Häring, M. Zander, W. Rehbein, M. Moehrle, A. Czylwik, and J. C. Balzer, "System-theoretical modeling of terahertz time-domain spectroscopy with ultra-high repetition rate mode-locked lasers," *Opt. Express*, vol. 28, pp. 16 935–16 950, May 2020. doi: 10.1364/OE.389632

[2] X. Liu, **K. Kolpatzeck**, L. Häring, J. C. Balzer, and A. Czylwik, "Wideband beam steering concept for terahertz time-domain spectroscopy: Theoretical considerations," *Sensors*, vol. 20, 2020. doi: 10.3390/s20195568 *(shared first authorship)*

[3] **K. Kolpatzeck**, X. Liu, L. Häring, J. C. Balzer, and A. Czylwik, "Ultra-high repetition rate terahertz time-domain spectroscopy for micrometer layer thickness measurement," *Sensors*, vol. 21, 2021. doi: 10.3390/s21165389

Conference publications (first author)

[4] **K. Kolpatzeck**, L. Häring, and A. Czylwik, "Power budget analysis and optimization of photonic beamforming concepts for terahertz transmitters," in *2016 German Microwave Conference (GeMiC)*, 2016. doi: 10.1109/GEMIC.2016.7461542

[5] ——, "Phase control in photonically steered phased array transmitters by optical homodyne detection," in *2016 46th European Microwave Conference (EuMC)*, 2016. doi: 10.1109/EuMC.2016.7824538

[6] **K. Kolpatzeck**, X. Liu, L. Häring, and A. Czylwik, "System-theoretical modeling and analysis of phase control in a photonically steered terahertz phased array transmitter," in *2018 First International Workshop on Mobile Terahertz Systems (IWMTS)*, 2018. doi: 10.1109/IWMTS.2018.8454691

[7] **K. Kolpatzeck**, X. Liu, B. Friederich, D. Damyanov, L. Häring, T. Schultze, J. C. Balzer, and A. Czylwik, "Wideband radiation pattern measurement of terahertz antenna-integrated photodiodes by frequency-domain spectroscopy," in *2019 Second International Workshop on Mobile Terahertz Systems (IWMTS)*, 2019. doi: 10.1109/IWMTS.2019.8823782

[8] **K. Kolpatzeck**, S. Tonder, X. Liu, A. Czylwik, and J. C. Balzer, "Characterization and application of a commercially available laser diode in a thz system," in *2019 IEEE MTT-S International Microwave Workshop Series on Advanced Materials and Processes for RF and THz Applications (IMWS-AMP)*, 2019. doi: 10.1109/IMWS-AMP.2019.8880071

[9] **K. Kolpatzeck**, X. Liu, S. Nellen, B. Friederich, D. Damyanov, L. Häring, T. Schultze, B. Globisch, J. C. Balzer, and A. Czylwik, "Wideband radiation pattern simulation and measurement of a photodiode-based continuous-wave thz emitter," in *2019 44th International Conference on Infrared, Millimeter, and Terahertz Waves (IRMMW-THz)*, 2019. doi: 10.1109/IRMMW-THz.2019.8874041

[10] **K. Kolpatzeck**, M. Dedic, P. Krämer, X. Liu, V. Cherniak, K.-H. Tybussek, M. Zander, L. Häring, J. C. Balzer, and A. Czylwik, "Enhancement of terahertz spectra by model-driven spectral shaping of a mode-locked laser diode in a terahertz time-domain spectroscopy system," in *2020 45th International Conference on Infrared, Millimeter, and Terahertz Waves (IRMMW-THz)*, 2020. doi: 10.1109/IRMMW-THz46771.2020.9370728

[11] **K. Kolpatzeck**, X. Liu, K.-H. Tybussek, L. Häring, M. Zander, W. Rehbein, M. Moehrle, A. Czylwik, and J. C. Balzer, "Analytical modeling of terahertz time-domain spectroscopy with monolithic mode-locked laser diodes," in *2020 45th International Conference on Infrared, Millimeter, and Terahertz Waves (IRMMW-THz)*, 2020. doi: 10.1109/IRMMW-THz46771.2020.9370745

[12] **K. Kolpatzeck**, P. Krämer, X. Liu, T. Kubiczek, J. C. Balzer, and A. Czylwik, "Interferometric time synchronization of a terahertz time-domain spectroscopy system driven by a mode-locked laser diode," in *2021 46th International Conference on Infrared, Millimeter and Terahertz Waves (IRMMW-THz)*, 2021. doi: 10.1109/IRMMW-THz50926.2021.9566956

[13] **K. Kolpatzeck**, D. Damyanov, X. Liu, T. Schultze, J. C. Balzer, and A. Czylwik, "Imaging with an ultra-high repetition rate terahertz time-domain spectroscopy system driven by a mode-locked laser diode," in *2021 46th International Conference on Infrared, Millimeter and Terahertz Waves (IRMMW-THz)*, 2021. doi: 10.1109/IRMMW-THz50926.2021.9566909

Journal publications (co-author)

[14] K.-H. Tybussek, **K. Kolpatzeck**, F. Faridi, S. Preu, and J. C. Balzer, "Terahertz time-domain spectroscopy based on commercially available 1550 nm fabry–perot laser diode and eras:in(al)gaas photoconductors," *Applied Sciences*, vol. 9, 2019. doi: 10.3390/app9132704

[15] D. Damyanov, B. Friederich, M. Yahyapour, N. Vieweg, A. Deninger, **K. Kolpatzeck**, X. Liu, A. Czylwik, T. Schultze, I. Willms, and J. C. Balzer, "High resolution lensless terahertz imaging and ranging," *IEEE Access*, vol. 7, pp. 147 704–147 712, 2019. doi: 10.1109/ACCESS.2019.2934582

[16] X. Liu, L. Samfaß, **K. Kolpatzeck**, L. Häring, J. C. Balzer, M. Hoffmann, and A. Czylwik, "Terahertz beam steering concept based on a mems-reconfigurable reflection grating," *Sensors*, vol. 20, 2020. doi: 10.3390/s20102874

Conference publications (co-author)

[17] X. Liu, **K. Kolpatzeck**, L. Häring, and A. Czylwik, "Experimental validation of a phase control concept for photonically steered terahertz phased array transmitters at microwave frequencies," in *2018 First International Workshop on Mobile Terahertz Systems (IWMTS)*, 2018. doi: 10.1109/IWMTS.2018.8454685

[18] P. Lu, M. Steeg, **K. Kolpatzeck**, S. Dülme, B. Khani, A. Czylwik, and A. Stöhr, "Photonic assisted beam steering for millimeter-wave and thz antennas," in *2018 IEEE Conference on Antenna Measurements Applications (CAMA)*, 2018. doi: 10.1109/CAMA.2018.8530567

[19] B. Friederich, **K. Kolpatzeck**, X. Liu, T. Schultze, J. C. Balzer, A. Czylwik, and I. Willms, "Preprocessing for robust estimation of material parameters by continuous wave thz spectroscopy," in *2018 43rd International Conference on Infrared, Millimeter, and Terahertz Waves (IRMMW-THz)*, 2018. doi: 10.1109/IRMMW-THz.2018.8510417

[20] X. Liu, **K. Kolpatzeck**, A. Öztürk, B. Friederich, D. Damyanov, L. Häring, T. Schultze, J. C. Balzer, and A. Czylwik, "Wideband characterization of 3d printed thz rectangular dielectric waveguides by thz frequency-domain spectroscopy," in

2019 Second International Workshop on Mobile Terahertz Systems (IWMTS), 2019. doi: 10.1109/IWMTS.2019.8823720

[21] D. Damyanov, B. Friederich, J. Kohl, X. Liu, **K. Kolpatzeck**, T. Schultze, A. Czylwik, J. C. Balzer, and I. Willms, "Super-resolution restoration of low-resolution thz camera images," in *2019 Second International Workshop on Mobile Terahertz Systems (IWMTS)*, 2019. doi: 10.1109/IWMTS.2019.8823667

[22] S. C. Tonder, **K. Kolpatzeck**, X. Liu, S. Rumpza, A. Czylwik, and J. C. Balzer, "A compact thz quasi tds system for mobile scenarios," in *2019 Second International Workshop on Mobile Terahertz Systems (IWMTS)*, 2019. doi: 10.1109/IWMTS.2019.8823786

[23] M. Alissa, B. Friederich, **K. Kolpatzeck**, A. Czylwik, and T. Kaiser, "Experimental investigation of terahertz wave scattering by statistically controlled rough surfaces," in *2019 IEEE MTT-S International Microwave Workshop Series on Advanced Materials and Processes for RF and THz Applications (IMWS-AMP)*, 2019. doi: 10.1109/IMWS-AMP.2019.8880134

[24] X. Liu, **K. Kolpatzeck**, B. Friederich, D. Damyanov, L. Häring, T. Schultze, J. C. Balzer, and A. Czylwik, "Spectroscopic characterization of 3d printed thz rectangular polymer waveguides," in *2019 44th International Conference on Infrared, Millimeter, and Terahertz Waves (IRMMW-THz)*, 2019. doi: 10.1109/IRMMW-THz.2019.8873855

[25] D. Damyanov, B. Friederich, **K. Kolpatzeck**, X. Liu, M. Yahyapour, N. Vieweg, A. Deninger, T. Schultze, I. Willms, and J. C. Balzer, "High resolution lensless thz imaging with an ultrafast tds system," in *2019 44th International Conference on Infrared, Millimeter, and Terahertz Waves (IRMMW-THz)*, 2019. doi: 10.1109/IRMMW-THz.2019.8873898

[26] B. Friederich, D. Damyanov, J. Kohl, **K. Kolpatzeck**, X. Liu, T. Schultze, A. Czylwik, J. C. Balzer, and I. Willms, "High resolution image processing technique for the detection of metal entrapments based on a terahertz camera," in *2019 44th International Conference on Infrared, Millimeter, and Terahertz Waves (IRMMW-THz)*, 2019. doi: 10.1109/IRMMW-THz.2019.8874437

[27] A. Stöhr, P. Lu, T. Haddad, M. Steeg, J. Tebart, B. Sievert, A. Rennings, M. Hofmann, S. Dülme, **K. Kolpatzeck**, and A. Czylwik, "Microwave photonic mm-wave & thz beam steering for imaging, radar and communications," in *Asia Communications and Photonics Conference (ACPC) 2019*. Optical Society of America, 2019. ISBN 978-1-943580-70-5

[28] M. Zander, W. Rehbein, M. Moehrle, S. Breuer, D. Franke, M. Schell, **K. Kolpatzeck**, and J. C. Balzer, "High performance bh inas/inp qd and ingaasp/inp qw mode-locked lasers as comb and pulse sources," in *Optical Fiber Communication Conference (OFC) 2020*. Optical Society of America, 2020. doi: 10.1364/OFC.2020.T3C.4

[29] D. Damyanov, B. Friederich, **K. Kolpatzeck**, X. Liu, A. Czylwik, T. Schultze, I. Willms, and J. C. Balzer, "A novel approach for lensless high-resolution terahertz imaging (Conference Presentation)," in *Terahertz Photonics*, M. Jarrahi, S. Preu, and D. Turchinovich, Eds., vol. 11348, International Society for Optics and Photonics. SPIE, 2020. doi: 10.1117/12.2554007

[30] X. Liu, C. Geng, X. Guo, **K. Kolpatzeck**, L. Häring, J. C. Balzer, and A. Czylwik, "Design and characterization of 3d printed polymer terahertz multimode interference couplers," in *2020 45th International Conference on Infrared, Millimeter, and Terahertz Waves (IRMMW-THz)*, 2020. doi: 10.1109/IRMMW-THz46771.2020.9370927

[31] D. Damyanov, A. Batra, B. Friederich, **K. Kolpatzeck**, X. Liu, T. Kaiser, T. Schultze, and J. C. Balzer, "High resolution vna thz imaging for large distances," in *2020 45th International Conference on Infrared, Millimeter, and Terahertz Waves (IRMMW-THz)*, 2020. doi: 10.1109/IRMMW-THz46771.2020.9370443

[32] J. Schorlemer, **K. Kolpatzeck**, J. C. Balzer, A. Czylwik, I. Rolfes, and J. Barowski, "Efficient frequency domain sampling schemes for thz sar systems," in *2021 Fourth International Workshop on Mobile Terahertz Systems (IWMTS)*, 2021. doi: 10.1109/IWMTS51331.2021.9486808

[33] V. Cherniak, **K. Kolpatzeck**, X. Liu, K. Tybussek, D. Damyanov, T. Schultze, A. Czylwik, and J. C. Balzer, "Compact and inexpensive terahertz system driven by monolithically integrated commercial light sources," in *2021 46th International*

Conference on Infrared, Millimeter and Terahertz Waves (IRMMW-THz), 2021. doi: 10.1109/IRMMW-THz50926.2021.9567637

[34] X. Liu, L. Schmitt, **K. Kolpatzeck**, M. Hoffmann, J. C. Balzer, and A. Czylwik, "Configuration of a mems-based terahertz reflectarray using a genetic algorithm," in *2021 46th International Conference on Infrared, Millimeter and Terahertz Waves (IRMMW-THz)*, 2021. doi: 10.1109/IRMMW-THz50926.2021.9567102

[35] X. Liu, **K. Kolpatzeck**, L. Häring, J. C. Balzer, and A. Czylwik, "Beam steering for terahertz time-domain spectroscopy using optical ring resonators," in *2021 46th International Conference on Infrared, Millimeter and Terahertz Waves (IRMMW-THz)*, 2021. doi: 10.1109/IRMMW-THz50926.2021.9567221

CONTENTS

INTRODUCTION

The discovery and comprehension of electromagnetic waves is one of the greatest scientific achievements of the last millennium. Enabled by the pioneering work of Maxwell, Heaviside, Hertz, and their contemporaries in the late 19^{th} century, the electromagnetic spectrum has through the course of the 20^{th} century become yet another resource for humankind to make use of. Although the propagation of all electromagnetic waves is described by a single set of partial differential equations, the way they interact with matter strongly depends on their wavelength and the associated photon energy. While only a small fraction of the electromagnetic spectrum is perceptible by humans as visible light, the frequency range that has been technically exploited covers nearly twenty orders of magnitude. It goes all the way from extremely low frequency (ELF) submarine communication systems operating at only a few hertz up to gamma ray (γ-ray) sources for cancer treatment working at several exahertz. Due to the large variety of practical applications, it is nowadays hard to value any particular portion of the electromagnetic spectrum above the rest. However, it is fair to say that the technological accessibility and the favorable propagation characteristics of the microwave and the infrared range have given them a special role in the second half of the 20^{th} century as well as today. Interestingly enough, despite their spectral proximity, the microwave and infrared range have historically been treated quite independently. This is mostly due to the different technological means by which they have been accessed, but also because of the different ways they interact with matter.

From microwave and infrared to terahertz waves

Microwaves, that is to say waves with a frequency that is roughly in the range from 300 MHz to 300 GHz and a wavelength that is roughly in the range from 1 mm to 1 m, are typically electronically generated by oscillator circuits. These oscillators generate their required power gain in an active electronic device, such as a semiconductor diode or transistor. These devices are sometimes called "transit-time" devices because power is transferred into the microwave band as carriers transit through the device. Consequently, the maximum operating frequency is limited by the time the carriers spend transiting through the device. Microwaves travel primarily through the line of sight, but they are also reflected by large pieces of infrastructure and in some cases diffract around smaller objects. These properties, along with the large available bandwidth, have made them the basis of today's wireless communication systems. The superior non-line-of-sight propagation characteristics at the lower end of the microwave range up to about 6 GHz have made it the frequency range of choice for wideband mobile communication standards. The adjacent bands are frequently used for satellite communications, and the upper bands up to about 100 GHz – typically called the millimeter-wave range – are a popular choice for point-to-point wireless communication links. Moreover, the microwave frequency range above about 60 GHz is widely used for radar applications with centimeter-level accuracy. A fairly novel use of that frequency range is three-dimensional sub-surface imaging in security applications.

The infrared range is located between the upper end of the microwave range and the lower end of the visible portion of the electromagnetic spectrum. It encompasses roughly the frequency range from 300 GHz to 400 THz or the wavelength range from 750 nm to 1 mm. Infrared waves are typically electronically generated by so-called "transition" devices, such as light-emitting diodes or lasers. In these devices, power is transferred into the infrared range by band transitions of carriers in a semiconductor material. Consequently, the minimum frequency that can be generated is determined by the minimum achievable band gap of the semiconductor structure. Unlike microwaves, infrared radiation travels almost exclusively through the line of sight and is efficiently reflected only by smooth surfaces. Moreover, it diffracts only around tiny objects, and atmospheric attenuation limits the usable transmission distance in large portions of the infrared range. Nonetheless, the applications of infrared waves are as numerous as the frequency range is wide. They include thermal sensing, spectroscopy,

metrology, meteorology, and optical communications. Fiber-optic communication systems in the 1550 nm band have a particular role, as they build the backbone of today's broadband digital communication systems.

The border region of the microwave and the infrared range is commonly referred to as the *terahertz* or *sub-millimeter wave* range. It is loosely defined as the frequency range from 100 GHz to 10 THz. Due to the aforementioned limitations of transit-time and transition devices, the terahertz range is notoriously difficult to conquer and has largely remained no-man's-land until the end of the 20^{th} century. This circumstance has led to the coining of the phrase "terahertz gap". Curiously, this "gap" is – on a logarithmic scale – located roughly in the center of the technically exploited portion of the electromagnetic spectrum. Most importantly, the terahertz range shares a lot of the properties of microwaves and infrared radiation, thus opening up a wide palette of possible applications. Terahertz waves have a wavelength that is almost as short as that of far-infrared radiation, but are capable of penetrating dielectric materials at least a few millimeters deep. This can make them a powerful tool for high-resolution sub-surface imaging. At the same time, the bandwidth available in the terahertz range is ten times that available in the microwave range. This can enable not only ultra-high data-rate wireless communication links but also radar systems with sub-millimeter resolution. Moreover, a few chemicals – particularly gases – exhibit distinct spectral features in the terahertz range that can be used for material detection.

Over the last few decades, a lot of scientific effort has been put into gaining access to the terahertz range. On the microwave side, electronic sources and detectors with ever-increasing cutoff frequencies have been developed. These include transistor- and diode-based fundamental oscillators and detectors as well as frequency multipliers and sub-harmonic mixers. Although electronic devices operating up to 2 THz have been reported, the output power as well as the realizable device complexity decrease steadily with increasing frequency. On the infrared side, quantum cascade lasers have allowed the laser concept to be extended just below 1 THz. However, most of these approaches have in common that they rely on a resonant element and thus exhibit a comparatively small relative bandwidth.

Photonic terahertz spectroscopy

This thesis focuses on systems that enable applications which utilize a wide spectral range at terahertz frequencies. The generation and coherent detection of terahertz waves across large portions of the terahertz range is only afforded by photonic terahertz spectroscopy systems. These operate on the principle of generating a sufficiently wide spectrum in a higher frequency band – typically the near-infrared or short-wavelength infrared range – with one or more lasers and translating this spectrum into the terahertz range with a suitable non-linear device. Most state-of-the-art systems use a pair of semiconductor devices driven by the same laser-generated infrared signal to emit and coherently detect terahertz radiation.

For many years now, these photonic terahertz spectroscopy systems have been the work horses in terahertz labs around the world due to their wide bandwidth, high dynamic range, room-temperature operation, ease of use, and relative maturity. However, except for a handful of lighthouse applications, they have yet failed to make a successful transition from the lab into the field. The reasons for this include the high cost of the systems (typically $> 50000\,€$), their relative bulk (larger than a shoe box), and their mechanical sensitivity. Undoubtedly, another reason is the simple fact that a new technology needs to offer significant advantages over existing solutions to achieve market penetration.

There are two groups of photonic terahertz spectroscopy systems: Terahertz *frequency-domain* spectroscopy (THz-FDS) and terahertz *time-domain* spectroscopy (THz-TDS). As their names suggest, the difference between them lies in the domains in which they generate and detect terahertz spectra. THz-FDS systems emit and detect monochromatic terahertz radiation, i.e. one frequency at a time, so that spectral information is obtained by scanning that frequency. THz-TDS systems emit pulsed terahertz radiation, i.e. all frequencies at once, so that spectral information is obtained by sampling the terahertz pulses in the time domain using an optical delay unit (ODU).

Ultra-high repetition rate terahertz time-domain spectroscopy

The properties of a THz-TDS system are largely determined by the infrared source – commonly called the "light source" – that drives the system. On the one hand, its spectral and coherence properties dictate the performance in the terahertz domain. On the

other hand, the light source is a major contributor to the cost, bulk, and complexity of the overall system. For these reasons, the last few decades have seen a quest for light sources that improve any one of these parameters. State-of-the-art THz-TDS systems typically use a fiber laser as their light source. These systems readily achieve a bandwidth of several terahertz and a peak dynamic range that exceeds 100 dB with a pulse repetition rate in the range of a few hundred megahertz. However, while fiber lasers are comparatively compact and robust compared to previously used light sources, they are still optically pumped and lack any potential for monolithic integration. These shortcomings have set off investigations into suitable monolithic light sources for THz-TDS.

Particular promising candidates are monolithic mode-locked laser diodes (MLLDs). Like fiber lasers, MLLDs exhibit a fixed phase relationship between their longitudinal modes. The quantitative difference that sets an MLLD-driven THz-TDS system apart from a fiber laser-driven system is a much larger free spectral range (FSR) due to the short on-chip cavity. Typical values are of the order of a few ten gigahertz. In the time domain, this causes a correspondingly high pulse repetition rate. Because of this property, this approach has recently been named *ultra-high repetition rate terahertz time-domain spectroscopy* (UHRR-THz-TDS). The UHRR-THz-TDS approach presents numerous unique opportunities and challenges, whose exploitation and overcoming, respectively, enable a quantum leap in the practical application of terahertz spectroscopy systems. This requires a thorough understanding of the concept and a comprehensive investigation of the UHRR-THz-TDS approach. This thesis gives a substantial contribution in this field.

Objectives and structure of this thesis

This thesis has three main objectives. The first objective is *properly placing UHRR-THz-TDS in the context of photonic terahertz spectroscopy systems*. To this end, an overview of the field of photonic terahertz spectroscopy is given in **Chapter 1**. This includes descriptions of the operating principles of THz-FDS and THz-TDS as well as brief recapitulations of their development. Moreover, it contains a recount of the work that has been done on monolithic light sources for THz-TDS. A detailed comparison between the conventional THz-TDS approach and THz-TDS using different monolithic light sources is provided in **Chapter 3**. For this comparison, we take a look at the spectral

and coherence properties of the light sources and analyze their practical implications. This analysis yields a much-needed comparison of the suitability of the various light sources for different applications and systems.

The second objective of this thesis is *furthering the understanding of UHRR-THz-TDS*. For this purpose, a thorough system-theoretical analysis of the UHRR-THz-TDS approach is presented for the first time in **Chapter 2**. This analysis starts with the development of a simple yet accurate system-theoretical model of an UHRR-THz-TDS system. This model describes the relationship between the complex optical spectrum of the MLLD and the measured terahertz spectrum. We then draw important conclusions from the system-theoretical model regarding the influence of pulse chirp and the significance of the number of laser modes. Finally, experimental results that verify the validity of the system-theoretical model are shown.

Based on this improved understanding, the third objective of this work is *showcasing promising new solutions for wideband terahertz systems enabled by the UHRR-THz-TDS concept*. A new model-driven approach for shaping the terahertz spectrum by shaping the optical spectrum of the MLLD is proposed in **Chapter 4**. Numerical results as well as first experimental results are presented, and limitations of the approach are discussed. **Chapter 5** is concerned with errors caused by the optical delay unit in a THz-TDS system. Following a brief look at the state of the art, a novel interferometric solution for accurately reconstructing the delay axis in an UHRR-THz-TDS system with minimal hardware effort is presented. Based on this solution, algorithms for the precise synchronization and linearization of the delay axis and efficient processing of the measurement data are introduced. Finally, **Chapter 6** touches on the topic of beam steering for UHRR-THz-TDS. Some of the fundamental challenges of beam steering for wideband terahertz systems are discussed. It is then shown how the frequency-discrete nature of UHRR-THz-TDS makes a new simplified variation of photonic true time delay (TTD) beam steering feasible. To round this off, it is demonstrated that non-uniform spatial distributions of the elements of a linear antenna array can provide good performance across the entire frequency range of an UHRR-THz-TDS system.

In summary, this thesis presents several **contributions to the state of the art**, including

- a simple yet accurate system-theoretical model of an UHRR-THz-TDS system,
- a new model-driven approach for shaping the detected terahertz spectrum by purposefully modifying the optical spectrum of the MLLD,
- a novel interferometric solution for accurately reconstructing the delay axis,
- efficient algorithms for processing measurement data acquired with an UHRR-THz-TDS system,
- the first utilization of the UHRR-THz-TDS approach for synthetic aperture radar imaging,
- a novel *quasi*-true time delay concept that paves the way for wideband beam steering with an UHRR-THz-TDS system, and
- promising antenna array element distributions that provide good performance over a relative bandwidth of a decade.

CHAPTER

ONE

FUNDAMENTALS OF PHOTONIC TERAHERTZ SPECTROSCOPY

As mentioned in the introduction, photonic terahertz spectroscopy systems with semiconductor emitters and detectors have been the work horses in terahertz labs around the world for many years. In this chapter, the two main groups of systems, i.e. *frequency-domain* and *time-domain* spectroscopy systems, are discussed. Their operating principles are summarized and a few noteworthy historical steps on the way from first demonstrations to the state of the art are discussed.

1.1 Terahertz frequency-domain spectroscopy

1.1.1 System description and operating principle

The most simple version of a fiber-coupled terahertz frequency-domain spectroscopy (THz-FDS) setup is depicted in Figure 1.1. It is the prototype for any more sophisticated setup and shall aid a brief description of the operating principle in this section. The spectrometer is driven by two single-mode infrared lasers emitting harmonic sig-

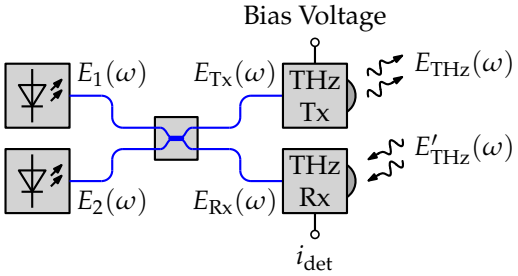

Figure 1.1: Simplified block diagram of a THz-FDS setup. Blue lines indicate polarization-maintaining fibers. Black lines indicate electrical connections.

nals at the angular frequencies ω_1 and ω_2, respectively [1]. The two harmonic signals are combined in a fused-fiber coupler, making sure that both lasers are linearly polarized and that their polarizations are accurately aligned. This is preferably accomplished by using polarization-maintaining (PM) fibers throughout the setup and aligning the polarization of the two lasers with the slow axis of said PM fibers. The same fused-fiber coupler that combines the two optical signals is used to split the combined signal into two paths. One path feeds the terahertz emitter (Tx), the other path feeds the terahertz detector (Rx). The emitter is either a biased antenna-integrated photodiode or a biased photoconductive antenna (PCA). The detector is typically an unbiased PCA. By photomixing, the terahertz emitter converts the beat of the two infrared signals into a terahertz wave at the difference frequency of the two lasers. The terahertz wave is transmitted via a radio-frequency (RF) channel and is incident on the terahertz detector. In the photoconductive terahertz detector, the incident terahertz wave is mixed with the beat of the two infrared signals.

The measured quantity in the THz-FDS system is the direct photocurrent generated in the photoconductive detector. This photocurrent can be easily calculated using simple models of the physical components in the setup. The infrared spectra emitted by the two lasers can be written as

$$E_1(\omega) = E_1 \cdot [\delta(\omega + \omega_1) + \delta(\omega - \omega_1)] \tag{1.1}$$

[1] The term "mode" can in principle indicate either longitudinal or transversal modes. In this thesis, it is generally used to indicate *longitudinal* laser modes. In this case, the term "single-mode" specifically indicates a single longitudinal mode synonymous with "single-frequency". The existence of a single transversal mode is assumed.

and

$$E_2(\omega) = E_2 \cdot [\delta(\omega + \omega_2) + \delta(\omega - \omega_2)] \ , \tag{1.2}$$

respectively, where E_1 and E_2 are the normalized amplitudes of the electric fields emitted by the two lasers. The amplitudes are normalized so that their squares are equal to the optical powers. Taking into account the intrinsic phase shifts introduced by the fused-fiber coupler while neglecting the time delays introduced by the optical fibers, the infrared spectra at the emitter respectively detector are

$$E_{\mathrm{Tx}}(\omega) \propto E_1 \cdot [\delta(\omega + \omega_1) + \delta(\omega - \omega_1)] + E_2 \cdot [-\mathrm{j}\delta(\omega + \omega_2) + \mathrm{j}\delta(\omega - \omega_2)] \tag{1.3}$$

and

$$E_{\mathrm{Rx}}(\omega) \propto \mathrm{j}E_1 \cdot [-\mathrm{j}\delta(\omega + \omega_1) + \mathrm{j}\delta(\omega - \omega_1)] + E_2 \cdot [\delta(\omega + \omega_2) + \delta(\omega - \omega_2)] \ . \tag{1.4}$$

The terahertz current generated in the antenna-integrated photodiode is proportional to the low-pass filtered instantaneous optical power incident on the photodiode. In the time domain, the instantaneous optical power is proportional to the squared magnitude of the electric field. Thus, in the frequency domain it can be written as

$$P_{\mathrm{Tx}}(\omega) \propto E_{\mathrm{Tx}} * E_{\mathrm{Tx}} \ , \tag{1.5}$$

where $*$ denotes the convolution operator. The instantaneous optical power contains five spectral components that can be categorized into

$$\begin{aligned} P_{\mathrm{Tx}}(\omega) \propto & \underbrace{2 \cdot \left(E_1^2 + E_2^2\right) \cdot \delta(\omega)}_{\text{average power}} \\ & + \underbrace{2 \cdot E_1 E_2 \cdot \{-\mathrm{j}\delta[\omega + (\omega_2 - \omega_1)] + \mathrm{j}\delta[\omega - (\omega_2 - \omega_1)]\}}_{\text{difference-frequency oscillation}} \\ & + \underbrace{2 \cdot E_1 E_2 \cdot \{-\mathrm{j}\delta[\omega + (\omega_2 + \omega_1)] + \mathrm{j}\delta[\omega - (\omega_2 + \omega_1)]\}}_{\text{sum-frequency oscillation}} \\ & + \underbrace{E_1^2 \cdot \delta[\omega + 2\omega_1] + \delta[\omega - 2\omega_1] + E_2^2 \cdot \delta[\omega + 2\omega_2] + \delta[\omega - 2\omega_2]}_{\text{double-frequency oscillation}} \ . \end{aligned} \tag{1.6}$$

Due to its low-pass behavior, only the average power and the difference-frequency oscillation can contribute to the photocurrent generated in the antenna-integrated photodiode. By tuning the frequencies of the lasers, the angular difference frequency $\Delta\omega = \omega_2 - \omega_1$ can be made to be in the terahertz frequency range. The electric field observed in the far field of the terahertz emitter contains only the terahertz-frequency oscillation

$$E_{\mathrm{THz}}(\omega) \propto E_1 E_2 \cdot \mathrm{j} \cdot [-\delta(\omega + \Delta\omega) + \delta(\omega - \Delta\omega)] \cdot H_{\mathrm{Tx}}(\omega) \,, \tag{1.7}$$

where $H_{\mathrm{Tx}}(\omega)$ describes the frequency response of the terahertz emitter [2]. After transmission through the RF channel, the electric field at the terahertz detector is

$$E'_{\mathrm{THz}}(\omega) \propto E_1 E_2 \cdot [-\delta(\omega + \Delta\omega) + \delta(\omega - \Delta\omega)] \cdot H_{\mathrm{Tx}}(\omega) \cdot H_{\mathrm{channel}}(\omega) \,, \tag{1.8}$$

where $H_{\mathrm{channel}}(\omega)$ is the transfer function of the RF channel. In the photoconductive terahertz detector, the conductivity of the photoconductor is proportional to the low-pass filtered instantaneous optical power in the same way as the photocurrent in the terahertz emitter. The terahertz wave that is incident on the PCA induces a voltage at the terminals of the photoconductor. The direct photocurrent that is generated in the photoconductor is proportional to the time average of the product of the instantaneous conductivity and the instantaneous voltage at its terminals. In the frequency domain, it can be written as

$$I_{\mathrm{det}}(\omega) \propto \left\{ P_{\mathrm{Rx}}(\omega) * E'_{\mathrm{THz}}(\omega) \cdot H_{\mathrm{Rx}}(\omega) \right\} \cdot H_{\mathrm{LP}}(\omega) \,, \tag{1.9}$$

where $P_{\mathrm{Rx}}(\omega)$ is the Fourier transform of the low-pass filtered instantaneous optical power at the detector. The transfer function $H_{\mathrm{Rx}}(\omega)$ considers the terahertz frequency response of the detector [3], and $H_{\mathrm{LP}}(\omega)$ is the transfer function of a low-pass filter with an angular cutoff frequency that is much lower than $\Delta\omega$. By calculating $P_{\mathrm{Rx}}(\omega)$ similar to Equation (1.6), we get

$$\begin{aligned} I_{\mathrm{det}}(\omega) \propto H_{\mathrm{LP}}(\omega) \cdot \Big\{ & E_1 E_2 \cdot [-\delta(\omega + \Delta\omega) + \delta(\omega - \Delta\omega)] \\ & * E_1 E_2 \cdot [-\delta(\omega + \Delta\omega) + \delta(\omega - \Delta\omega)] \cdot H_{\mathrm{Tx}}(\omega) \cdot H_{\mathrm{channel}}(\omega) \cdot H_{\mathrm{Rx}}(\omega) \Big\} \,. \end{aligned} \tag{1.10}$$

[2] In literature, the antennas of the terahertz emitter and detector are commonly approximated as electric dipoles [36]. The electric field observed in the far field of an electric dipole is proportional to the first time derivative of the current flowing in the dipole [37]. The corresponding term $\mathrm{j}\omega$ is obliquely included in the transfer function $H_{\mathrm{Tx}}(\omega)$.

[3] Analogous to footnote 2, the term $(\mathrm{j}\omega)^{-1}$ is obliquely included in the transfer function $H_{\mathrm{Rx}}(\omega)$.

The transfer functions of the emitter, detector, and RF channel can be combined into a transfer function that describes the complete terahertz system:

$$\begin{aligned} H_{\mathrm{THz}}(\omega) &= H_{\mathrm{Tx}}(\omega) \cdot H_{\mathrm{channel}}(\omega) \cdot H_{\mathrm{Rx}}(\omega) \\ &= |H_{\mathrm{THz}}(\omega)| \cdot \mathrm{e}^{\mathrm{j}\varphi_{\mathrm{THz}}(\omega)} \,. \end{aligned} \tag{1.11}$$

We thus get

$$\begin{aligned} I_{\mathrm{det}}(\omega) &\propto H_{\mathrm{LP}}(\omega) \cdot \Big\{ E_1^2 E_2^2 \cdot |H_{\mathrm{THz}}(\Delta\omega)| \cdot [-\delta(\omega + \Delta\omega) + \delta(\omega - \Delta\omega)] \\ &\qquad * \left[-\delta(\omega + \Delta\omega) \cdot \mathrm{e}^{-\mathrm{j}\varphi_{\mathrm{THz}}(\Delta\omega)} + \delta(\omega - \Delta\omega) \cdot \mathrm{e}^{\mathrm{j}\varphi_{\mathrm{THz}}(\Delta\omega)} \right] \Big\} \\ &\propto E_1^2 E_2^2 \cdot |H_{\mathrm{THz}}(\Delta\omega)| \cdot \delta(\omega) \cdot \left[\mathrm{e}^{-\mathrm{j}\varphi_{\mathrm{THz}}(\Delta\omega)} + \mathrm{e}^{\mathrm{j}\varphi_{\mathrm{THz}}(\Delta\omega)} \right] \\ &\propto E_1^2 E_2^2 \cdot |H_{\mathrm{THz}}(\Delta\omega)| \cdot \delta(\omega) \cdot \cos\left[\varphi_{\mathrm{THz}}(\Delta\omega)\right] \,. \end{aligned} \tag{1.12}$$

The photocurrent that can be measured at the output of the photoconductive detector can thus be written as a function of the difference frequency of the two lasers in the form of

$$i_{\mathrm{det}}(\Delta\omega) \propto E_1^2 E_2^2 \cdot |H_{\mathrm{THz}}(\Delta\omega)| \cdot \cos\left[\varphi_{\mathrm{THz}}(\Delta\omega)\right] \,. \tag{1.13}$$

Assuming that the average powers of both lasers are constant, the measured current depends linearly on the magnitude of the transfer function of the terahertz system and sinusoidally on its phase. Theoretically, the magnitude of the transfer function could thus be determined with a frequency resolution that is only limited by the tuning accuracy of the lasers. However, in reality the term $\cos\left[\varphi_{\mathrm{THz}}(\Delta\omega)\right]$ complicates the evaluation. Assuming the simplest RF channel consisting of a free-space path of length L between emitter and detector, we get

$$i_{\mathrm{det}}(\Delta\omega) \propto E_1^2 E_2^2 \cdot |H_{\mathrm{THz}}(\Delta\omega)| \cdot \cos\left[\frac{-\Delta\omega L}{c_0} + \varphi_{\mathrm{THz},0}(\Delta\omega)\right] \,, \tag{1.14}$$

where $-\Delta\omega L/c_0$ describes the phase shift introduced by the air channel and $\varphi_{\mathrm{THz},0}(\Delta\omega)$ describes any further frequency-dependent contributions to the phase of the transfer function. For a given length L, the measured photocurrent thus oscillates with the terahertz frequency, with maxima (respectively minima) being c_0/L apart in the frequency

domain. As the frequency is scanned, a *fringe pattern* can be observed in the photocurrent. It can be shown that the difference between the optical path length between the fiber coupler and the terahertz emitter and the optical path length between the fiber coupler and the terahertz detector can be included in the total length L. The impacts these theoretical result have on the use of the system have been described in good detail in a large number of publications. Different approaches have been proposed to determine both the magnitude and phase of the transfer function of a sample that is placed in the terahertz path.

The most straightforward approach uses an optical delay unit (ODU) in the optical path to the detector [38, 39]. In this case, L is varied to scan and analyze the fringe pattern. An all-fiber realization of this concept uses a fiber stretcher to vary the optical path lengths [40]. Another approach uses optical phase shifters to achieve the same goal [41]. Besides these solutions, Roggenbuck et al. [42] have demonstrated that the magnitude and phase of the transfer function of a sample that is placed in the terahertz path can be determined without any additional means by comparing the magnitudes and locations of the maxima of the fringe patterns that are observed with and without the sample, respectively, albeit with a poor frequency resolution. Recent works have demonstrated another interesting approach. By having slightly different angular difference frequencies $\Delta\omega_{\mathrm{Tx}}$ and $\Delta\omega_{\mathrm{Rx}}$ at the emitter and detector, respectively, the homodyne detection in the PCA turns into a heterodyne detection, so that magnitude and phase can be directly accessed. The frequency difference is realized either by modulation in the optical domain [43, 44] or very elegantly by combining fast tuning of one of the lasers with a small path length difference between the transmit and receive path [45, 46].

1.1.2 From first demonstrations to the state of the art

The experimental groundwork for THz-FDS was laid in the middle of the 1990s. In 1994, Brown et al. [47] demonstrated terahertz generation by photomixing in low-temperature-grown (LTG) gallium arsenide (GaAs). They did so by beating a fixed-frequency and a tunable-frequency titanium-sapphire (Ti:sapphire, Ti:Al_2O_3) laser in a LTG-GaAs photomixer. The measured radiated terahertz power was close to constant in the range from 100 GHz to 300 GHz at a value of about 10 µW and showed a roll-off of 12 dB per octave above that frequency. The highest-frequency signal that was mea-

sured was at a frequency of 3.8 THz with a power of roughly 200 fW. In the following year, McIntosh et al. [48] made the photomixing terahertz source entirely solid-state by replacing the Ti:sapphire lasers with distributed-Bragg-reflector (DBR) laser diodes, and they increased the 3 dB-bandwidth from 405 to 650 GHz by improving the photomixer design.

In 1998, Verghese et al. [49] extended this concept to the generation and coherent detection with two photomixers. They constructed the prototype for the coherent THz-FDS system explained in the previous section. The system was demonstrated up to a frequency of 2 THz. In 2002, Siebert et al. [50] applied this concept to transmission-mode imaging. They measured both the transmission amplitude and phase at a fixed frequency of 1 THz and compared the results to those achievable with a state-of-the-art time-domain system. In 2005, Gregory et al. [51] increased the dynamic range achievable with a coherent THz-FDS system to 60 dB at 500 GHz by optimizing the antenna structure at that frequency. The first tunable coherent THz-FDS system was shown in the same year by Mendis et al. [52] by using two tunable laser diodes to drive optimized LTG-GaAs photomixers with log-periodic circular-toothed antenna structures. They demonstrated a frequency resolution of a few megahertz and a peak dynamic range around 60 dB. In 2007, Wilk et al. [53] made a step towards a low-cost system by driving the photomixers with a 1064 nm dual-mode laser, albeit with a fixed frequency and no coherent detection. In the subsequent year, Deninger et al. demonstrated the first tunable coherent THz-FDS system operating at 1064 nm. The system used LTG-GaAs photomixers with log-periodic antennas driven by a pair of distributed-feedback (DFB) lasers. They demonstrated a bandwidth exceeding 1.2 THz and megahertz frequency resolution by interferometric frequency control of the DFB lasers. The dynamic range at 100 GHz with an integration time of 100 ms was 70 dB and decreased to 30 dB at 1 THz.

A major leap was made at the end of the decade by Stanze et al. [54, 55]. They demonstrated the first THz-FDS system operating at 1550 nm, thus paving the way for the use of standard telecom fiber-optic components for terahertz spectroscopy. To that end, they employed a LTG-indium gallium arsenide/indium aluminum arsenide (InGaAs/InAlAs) photomixer as the receiver. They furthermore recognized that the performance of continuous-wave terahertz systems is primary limited by the carrier lifetime of the photoconductive emitter. To resolve this, they replaced the photoconduc-

tive emitter with an indium gallium arsenide/indium gallium arsenide phosphide (InGaAs/InGaAsP) waveguide-integrated photodiode coupled to a bowtie antenna. They achieved a dynamic range of 75 dB at 75 GHz that dropped to 40 dB at 900 GHz with an integration time of 300 ms. In the following year, Kim et al. [56] demonstrated driving a THz-FDS system with a tunable dual-mode DFB laser diode operating around 1550 nm. A major improvement in performance was accomplished by Göbel et al. [57] in 2013 by optimizing the design of the InGaAs/InAlAs photoconductive detector. They achieved dynamic ranges of 105 dB at 100 GHz and 70 dB at 1 THz, both with an integration time of 200 ms.

Since then, the emitter and detector structures for THz-FDS have remained roughly the same, thus not giving any major improvements in terms of bandwidth or dynamic range. In the last few years, there have been different efforts to mitigate the major drawback of THz-FDS, namely the slow measurement speed due to the relatively slow tuning of the lasers. A notable work was published in 2021 by Liebermeister et al. [46], in which they demonstrated a THz-FDS system with a measurement rate of 200 spectra per second with a single-shot bandwidth of 2 THz and a peak dynamic range of 60 dB. Averaging over 5000 seconds allowed them to achieve an unprecedented peak dynamic range of 117 dB and a bandwidth of 4 THz. Their approach adapts the concept of frequency-modulated continuous-wave (FMCW) radar to THz-FDS. By tuning one of the two lasers driving the THz-FDS system with an extremely high tuning speed and introducing a small time delay between emitter and detector, they generate a frequency offset between emitter and detector and thus effectively realize a heterodyne detection. Besides the high measurement speed, this allowed them to measure both amplitude and phase at any frequency without any additional means of phase modulation. The particular significance of that work is that it proved that there is no inherent speed deficit of frequency-domain systems compared to time-domain systems. As will become obvious in Section 1.2, the colloquial generalization that time-domain systems are much faster than frequency-domain systems at the cost of a lower frequency resolution is merely due to the historical circumstance that femtosecond lasers became available decades earlier than fast-tunable continuous-wave lasers.

1.2 Terahertz time-domain spectroscopy

1.2.1 System description and operating principle

A mode-locked femtosecond laser is at the heart of the THz-TDS setup. Through mode locking, there is a stable phase relationship between the longitudinal modes of the laser, so that the superposition of the modes leads to a periodic output signal. By establishing a favorable phase relationship between the modes, they all interfere constructively at distinct times, so that a periodic train of short high-power pulses is emitted. The exact shape of these pulses generally depends on the width and shape of the optical spectrum as well as the precise phase relationship between the laser modes. As will be explained in more detail in Section 1.2.3, a *passively* mode-locked laser contains an element – typically a saturable absorber – within its cavity that causes mode locking without an external signal.

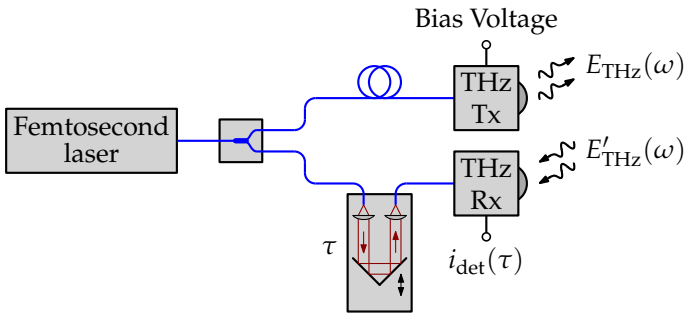

Figure 1.2: Simplified block diagram of a THz-TDS setup. Blue lines indicate polarization-maintaining fibers. Black lines indicate electrical connections.

State-of-the-art THz-TDS systems usually employ a fiber laser with a pulse duration in the order of 100 fs and a repetition rate in the order of 100 MHz to feed the terahertz spectrometer. As depicted in Figure 1.2, the infrared signal is split into a transmit and a receive arm with a fused-fiber coupler. In the receive arm, the pulses are delayed with a variable delay τ in an ODU. In the transmit arm, a section of fiber is used to compensate any static length differences between the transmit and the receive arm. Both the terahertz emitter and detector are PCAs whose structures may be optimized somewhat differently.

The PCA in the emitter is biased with a fairly high voltage (typically in the order of 100 V) whereas the detector is operated without bias. In the emitter, the femtosecond

optical pulses excite free carriers across the bandgap of the photoconductive material. These free carriers are accelerated by the applied bias field and flow as a current through the antenna structure that is coupled to the photoconductor. If the carrier lifetime in the photoconductive material is sufficiently short, the free carriers recombine quickly after the femtosecond infrared pulse has decayed. This way an ultra-short current pulse flows through the PCA with each repetition of the femtosecond laser and electromagnetic pulses are radiated into free space. Depending on the carrier dynamics, the radiated pulses are significantly longer than the femtosecond infrared pulses that excite them, but still have a bandwidth of several terahertz.

At the detector, similar to the emitter, the incident infrared pulses excite free carriers. These are, however, not accelerated by an externally applied bias field but by the terahertz electric field that is received by the antenna. The accelerated carriers contribute to an average current flow that can be measured at the terminals of the PCA. The amplitude of the average current depends on the temporal overlap between the infrared and the terahertz pulse. By changing the delay τ of the infrared with respect to the terahertz pulse with the ODU and measuring the average photocurrent $i_{\mathrm{det}}(\tau)$ at the terminals of the PCA, the received terahertz pulse can be sampled in the time domain, hence the name *time-domain* spectroscopy. The measured photocurrent is [36]

$$i_{\mathrm{det,ideal}}(\tau) \propto p_{\mathrm{opt}}(\tau) * e'_{\mathrm{THz}}(\tau) \,, \tag{1.15}$$

where $p_{\mathrm{opt}}(\tau)$ and $e'_{\mathrm{THz}}(\tau)$ are the low-pass filtered instantaneous optical power and the instantaneous terahertz field at the PCA, respectively. Transforming this expression into the frequency domain and considering the frequency dependence of the detector with the transfer function $H_{\mathrm{Rx}}(\omega)$, we get

$$I_{\mathrm{det}}(\omega) \propto P_{\mathrm{opt}}(\omega) \cdot E'_{\mathrm{THz}}(\omega) \cdot H_{\mathrm{Rx}}(\omega) \,.$$

Considering that the spectrum of the femtosecond laser stays constant, we can thus compare the spectra of different received terahertz pulses, for example with and without a sample in the RF path.

There is an important distinction to draw between the modeling of THz-FDS and THz-TDS systems. In THz-FDS, the infrared signals are continuous-wave signals with a peak-to-average power ratio (PAPR) of 2. In THz-TDS, assuming a pulse width of 100 fs and a repetition rate of 100 MHz, the PAPR is approximately 10^5. In the case of

THz-FDS, it is valid to use a small-signal model of the semiconductor components as described in Section 1.1.1. This allowed us to derive a simple frequency-domain model of the system. In the case of THz-TDS, however, non-linear processes – such as screening effects – play an important role. Thus, an accurate description requires careful consideration of the carrier dynamics both in the terahertz emitter and detector. The interested reader is referred to a review by Jepsen et al. [36] and a detailed analytical model by Duvillaret et al. [58].

1.2.2 From first demonstrations to the state of the art

The development of THz-FDS and THz-TDS have run somewhat in parallel, with THz-TDS being the slightly more mature sibling. THz-TDS has always been a step ahead in terms of bandwidth and measurement speed.

In the early 1970s, Ippen and Shank introduced the concept of passive mode locking in dye lasers [59, 60]. This concept allowed them to generate optical pulses with a pulse width as low as 1.5 ps. In 1981, Fork et al. [61] extended the concept of passive mode locking by employing a scheme called "colliding pulse mode locking" (CPM) where two counterpropagating pulses interact in the laser cavity. Using this approach, they were able to reduce the pulse width to 90 fs. In the same year, Mourou et al. [62] used optical pulses from a mode-locked dye laser to drive a GaAs photoconductive switch that was coupled to a small dipole antenna. This was effectively the first PCA. They could show that the microwave pulses radiated by the dipole had a pulse width of less than 3 ps, but they did not use the term "terahertz" yet.

Three years later, Auston et al. [63] showed that PCAs could not only be used for the generation but also for the detection of terahertz radiation. They placed two photoconductive dipoles on opposite sides of an electrically insulating slab. The photoconductor they used was radiation-damaged silicon-on-sapphire (SOS). Both PCAs where driven through free space by the same CPM laser with a pulse width of 100 ps. Similar to the block diagram shown in Figure 1.2, the emitter PCA was electrically biased, whereas the detector PCA was connected to a highly sensitive current amplifier. By scanning the delay between the optical pulse at the detector and emitter, they sampled the microwave pulse that was transmitted through the insulating slab. This was effectively the first THz-TDS setup and is the prototype for the system described in Section 1.2.1.

The detected pulses exhibited a pulse width of 2.3 ps. In 1988, Fattinger et al. [64] adopted this approach in a reflection geometry by placing the emitter and detector PCA in the same plane. They placed a spherical mirror above the pair of PCAs, thus reflecting the radiation from the emitter onto the detector. They measured a pulse width of 1 ps and for the first time called this a "terahertz" system. They furthermore predicted that in the future further standard optical elements could be used for terahertz applications, for example, to collimate the terahertz radiation from the emitter. In the following year [65], the same group followed through on this promise and transmitted terahertz pulses over a distance of 1 m by collimating the radiation from the photoconductive emitter and focusing it onto the photoconductive detector with a pair of sapphire lenses. This configuration is almost identical to today's terahertz transmission spectroscopy setups. In their visionary work, they discussed the effects of water vapor absorption lines as well as possible applications of this new concept for spectroscopy and wideband communications.

The last three decades have seen different improvements of the THz-TDS concept. These can be grouped into

- technological advances that improved the system performance while enabling a transition from bulky and sensitive near-infrared free-space-optical setups to compact and robust fiber-coupled setups operating at 1550 nm, and
- engineering improvements that aimed to alleviate the need for a free-space ODU in the setup.

Technological advances

It was found early on that the carrier lifetime in the PCA is the most limiting factor for the system bandwidth. The shorter the carrier lifetime is, the higher the usable bandwidth of the THz-TDS system is. This is particularly true for the emitter. A detailed discussion can be found in [58]. Besides the investigation of the influence of the carrier lifetime, it was shown that the high-frequency limit of the system is dominated by the laser pulse width. In 1992 and 1993, Gupta et al. [66, 67] discussed different ways to achieve short carrier lifetimes. They introduced LTG-GaAs as a particularly attractive material for that purpose. LTG-GaAs has since then remained the material of choice for PCAs driven by near-infrared lasers. In the same year, Kafka et al. [68] introduced the

Ti:sapphire mode-locked laser as an alternative to the dye lasers that were prevalent at the time. The Ti:sapphire laser exhibited a larger tuning range as well as a higher pump power handling capability. It allowed the construction of the first "compact" (i.e. table-sized) THz-TDS systems. In 1994, Takahashi et al. [69] demonstrated the first photoconductive material with a carrier lifetime as low as 1 ps that is sensitive at 1550 nm. They employed a LTG-InGaAs/InAlAs multiple quantum well (MQM) structure. Still, near-infrared systems dominated terahertz labs.

A decade later, different competing approaches to shorten the carrier lifetime by adding defects in the InGaAs/InAlAs material system were proposed. Suzuki et al. demonstrated iron- (Fe-) implanted InGaAs photoconductive terahertz detectors [70] and emitters [71]. Takazoto et al. [72] proposed beryllium- (Be-) doping and demonstrated a bandwidth of 2.5 THz with a peak signal-to-noise power ratio of 45 dB.

In 2008, Sartorius et al. [73] made a significant advancement by presenting the first all-fiber THz-TDS system operating at 1550 nm. The system employed LTG-InGaAs/InAlAs PCAs with a novel multiple quantum well (MQW) structure and was driven by a mode-locked fiber laser. The use of a compact fiber laser and fiber-coupled emitter and detector heads meant an important step towards a plug-and-play system. They demonstrated a bandwidth of 3 THz. In 2010, Roehle et al. [74] presented improved PCAs using a 3D-mesa structuring process that yielded an improvement by a factor of 27.5 in detected amplitude compared to planar antennas and exhibited a bandwidth of 4 THz. In the same year, Wood et al. [75] demonstrated terahertz emission from metal-organic chemical vapor deposition (MOCVD) grown iron-doped InGaAs (Fe:InGaAs). Particular about this work was that they demonstrated the material system's ability to be excited across the wavelength range from 830 to 1550 nm. In 2013 and 2014, Dietz et al. [76, 77] presented a molecular beam epitaxy- (MBE-) grown InGaAs/InAlAs multilayer heterostructure (MLHS) for the emitter and a Be-doped LTG-InGaAs/InAlAs MLHS for the detector. With these structures, they achieved a radiated power of 64 µW, a bandwidth of 6 THz, and a peak dynamic range of 90 dB. The problem with these high-performance devices was that the emitter and detector were fabricated in separate processes.

In 2017, Globisch et al. [78] solved this problem by demonstrating that MBE-grown iron-doped InGaAs (Fe:InGaAs) can be used to fabricate both high-performance emitters and detectors. Using this material system, they demonstrated a radiated power of

75 μW, a bandwidth of 6 THz, and a peak dynamic range of 95 dB. Kohlhaas et al. [79] recently made use of this by constructing a photoconductive transceiver that employs an emitter and detector PCA on the same substrate behind a single silicon lens. This device allows true monostatic reflection-mode measurements with a THz-TDS system. There are several other recent works showing structures such as an InGaAs/InAlAs superlattice with localized Be-doping [80], a GaAs epilayer with erbium arsenide (ErAs) quantum dots [81], and an InGaAs/InAlAs superlattice with ErAs inclusions [82].

Towards THz-TDS without a free-space-optical ODU

While the advent of fiber laser-driven THz-TDS [73] made the systems significantly more compact and robust, the free-space optical component that remained in any THz-TDS system was the ODU. To remedy that, several different approaches have been proposed. The oldest approach is called "asynchronous optical sampling" (ASOPS) [83, 84]. In ASOPS, the terahertz emitter and detector are driven by two separate optical pulse trains. The two pulse trains exhibit constant but slightly different repetition rates. Thus, the optical pulses repetitively pass the terahertz pulses incident on the terahertz detector. This is equivalent to one of the pulses being conventionally delayed with an ODU. The two pulse trains can, for example, be emitted from two mutually stabilized Ti:sapphire lasers [84,85] or from a bidirectional mode-locked fiber laser with two outputs [86].

A variation of the ASOPS concept is an approach called "electronically controlled optical sampling" (ECOPS) [87, 88]. As the name suggests, in ECOPS the repetition rates of the pulse trains are electronically controlled during the operation. ECOPS has the advantage of allowing higher scan rates with low repetition rate mode-locked lasers.

Another approach is called "optical sampling by laser cavity tuning" (OSCAT) [89–91]. The OSCAT approach employs a single mode-locked laser whose repetition rate is continuously modulated by tuning the length of the cavity. A static time delay between emitter and detector is introduced in the setup with a piece of fiber. Because of this static delay and the modulation of the laser's repetition rate, the instantaneous repetition rates at the emitter and detector are different and a scanning similar to the ASOPS concept is achieved.

A recently proposed approach is called "single-laser polarization-controlled optical

sampling" (SLAPCOPS) [92]. The SLAPCOPS concept is a variation of the ECOPS approach using only a single laser. The SLAPCOPS laser is a fiber laser with a single pump diode and gain section but two cavities. By using a pair of polarization beam splitters/combiners, the optical signals circulating in the two fiber cavities are polarization multiplexed through the same gain medium, i.e. the same Erbium-doped fiber, with opposite propagation directions. Due to the polarization multiplex, the two counterpropagating pulse trains do not interfere with each other and can be independently coupled out of the laser. One of the two cavities includes a piezo phase shifter to modulate the repetition rate of the pulse train in that cavity, thus enabling the ECOPS operation of the system.

1.2.3 Monolithic light sources for THz-TDS

While the developments described in Section 1.2.2, in particular the introduction of all-fiber systems based on the mode-locked fiber laser and fiber-coupled PCAs, have paved the way towards compact and robust THz-TDS systems, their widespread application is still hindered by the high cost and relative bulkiness of the fiber laser. State-of-the-art fiber lasers still cost tens of thousands of euros, which makes them the major contributor to the overall system cost. Moreover, while the cost of the terahertz emitter and detector can be expected to go down with scaling of the semiconductor process as the number of fabricated devices increases, the assembly of the fiber laser is quite complex and consists of several specialized parts. A monolithic light source would be preferable, as it is significantly more compact, robust, and has the potential to be mass-produced. Quite early, different groups have looked at monolithic light sources for THz-TDS. Three options have gained particular attention, the third of which is the topic of the majority of this thesis.

Multi-mode laser diodes

As early as 1997, Tani et al. [93] performed experiments driving a biased PCA with a low-cost commercially available multi-mode laser diode (MMLD) [4]. They measured the RF spectrum radiated by the PCA and found discrete spectral peaks at integer

[4] Analogous to footnote 1, the term "multi-mode" specifically indicates multiple longitudinal laser modes. Notwithstanding the above, the laser diode used by Tani happened to exhibit more than one transversal mode as well [93].

multiples of $F = 52\,\mathrm{GHz}$, where F was the MMLD's free spectral range (FSR). Each spectral component at the frequency mF , $m \in \mathbb{N}$, was the superposition of the beat signals of all pairs of laser modes that were located mF apart. Because the modes of the MMLD are not locked, there is no stable phase relationship between them, thus yielding a high linewidth of the spectral peaks of around 4 GHz. It was already found by Tani et al. that "the spectral intensity for the lowest frequency mode (52 GHz) is the strongest, as expected from the highest number of the laser modes contributing to the fundamental beat frequency and the decreasing efficiency of the photoconductive bow-tie antenna for higher frequencies" [93].

In 1999, Morikawa et al. [94] used this source of terahertz radiation for spectroscopic measurements by comparing the amplitude spectra measured with and without a sample in the path of the terahertz radiation. To measure the amplitude spectra, they used a Martin–Puplett-type interferometer with a bolometer.

In the following year, the same group [95] built on this work and demonstrated that a MMLD cannot only be used for the generation but also the detection of terahertz radiation. To that end, they drove a conventional THz-TDS setup with a MMLD. Doing so, they measured a photocurrent at the output of the photoconductive detector that was periodic with the delay introduced by the ODU. The periodicity of this photocurrent matched the mode spacing of the MMLD. Even though the light intensity of the MMLD fluctuates very rapidly as the laser modes randomly change their amplitudes and phases, the measured photocurrent is very stable. The measured photocurrent is proportional to the time average of the product of the instantaneous optical power and the instantaneous electric terahertz field at the photoconductive detector, i.e. the cross correlation of the two quantities. Because of that, this approach was called *terahertz cross-correlation spectroscopy* (THz-CCS).

If we remember that the terahertz signal and the optical signal at the photoconductive detector have been generated by the same MMLD, we can see that the detected photocurrent is equal to the convolution of the autocorrelation of the low-pass filtered instantaneous optical power and the impulse response of the terahertz system. Assuming that the random process describing the MMLD is stationary, the detected photocurrent can be written in the frequency domain as [95]

$$I_{\mathrm{det}}(\omega) \propto H_{\mathrm{THz}}(\omega) \cdot \left|S_{\mathrm{opt}}(\omega)\right|^2 , \tag{1.16}$$

where $H_{\mathrm{THz}}(\omega)$ is the combined transfer function of the terahertz system and $S_{\mathrm{opt}}(\omega)$ is the power spectral density of the low-pass filtered instantaneous optical power. Thus, as long as the power spectral density remains constant, which can be assumed if the operating parameters of the MMLD remain unchanged, the detected terahertz spectrum only depends on the transfer function of the terahertz system. In 2004, Morikawa et al. [96] improved the performance of this approach by replacing the free-space optical setup with a fiber-optic setup and observed spectral components up to about 600 GHz.

Interestingly, the same concept was rediscovered in 2009 and published under the name *quasi time-domain spectroscopy* (QTDS) by Scheller et al. [97]. They also measured a bandwidth of about 600 GHz. In their publication, Scheller et al. describe the system in the frequency domain by mixing between the modes of the MMLD. They state that because of "the time averaging characteristic of the detection process [...] the phase of the detected THz frequency components is not related to the random phase between the multimode laser lines". As we will see later, the irrelevance of the phases of the laser modes in THz-CCS is of particular importance. Both Morikawa's and Scheller's experiments were performed with near-infrared lasers.

In 2017, Kohlhaas et al. [98] moved this concept to telecom wavelengths by using a Fabry-Perot MMLD (Thorlabs FPL1055T, $\lambda_0 = 1550\,\mathrm{nm}$, $F \approx 43.5\,\mathrm{GHz}$) and state-of-the-art InGaAs emitter and detector modules. With this setup, they were able to demonstrate a bandwidth of about 1.5 THz. In 2018 and 2019, Rehn et al. [99, 100] showed the enhancement of the terahertz bandwidth by low duty cycle operation of the MMLD and optical feedback into the MMLD, respectively. In their second paper, they used a laser diode (Thorlabs FPL1009P) that appeared to be a fiber-coupled version of the MMLD used by Kohlhaas in his 2017 paper. However, Rehn made some conflicting observations that indicated that the laser may be mode-locked under certain conditions.

Superluminescent diodes

The frequency resolution of THz-TDS systems is primarily determined by two parameters. The first parameter is the length of the ODU, as it determines the size of the discrete Fourier transform (DFT) window. The second parameter is the optical spectrum of the light source, since the spacing of the laser modes determines the spacing of the spectral components of the terahertz spectrum. In the case of a fiber laser, the mode spacing (i.e. the FSR) is typically around 100 MHz. A double-pass ODU whose delay range is long enough to scan one repetition period of the laser would need to be 1.5 m long. In practice, ODUs are typically much shorter than that, so that the frequency resolution is usually limited by the length of the ODU. However, in the case of THz-CCS, where the setup is driven by an MMLD, the mode spacing is in the range of several ten gigahertz due to the much shorter cavity of the MMLD. In that case, the frequency resolution is limited by the FSR of the light source.

In 2019, Molter et al. [101] tried to address this drawback of monolithic lasers by driving a THz-CCS setup with a monolithic superluminescent diode (SLD). The SLD does not have a cavity, so its optical spectrum does not have a mode structure. The SLD emits virtually incoherent light with a very wide and smooth spectrum with a 3 dB-bandwidth of about 5.7 THz. Using this light source, they were able to demonstrate a continuous terahertz spectrum with a bandwidth of 1.7 THz and a peak dynamic range of 60 dB after 20 s averaging time.

Mode-locked laser diodes

The THz-CCS approach using either a MMLD or a SLD has demonstrated that it is possible to drive a photonic terahertz spectrometer with light that has small or virtually no temporal coherence, respectively. However, the lack of temporal coherence can cause problems in some applications that will be discussed in Chapter 3. An alternative monolithic light source that promises to provide behavior similar to "classical" THz-TDS is a mode-locked laser diode (MLLD). MLLDs have been subject to intense research for more than twenty years due to their widespread applicability in metrology, signal processing, and communications. The prospect of integration in fiber optic networks and the availability of a suitable material system have early on led to MLLD implementations at 1550 nm telecom wavelengths. The wide range of possible appli-

cations on the other hand has led to the development of MLLDs with a wide range of pulse widths and repetition rates. Pulse widths tend to be somewhere between a few hundred femtoseconds and several picoseconds, whereas repetition rates range from a few gigahertz to hundreds of gigahertz. An excellent review can be found in Ref. [102].

The material system of choice is InGaAs/GaAs/InAs on an InP substrate. The key technology that has enabled high-performance MLLDs with low injection current, small pulse width, low noise, and low temperature sensitivity is the inclusion of quantum dots (QDs) or quantum dashes (QDashes) in the semiconductor. A comprehensive review of QD lasers can be found in Ref. [103].

There are three mode-locking mechanisms: *Active*, *passive*, and *hybrid* mode-locking. Actively mode-locked lasers acquire their lock through the injection of an RF signal with a frequency that is close to the FSR of the laser cavity. Passively mode-locked lasers automatically lock their modes when they are operated with the correct injection current, temperature, and in some cases reverse bias voltage. In this case the repetition rate of the MLLD is solely determined by the optical length of the cavity and the operating conditions. Hybridly mode-locked lasers are locked to an injected RF signal, but contain similar elements as passively mode-locked lasers to shorten the pulse. In this thesis, the term MLLD represents passively mode-locked laser diodes.

Conventionally, MLLDs consist of a two sections: A gain section and a saturable absorber section. An excellent explanation of the mode-locking principle of two-section MLLDs is given in Ref. [103]. However, it has been found that single-section laser diodes, that is to say Fabry-Pérot laser diodes without a saturable absorber, can also exhibit mode locking [104]. While their mode of operation is not as well understood as that of two-sections MLLDs and they are more difficult to control due to the absence of a saturable absorber, they exhibit some interesting properties. Besides the simplicity of their structure, they typically exhibit the lowest pulse width at a higher injection current, which benefits their ability to emit short high-power pulses. However, single-section MLLDs exhibit a much stronger group delay dispersion (GDD) than two-section devices. This requires external dispersion compensation in order to generate short optical pulses. The implications of this aspect will be discussed in great depth in Chapter 2. A detailed comparison between single-section and two-section MLLDs with a particular focus on single-section MLLDs can be found in Refs. [105,106].

In 2017, Merghem et al. [107] demonstrated for the first time the use of an MLLD to drive a terahertz time-domain spectrometer. They used a single-section QDash laser with a center wavelength of 1550 nm and a repetition rate of about 41 GHz. Because of its single-section design, the emitted pulses were strongly chirped. They used the anomalous dispersion of a 62 m long section of single-mode fiber at 1550 nm to compress the pulses and achieved a pulse width below 1 ps [5]. They employed commercially available fiber-coupled PCAs both as the terahertz emitter and detector and were able to demonstrate a bandwidth of about 600 GHz and a peak dynamic range of 45 dB. Although these numbers were somewhat disappointing, they still proved that a single-section monolithic MLLD can be used to drive a THz-TDS system. This demonstration is the experimental groundwork for all further investigations in this thesis and a large amount of research activity within our group. Because this approach is akin to conventional THz-TDS but with an orders of magnitude higher repetition rate, we have coined the term *ultra-high repetition rate terahertz time-domain spectroscopy* (UHRR-THz-TDS). This intentionally sets it apart from the previously presented THz-CCS approach.

Within the last few years, our group has put a lot of effort into the improvement of the performance of UHRR-THz-TDS systems. We have suspected that the limited bandwidth and dynamic range observed by Merghem was due to the use of conventional PCAs both for the terahertz emitter and detector. As was shown in Ref. [58], the bandwidth of a THz-TDS system using a PCA emitter is largely determined by the optical pulse width and the carrier lifetime of the emitter PCA. The pulse width of the MLLD used by Merghem was however about ten times longer than that of a state-of-the-art fiber laser. In 2019, Tybussek et al. [14] demonstrated UHRR-THz-TDS with state-of-the-art ErAs:In(Al)GaAs PCAs. These exhibited carrier lifetimes around 2 ps, whereas the PCAs used by Merghem had a carrier lifetime of about 30 ps. The employed MLLD was the same Thorlabs FPL1009P used previously by Rehn [100] in his work on the spectral enhancement of THz-CCS. However, intensity autocorrelation measurements suggested that the laser was at least partially mode-locked under the correct operating conditions, i.e. injection current and temperature. The terahertz measurement revealed a bandwidth of about 1.4 THz and a peak dynamic range of 51 dB.

Another argument can be made by looking at the PAPR of the optical signal. Assuming that the MLLD has a repetition rate of 50 GHz and a pulse width of 500 fs, we get an

[5] In the context of optical fibers, the term “single-mode” indicates a single *transversal* mode.

approximate PAPR of 25. This is much closer to the PAPR of a continuous-wave system (PAPR $= 2$) than that of a fiber laser-driven THz-TDS system (PAPR $\approx 10^5$). It is known from THz-FDS that continuous-wave systems perform well up to 2 THz if they use an antenna-integrated photodiode-based terahertz emitter. It is thus safe to assume that such an emitter would perform well for UHRR-THz-TDS, too. We have verified this assumption in recent works [1,3] and observed bandwidths up to 1.5 THz with a peak dynamic range exceeding 60 dB.

CHAPTER

TWO

SYSTEM-THEORETICAL ANALYSIS OF UHRR-THZ-TDS

While there are a few mathematical descriptions of THz-CCS in literature, these cannot be applied to UHRR-THz-TDS because they assume a stochastic laser signal and do not take into account the phase spectrum of the MLLD. In this chapter, a simple yet accurate system-theoretical model of an UHRR-THz-TDS system is presented. This model makes it possible to calculate the detected terahertz spectrum from the complex optical spectrum of the MLLD and the transfer function of the terahertz system. It provides plentiful new insights into the system's operating principle and accurately describes the influence of the optical phase on the detected terahertz spectrum. In particular, it explains the experimentally observed relevance of chirp compensation in UHRR-THz-TDS and gives the relationship between the intensity autocorrelation of the MLLD and the detected terahertz spectrum.

I have first published this model in Ref. [1]. In Section 2.1, the findings in that work will be summarized and a more detailed analysis of the results is provided. For more details of the mathematical derivation, the interested reader is referred to Ref. [1]. Please note that this chapter slightly deviates from the notation used in the reference to better match the remainder of this thesis. In Section 2.2, a few important conclusions from the system-theoretical model regarding the influence of pulse chirp on the emitted as well as the detected terahertz spectrum are drawn. Also, the relevance of the number of

laser modes are analyzed. Finally, in Section 2.3, some experimental results that verify the validity of the mathematical model are summarized.

2.1 System-theoretical modeling

A simplified block diagram of an UHRR-THz-TDS setup is depicted in Figure 2.1. The optical signal from the MLLD first passes a device that compensates the inherent chirp of the laser pulse. This device can either be a suitable section of single-mode fiber (or polarization-maintaining single-mode fiber) or an optical filter. The anomalous dispersion of single-mode fiber has proven to be a simple yet effective tool for this purpose. The optical signal is then split into a transmit and a receive path with a 50:50 fused fiber coupler. In the receive path, the optical signal is delayed with an ODU by the delay τ. In the transmit path, a "dummy" section of fiber is used to ensure that the path lengths from the splitter to the emitter and detector modules are roughly the same. The emitter module is an electrically biased antenna-integrated photodiode, whereas the detector module is an unbiased PCA. The measured quantity in the setup is the photocurrent $i_{\mathrm{det}}(\tau)$ at the terminals of the detector.

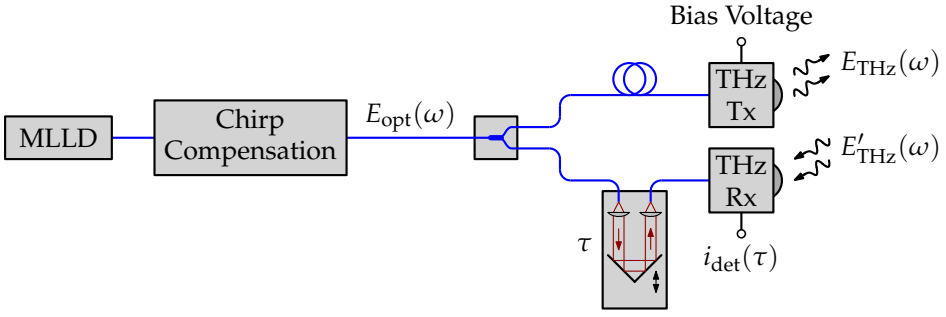

Figure 2.1: Simplified block diagram of an UHRR-THz-TDS setup. Blue lines indicate polarization-maintaining fibers. Black lines indicate electrical connections.

2.1.1 Mathematical description of the mode-locked laser diode

The complex optical spectrum emitted by the MLLD can be written as

$$e_{\mathrm{opt}}(t) = \sum_{k=0}^{N-1} E_k \cdot \cos\left[(\omega_0 + k\Omega) \cdot t + \varphi_k\right] \tag{2.1}$$

$$\circ\!\!-\!\!\bullet$$

$$E_{\mathrm{opt}}(\omega) = \sum_{k=0}^{N-1} E_k \cdot \left\{\delta\left[\omega + (\omega_0 + k\Omega)\right] \cdot \mathrm{e}^{-\mathrm{j}\varphi_k} + \delta\left[\omega - (\omega_0 + k\Omega)\right] \cdot \mathrm{e}^{\mathrm{j}\varphi_k}\right\}, \tag{2.2}$$

with $\Omega = 2\pi F$, where N is the number of considered laser modes, ω_0 is the angular frequency of the first considered laser mode, F is the repetition rate of the MLLD, and E_k and φ_k are the amplitude and phase of the k-th mode, respectively. The field amplitudes E_k are normalized so that their squares equal the optical powers of the laser modes. This expression describes a comb-like structure of equidistant modes. For the purposes of this derivation, we assume laser modes with infinitely small linewidth.

2.1.2 Filtered instantaneous optical power

We have seen in the mathematical description of a THz-FDS system in Section 1.1.1 that the instantaneous optical power, i.e. the squared magnitude of the instantaneous electrical field, is of particular importance in describing both the generation and detection of terahertz radiation. In the case of UHRR-THz-TDS, it contains spectral components at the difference- and sum-frequencies of the MLLD's modes. However, due to the low-pass behavior of the terahertz emitter and detector, the sum-frequency components can be neglected. It is thus useful to define a *filtered* instantaneous optical power that only contains the difference-frequency components [1], [106]:

$$p_{\mathrm{opt}}(t) \propto \sum_{k=0}^{N-1} E_k^2 \; + \; 2 \cdot \sum_{m=1}^{N-1} \sum_{k=m}^{N-1} E_k E_{k-m} \cdot \cos\left(m\Omega t + \varphi_k - \varphi_{k-m}\right) \tag{2.3}$$

$$\circ\!\!-\!\!\bullet$$

$$P_{\mathrm{opt}}(\omega) \propto 2\pi \cdot \sum_{m=0}^{N-1} \sum_{k=m}^{N-1} E_k E_{k-m} \cdot \left[\delta\left(\omega - m\Omega\right) \cdot \mathrm{e}^{-\mathrm{j}(\varphi_k - \varphi_{k-m})} + \delta\left(\omega + m\Omega\right) \cdot \mathrm{e}^{\mathrm{j}(\varphi_k - \varphi_{k-m})}\right]. \tag{2.4}$$

It can be seen that the filtered instantaneous optical power consists of discrete spectral components at the angular frequencies $\omega = m\Omega$, $0 \leq m \leq N-1$. The average optical power ($m = 0$) is simply the sum of the optical powers of all laser modes, whereas the amplitudes and phases of the other spectral components ($m > 0$) result from the complex superposition of the beat signals of all pairs of laser modes that have the spacing $m\Omega$. In the general case of arbitrary amplitude and phase distributions of the laser modes, the beat signals interfere in a rather complex way. However, we can see that in the case of a linear phase distribution, the term $\varphi_k - \varphi_{k-m}$ is independent of k. In this case, all the beat signals at the angular frequency $m\Omega$ interfere constructively.

2.1.3 Transmitted and received terahertz field

A photodiode responds to the filtered instantaneous optical power of the incident light. If the peak power is sufficiently small, this response is linear. As previously discussed, the PAPR of an MLLD is relatively low. Thus, the photocurrent generated by the antenna-integrated photodiode in the emitter module is approximately proportional to the filtered instantaneous optical power:

$$I_{\mathrm{THz}} \propto P_{\mathrm{opt}}(\omega) \; . \tag{2.5}$$

This photocurrent flows through the transmit antenna and radiates a terahertz wave. As elaborated in Section 1.1.1, the terahertz electric field in the far field of the antenna is proportional to the current flowing through the antenna. Furthermore, the antenna-integrated photodiode itself has a frequency response that must be accounted for by a transfer function $H_{\mathrm{Tx}}(\omega)$ describing the emitter. Thus, the terahertz electric field in the far field of the emitter can be written as [1]

$$\begin{aligned} E_{\mathrm{THz}}(\omega) &\propto H_{\mathrm{Tx}}(\omega) \cdot P_{\mathrm{opt}}(\omega) \\ &\propto H_{\mathrm{Tx}}(\omega) \cdot 2\pi \cdot \sum_{m=1}^{N-1} \sum_{k=m}^{N-1} E_k E_{k-m} \\ &\quad \cdot \left[\delta\left(\omega - m\Omega\right) \cdot \mathrm{e}^{-\mathrm{j}(\varphi_k - \varphi_{k-m})} + \delta\left(\omega + m\Omega\right) \cdot \mathrm{e}^{\mathrm{j}(\varphi_k - \varphi_{k-m})} \right] \; . \end{aligned} \tag{2.6}$$

The influence of the RF channel between emitter and detector can be accounted for by the transfer function $H_{\text{Channel}}(\omega)$, so that the field received by the detector is [1]

$$\begin{aligned} E'_{\text{THz}}(\omega) &\propto H_{\text{Channel}}(\omega) \cdot E_{\text{THz}}(\omega) \\ &\propto H_{\text{Tx}}(\omega) \cdot H_{\text{Channel}}(\omega) \cdot 2\pi \cdot \sum_{m=1}^{N-1} \sum_{k=m}^{N-1} E_k E_{k-m} \\ &\quad \cdot \left[\delta\left(\omega - m\Omega\right) \cdot \mathrm{e}^{-\mathrm{j}(\varphi_k - \varphi_{k-m})} + \delta\left(\omega + m\Omega\right) \cdot \mathrm{e}^{\mathrm{j}(\varphi_k - \varphi_{k-m})} \right] . \end{aligned} \tag{2.7}$$

2.1.4 Detected photocurrent

To determine the photocurrent $i_{\text{det}}(\tau)$ that can be measured at the terminals of the detector, it is necessary to look at the mixing process taking place in the photoconductive detector. The instantaneous photoconductivity of the photoconductor $g(t)$ is approximately proportional to the filtered instantaneous optical power of the optical signal illuminating the photoconductor. This optical signal is the same as that illuminating the emitter, but it is delayed by the delay τ of the ODU:

$$g(t,\tau) \propto p_{\text{opt}}(t-\tau) \tag{2.8}$$

$$\circ\!\!-\!\!\bullet$$

$$G(\omega,\tau) \propto P_{\text{opt}}(\omega) \cdot \mathrm{e}^{-\mathrm{j}\omega\tau} . \tag{2.9}$$

The electric field of the terahertz wave that is incident on the photoconductive detector modulates the voltage $v(t)$ across the photoconductor:

$$v(t) \propto e'_{\text{THz}}(t) \tag{2.10}$$

$$\circ\!\!-\!\!\bullet$$

$$V(\omega) \propto E'_{\text{THz}}(\omega) . \tag{2.11}$$

The current flowing through the photoconductor can thus be described by the product of the conductivity $g(t,\tau)$ and the voltage $v(t)$ across the photoconductor. The current $i_{\text{det}}(\tau)$ that is measured at the terminals of the detector is proportional to the time average of this current. This can be written as [1]

$$i_{\mathrm{det}}(\tau) \propto \mathcal{F}^{-1}\left\{\frac{1}{2\pi}\cdot\left[P_{\mathrm{opt}}(\omega)\cdot \mathrm{e}^{-\mathrm{j}\omega\tau}\right] * \left[H_{\mathrm{Rx}}(\omega)\cdot E'_{\mathrm{THz}}(\omega)\right]\Big|_{\omega=0}\right\}\,, \tag{2.12}$$

where $H_{\mathrm{Rx}}(\omega)$ describes the frequency response of the photoconductive detector. After a lengthy calculation, this expression can be simplified to [1]

$$\begin{aligned} i_{\mathrm{det}}(\tau) \propto 2\cdot\sum_{m=1}^{N-1}\Bigg\{ & |H_{\mathrm{THz}}(m\Omega)|\cdot\sin\left[m\Omega\tau+\angle H_{\mathrm{THz}}(m\Omega)\right] \\ & \cdot\sum_{k=m}^{N-1}\sum_{l=m}^{N-1} E_k E_{k-m} E_l E_{l-m}\cdot\cos\left[(\varphi_k-\varphi_{k-m})-(\varphi_l-\varphi_{l-m})\right]\Bigg\}\,, \end{aligned} \tag{2.13}$$

where

$$H_{\mathrm{THz}}(m\Omega) = m\Omega\cdot H_{\mathrm{Tx}}(m\Omega)\cdot H_{\mathrm{channel}}(m\Omega)\cdot H_{\mathrm{Rx}}(m\Omega)\,,\ m=1\ldots N-1\,, \tag{2.14}$$

combines the frequency responses of the emitter, the detector, and the RF channel. The double sum in the second row of this equation can be interpreted as a set of unique amplitude factors [1]

$$\boxed{\begin{aligned} A_m = \sum_{k=m}^{N-1}\sum_{l=m}^{N-1} & E_k E_{k-m} E_l E_{l-m} \\ & \cdot\cos\left[(\varphi_k-\varphi_{k-m})-(\varphi_l-\varphi_{l-m})\right]\,,\ m=0\ldots N-1\,, \end{aligned}} \tag{2.15}$$

that depend only on the complex optical spectrum of the MLLD. Using this expression, the detected photocurrent can be written in the compact form [1]

$$\boxed{i_{\mathrm{det}}(\tau) \propto 2\cdot\sum_{m=1}^{N-1}|H_{\mathrm{THz}}(m\Omega)|\cdot\sin\left[m\Omega\tau+\angle H_{\mathrm{THz}}(m\Omega)\right]\cdot A_m\,.} \tag{2.16}$$

We can draw numerous important conclusions from this result. The detected photocurrent in an UHRR-THz-TDS system consists of spectral components at the angular frequencies $\nu = m\Omega\,,\ m=1\ldots N-1$. The amplitude of each spectral component is the product of the magnitude $|H_{\mathrm{THz}}(m\Omega)|$ of the transfer function of the terahertz system at that angular frequency and an amplitude factor A_m that depends on the amplitudes and phases of all laser modes that are involved in the generation and detection of that

spectral component. The phase of each spectral component depends only on the phase $\angle H_{\mathrm{THz}}(m\Omega)$ of the transfer function at the respective angular frequency. If the spectrum of the MLLD is stable, which can be assumed under mode-locked conditions, changes in the detected spectrum can be directly attributed to changes in the transfer function of the terahertz system. The complex optical spectrum of the MLLD only determines the maximum achievable amplitude of each component of the detected terahertz spectrum. An important differentiation from the THz-CCS approach is that the amplitudes A_m result from deterministic beating of the laser modes rather than time averaging over random fluctuations of the beat signals. In Section 2.2, the terms A_m are analyzed in greater detail.

2.1.5 Intensity autocorrelation

The conventional way of characterizing an MLLD is by measuring its intensity autocorrelation function $R_{pp}(\tau)$, commonly known as *second harmonic generation* (SHG) autocorrelation. It is the autocorrelation function of the filtered instantaneous optical power [1]:

$$R_{pp}(\tau) = p_{\mathrm{opt}}(\tau) * p_{\mathrm{opt}}(-\tau)\,. \tag{2.17}$$

A lengthy calculation leads to the expression [1]

$$R_{pp}(\tau) \propto \sum_{m=0}^{N-1} \cos\left(m\Omega\tau\right) \cdot A_m\,. \tag{2.18}$$

This expression shows the close relationship between the intensity autocorrelation and the detected photocurrent in the UHRR-THz-TDS system. The intensity autocorrelation consists of discrete spectral components at the frequencies $\nu = m\Omega\,, m = 0 \ldots N-1$. There is no delay between these spectral components, indicating that they have common maxima at $\tau_{\mathrm{max},n} = nF^{-1}\,,\ n \in \mathbb{Z}$. Distinct symmetrical pulses appear at these positions. The shape and amplitude of these pulses depend on the factors A_m.

The comparison of Equations (2.16) and (2.18) gives us an interesting alternative explanation of the UHRR-THz-TDS approach that shows an undeniable relationship with the THz-CCS approach. The detection process in the photoconductive detector effectively measures the autocorrelation of the MLLD signal weighted with the amplitude

and phase of the terahertz system's transfer function. The difference between THz-CCS and UHRR-THz-TDS is the fact that the optical signal from an MLLD is primarily deterministic, whereas the signals from a MMLD or SLD are stochastic. This has an important effect on the measured photocurrent $i_{\mathrm{det}}(\tau)$ and intensity autocorrelation function $R_{pp}(\tau)$. In the case of an MLLD driving the system, both measured quantities are periodic with the period $1/F$, and their envelope decays only slowly with increasing absolute value of τ. In the case of a MMLD driving the system, they are periodic with the period $1/F$, but their envelope quickly decays with increasing absolute value of τ. In the case of an SLD, both the photocurrent and the intensity autocorrelation are aperiodic and exhibit a single distinct maximum at $\tau = 0$. The practical consequences of these differences are discussed in Chapter 3.

Another important conclusion from the comparison of Equations (2.16) and (2.18) is that the detected terahertz spectrum can be calculated given the intensity autocorrelation of the MLLD and the transfer function of the terahertz system. More importantly, the measurement of an MLLD's intensity autocorrelation allows us to evaluate its performance in an UHRR-THz-TDS system. As we will see in Chapter 4, we can use the knowledge of this relationship to engineer optical spectra that imprint desired characteristics on the detected terahertz spectrum. Moreover, it makes it possible to specify requirements for the development of MLLDs that are optimized for UHRR-THz-TDS.

2.2 Conclusions from the system-theoretical model

In this section, a few key lessons from the theoretical analysis in the previous section are drawn. In particular, the influences of the optical phase distribution and the number of laser modes on the emitted terahertz signal and the detected photocurrent are evaluated.

2.2.1 Influence of the pulse chirp

It is well-known that the pulse from a mode-locked laser needs to be chirp-free in order to achieve a minimum pulse width and maximum pulse amplitude. This is addressed either by designing the laser cavity such that it automatically emits chirp-free pulses or by external pulse compression. In the first demonstration of UHRR-THz-

TDS, Merghem et al. [107] by habit compensated the chirp of their single-section MLLD with a section of single-mode fiber. In this section, the effect of laser chirp on the emitted as well as the detected terahertz spectrum are quantified.

Quantification of pulse chirp

In their 2012 paper, Rosales et al. [106] analyzed the chirp of single-section and two-section MLLDs. They found that the chirp of single-section MLLDs was much stronger. In 2016, O'Duill et al. [108] performed stepped-heterodyne measurements of the complex optical spectra of single-section MLLDs under different operating conditions to analyze their group delay dispersion. They found a simple empirical formula that relates the group delay dispersion to the 10 dB-bandwidth of the device. They defined the phase of the k-th mode as [108]

$$\varphi_k = \frac{1}{2} \cdot D_2 \cdot \left[2\pi \cdot (f_k - f_0) \right]^2 , \tag{2.19}$$

where f_0 is the central frequency of the MLLD spectrum and D_2 is the group delay dispersion. For this definition, they empirically found that [108]

$$D_2 = \frac{1}{2\pi \cdot \Delta f_{\text{env}} \cdot F} , \tag{2.20}$$

where f_{env} is the 10 dB-bandwidth of the laser spectrum and F is the free spectral range. An interesting interpretation of this empirical result can be found by looking at the outer two modes. Since they are located Δf_{env} apart, the difference of their group delays is

$$\Delta\tau_{\text{gr}} = 2\pi \cdot D_2 \cdot \Delta f_{\text{env}} = \frac{1}{F} . \tag{2.21}$$

This is equivalent to saying that the "difference in group delays experienced by the two modes at the frequency extrema of the MLL spectrum [...] equal the cavity round-trip time" [108].

To analyze the effect of laser chirp on the detected terahertz spectrum, we can use O'Duill's empirical formula for the group delay dispersion as the maximum chirp one can expect to experience. By applying the notations from Section 2.1, we get

$$D_2 = \frac{1}{2\pi N F^2} \tag{2.22}$$

and

$$\varphi_k = \frac{1}{2} \cdot D_2 \cdot (2\pi k F)^2 \tag{2.23}$$
$$= \frac{\pi}{N} \cdot k^2 \, .$$

By introducing a chirp coefficient $c \in [0, 1]$, the effect of different amounts of chirp can now be analyzed:

$$\varphi_k = c \cdot \frac{\pi}{N} \cdot k^2 \, , \; 0 \leq c \leq 1 \, . \tag{2.24}$$

To keep it simple, only the case of an MLLD whose modes all have the same amplitude $E_k \equiv E_0 \; \forall \; k$ is considered.

Influence of pulse chirp on the emitted terahertz spectrum

First, the emitted terahertz spectrum is analyzed. Since it was found that the radiated terahertz field is proportional to the filtered instantaneous optical power of the incident light, we can gauge the influence of the optical spectrum on the emitted terahertz spectrum by defining a normalized amplitude for the spectral component of the filtered instantaneous optical power at the angular frequency $m\Omega$. Evaluating the weights of the Dirac delta functions within the inner sum in Equation (2.4) yields the normalized amplitude of the spectral component at the normalized frequency m:

$$A_{p_{\mathrm{opt}},m} = \left| \sum_{k=m}^{N-1} E_0^2 \cdot \mathrm{e}^{\mathrm{j}(\varphi_k - \varphi_{k-m})} \right| \, . \tag{2.25}$$

Inserting Equation (2.24) into Equation (2.25) yields

$$A_{p_{\mathrm{opt}},m} = \left| \sum_{k=m}^{N-1} E_0^2 \cdot \mathrm{e}^{\mathrm{j} \cdot c \cdot \frac{\pi}{N} \cdot \left[k^2 - (k-m)^2 \right]} \right| \, . \tag{2.26}$$

A numerical evaluation of the normalized amplitudes $A_{p_{\mathrm{opt}},m}/(N-1)$ is depicted in Figure 2.2. Plot (a) shows the normalized amplitudes as a function of the normalized frequency m for different values of the chirp coefficient c, whereas plot (b) shows the normalized amplitudes as a function of the chirp coefficient c for different values of the normalized frequency m.

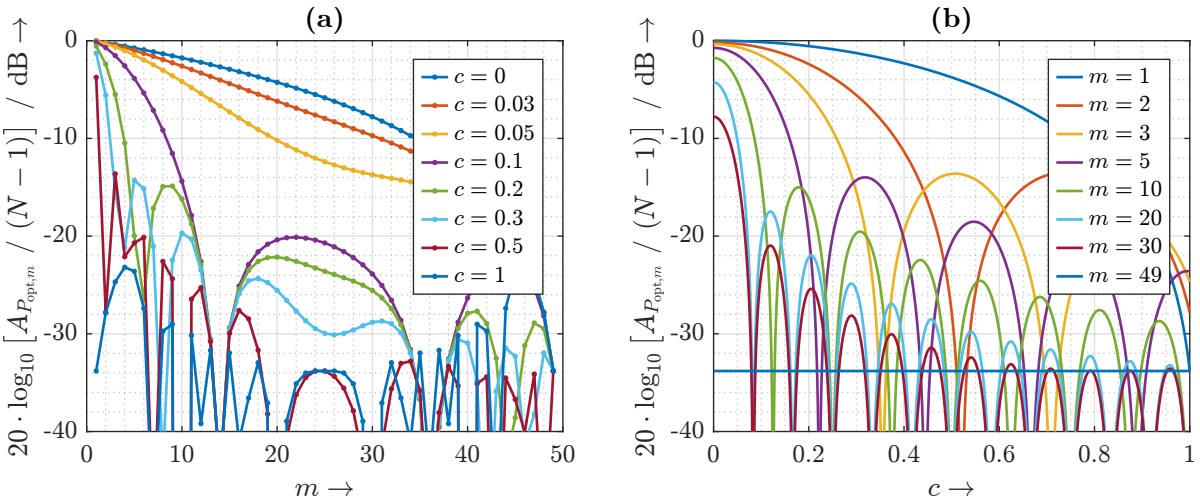

Figure 2.2: Normalized amplitudes $A_{p_{\mathrm{opt}},m} \,/\, (N-1)$ of the spectral components of the filtered instantaneous optical power for $N = 50$ **(a)** as a function of the normalized frequency m for different values of the chirp coefficient c and **(b)** as a function of the chirp coefficient c for different values of the normalized frequency m.

The case $c = 0$ in plot (a) represents the case without any chirp. This case shows that the emitted amplitude rolls off towards higher frequencies due to the decreasing number of constructively superimposed beat tones. An increasing amount of chirp leads to a frequency-dependent reduction of the emitted amplitudes. For small amounts of chirp ($c < 0.1$), the frequency dependence is relatively mild, whereas for large amounts of chirp ($c \geq 0.1$) the frequency dependence is severe. For very large amounts of chirp, the interference between the beat tones is almost perfectly destructive.

The chirp dependence of select frequencies is highlighted in plot (b). Most notable are the normalized frequencies $m = 1$ and $m = 49$. For the lowest-frequency component $m = 1$, we can observe a monotonic decrease with increasing chirp. For $c = 1$, i.e. without any chirp compensation, the amplitude for $m = 1$ drops to $1/(N-1)$. This can be easily explained. For $c = 1$, the phase shift between the beat tones of adjacent pairs of laser modes is equal to π. In the case of 50 modes, the beat tones of 48 pairs of laser modes interfere destructively, and only the beat tone of a single pair of modes remains. The highest-frequency component ($m = N - 1 = 49$) on the other hand results from the beating of only the outer two modes of the laser spectrum and is thus independent of the chirp.

Influence of pulse chirp on the detected terahertz spectrum

Next, the detected terahertz spectrum is analyzed. As discussed in Section 2.1, the influence of the optical spectrum on the detected terahertz spectrum is determined by the amplitudes A_m. Inserting Equation (2.24) into Equation (2.15), we get

$$\begin{aligned} A_m &= \sum_{k=m}^{N-1} \sum_{l=m}^{N-1} E_0^4 \cdot \cos\left\{ c \cdot \frac{\pi}{N} \cdot \left[k^2 - (k-m)^2 - l^2 + (l-m)^2 \right] \right\} \\ &= \sum_{k=m}^{N-1} \sum_{l=m}^{N-1} E_0^4 \cdot \cos\left[c \cdot \frac{\pi}{N} \cdot m \cdot (k-l) \right] \ , \ m = 0 \ldots N-1 \ . \end{aligned} \tag{2.27}$$

I have shown in Ref. [1] that by using the Dirichlet kernel this can be rewritten in the closed form

$$A_m = E_0^4 \cdot \left\{ \frac{\sin\left[\frac{1}{2} \cdot c \cdot \frac{\pi}{N} \cdot m \cdot (m-N) \right]}{\sin\left[\frac{1}{2} \cdot c \cdot \frac{\pi}{N} \cdot m \right]} \right\}^2 \ , \ m = 0 \ldots N-1 \ . \tag{2.28}$$

A numerical evaluation of the normalized amplitudes $A_m / (N-1)^2$ is depicted in Figure 2.3. The behavior is similar to the amplitudes of the emitted spectrum depicted in Figure 2.2, with a few notable differences.

In plot (a), we can see that the high frequency roll-off is steeper than for the emitted spectrum. This is easy to understand given that the detected spectrum results from the beating process occurring both in the emitter and detector. In plot (b), it can be observed that the chirp dependence of the lowest-frequency component $m = 1$ of the detected spectrum is much less than that of the emitted spectrum. Considering Equation (2.15), this can be attributed to the fact that the double sum introduces summands with various combinations of the phases φ_k, φ_{k-m}, φ_l, and φ_{l-m}.

2.2.2 Influence of the number of modes

Another important aspect that can be analyzed given the theoretical results is the influence of the number of laser modes. Practically, the average optical power that is allowed to be incident on the terahertz emitter and detector is limited by the damage threshold $P_{\max}$ of the photodiode and photoconductor, respectively. For the purposes

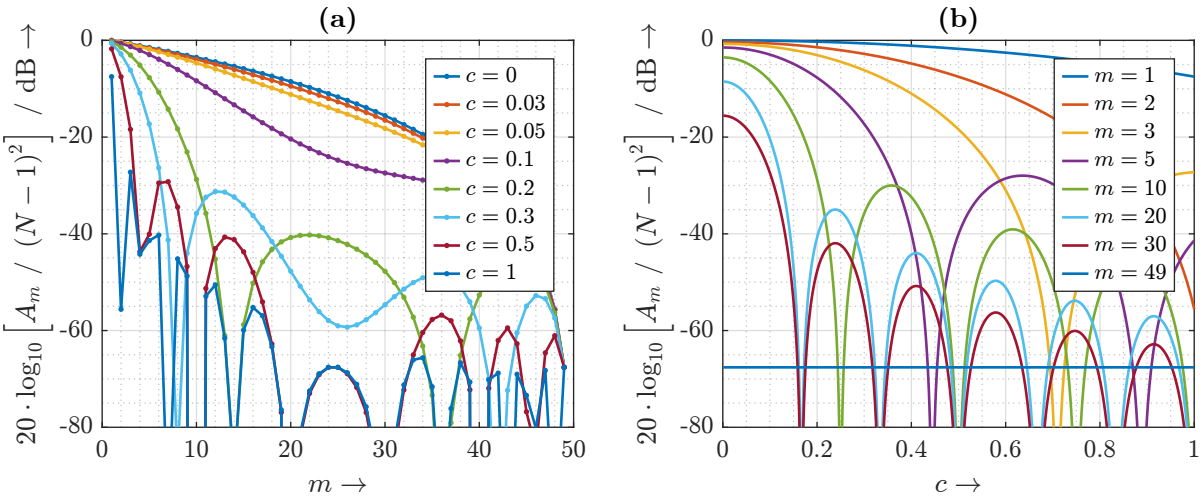

Figure 2.3: Normalized amplitudes $A_m \;/\; (N-1)^2$ of the spectral components of the detected terahertz spectrum for $N = 50$ **(a)** as a function of the normalized frequency m for different values of the chirp coefficient c and **(b)** as a function of the chirp coefficient c for different values of the normalized frequency m.

of this analysis, both damage thresholds are assumed to be identical. It is thus instructive to consider the case of a flat optical spectrum with $E_k \equiv E_0 = \sqrt{P_{\max}/N}$. In this case, Equation (2.25) simplifies to

$$A_{p_{\text{opt}},m} = \sum_{k=m}^{N-1} \frac{P_{\max}}{N} = \frac{N-m}{N} \cdot P_{\max} \tag{2.29}$$

and Equation (2.27) simplifies to

$$A_m = \sum_{k=m}^{N-1} \sum_{l=m}^{N-1} \left(\frac{P_{\max}}{N}\right)^2 = \frac{(N-m)^2}{N^2} \cdot {P_{\max}}^2 \,. \tag{2.30}$$

A numerical analysis of these results is depicted in Figure 2.4. The plots show the amplitudes of select components of the emitted and detected terahertz spectra as a function of the number of laser modes N. The amplitudes are normalized to the average optical power $P_{\max}$ and its square ${P_{\max}}^2$, respectively. We can draw several important

conclusions from these results. The normalized amplitudes monotonically increase with the number of modes and converge to 1 for $N \to \infty$. Thus, the spectrum of the MLLD should be as dense and as wide as possible in order to maximize both the emitted and detected amplitudes.

The case $m = 1$ is particularly interesting. It can be seen that for $N = 2$ the emitted and detected amplitudes are 6 dB and 12 dB lower than the optimum, respectively. This means that

(a) the emitted amplitude at the fundamental frequency is up to 6 dB higher if an MLLD is used compared to two single-mode laser diodes. Thus, a terahertz communication system driven by an MLLD whose repetition rate is equal to the desired carrier frequency has a higher transmit power than a system driven by two single-mode laser diodes with the same combined average optical power.

(b) the detected amplitude at the fundamental frequency is up to 12 dB higher if an MLLD is used compared to two single-mode laser diodes. This puts UHRR-THz-TDS at an advantage over THz-FDS.

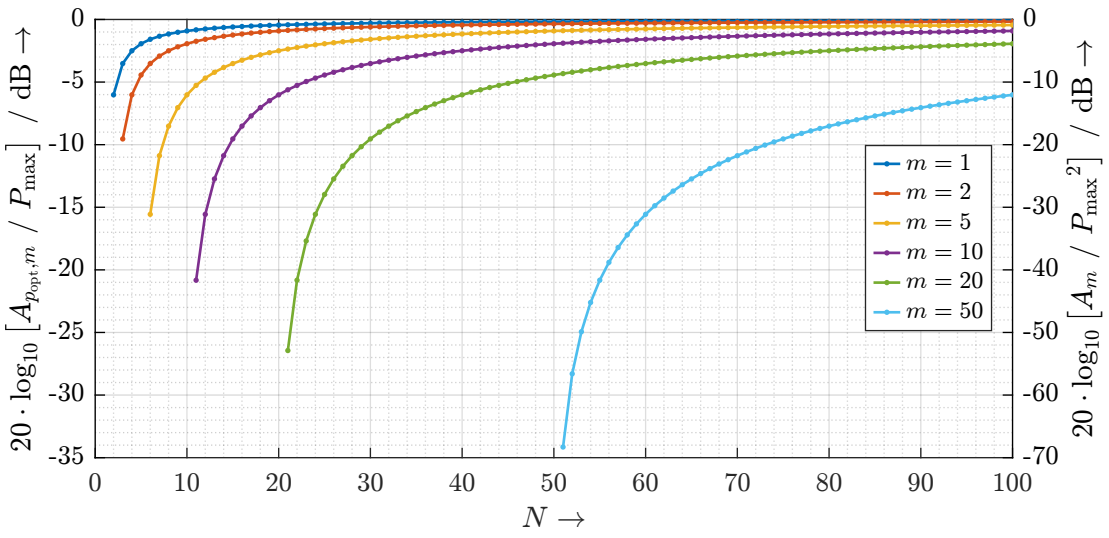

Figure 2.4: Left axis: Normalized spectral amplitudes $A_{p_{\mathrm{opt}},m} \,/\, P_{\mathrm{max}}$ of the emitted terahertz spectrum as a function of the number of laser modes N. Right axis: Normalized spectral amplitudes $A_m \,/\, {P_{\mathrm{max}}}^2$ of the detected terahertz spectrum as a function of the number of laser modes N.

2.3 Experimental results

I have shown an extensive experimental validation of the system-theoretical model in Ref. [1]. For the sake of conciseness, only a short summary of the findings is reproduced here. Details about the experimental methods as well as further results can be found in Ref. [1].

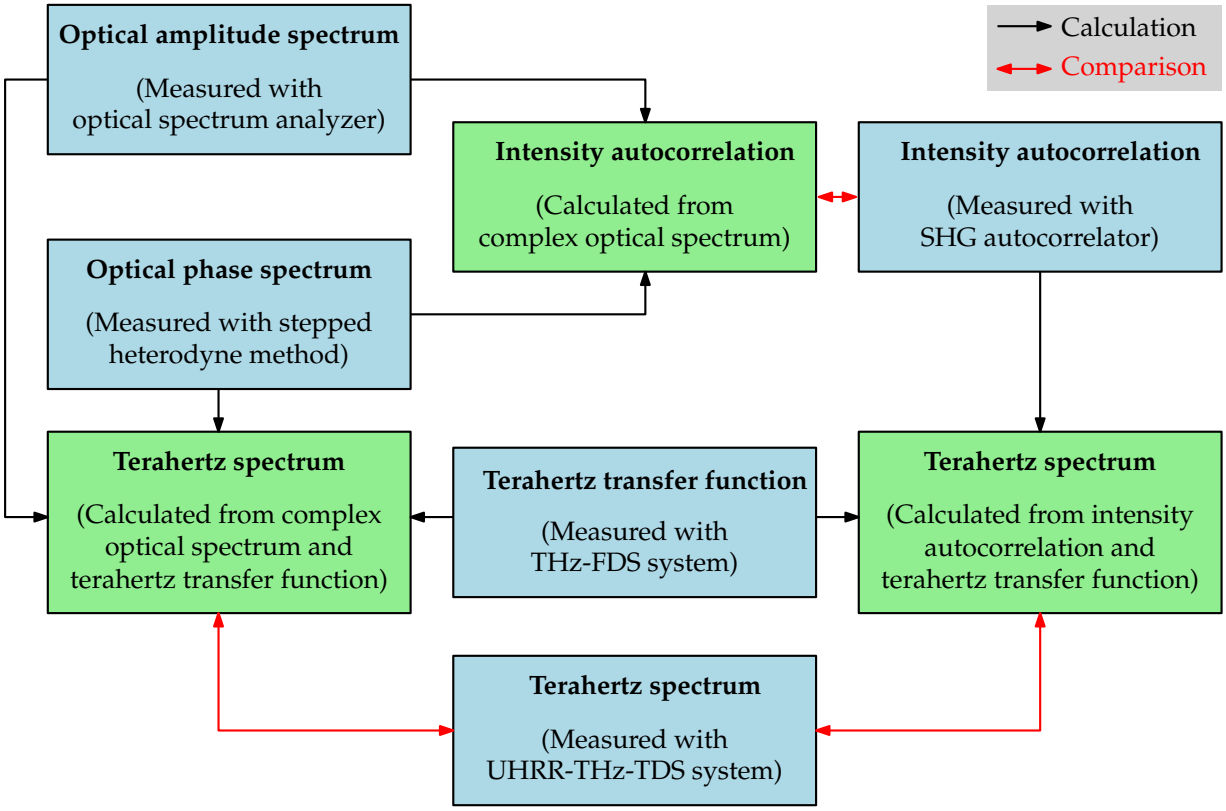

Figure 2.5: Concept for experimental validation of the system-theoretical model of UHRR-THz-TDS. Blue boxes indicate measured quantities. Green boxes indicate calculated quantities.

The concept for experimental validation of the system-theoretical model is sketched in Figure 2.5. Measured quantities are indicated by blue boxes, calculated quantities are indicated by green boxes. The main objectives are the validation of Equations (2.15), (2.16), and (2.18) as well as the confirmation of the relationship between the optical intensity autocorrelation and the detected terahertz spectrum. To that end, all the relevant quantities are measured and calculated with various optical amplitude and phase spectra. These different spectra are generated by using two different MLLDs and us-

ing different lengths of single-mode fiber between the MLLD and the measurement setup to (partially) compensate their inherent chirp. The first MLLD was the Thorlabs FPL1009P mentioned in Section 1.2.3. The second MLLD was a two-section QD laser diode from Fraunhofer Heinrich Hertz Institute (HHI) in Berlin. Here, only results for the latter are shown. The quantities that are independent of the optical phase spectrum (i.e. independent of the single-mode fiber length) are depicted in Figure 2.6. The quantities that depend on the optical phase spectrum are depicted in Figures 2.7 through 2.10.

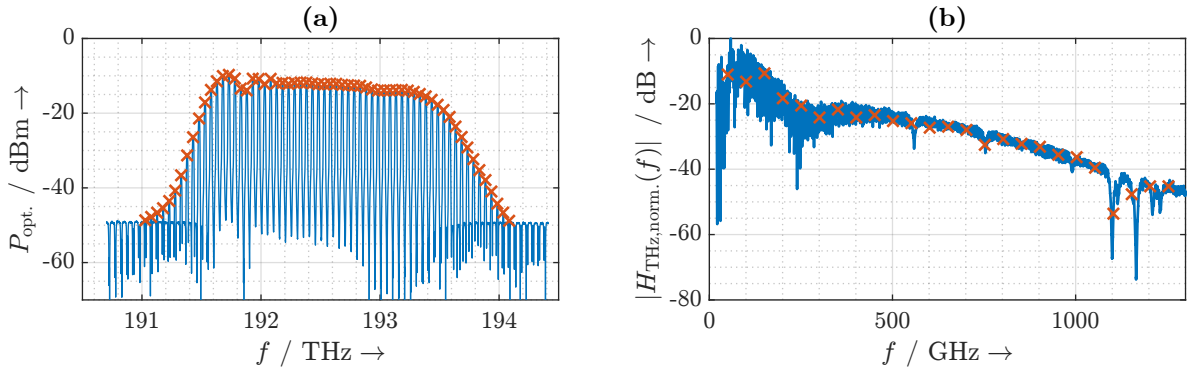

Figure 2.6: **(a)** Optical amplitude spectrum. The continuous blue line indicates the spectrum measured with the optical spectrum analyzer. The red crosses indicate the peaks within the 40 dB-bandwidth. **(b)** Transfer function of the terahertz system. The continuous blue line indicates the transfer function measured with the THz-FDS system. The red crosses indicate the values of the transfer function at $f = mF$.

Figure 2.6 (a) shows the optical amplitude spectrum of the MLLD measured with an optical spectrum analyzer (*Anritsu MS9740A*). The MLLD exhibits 62 modes within a 40 dB bandwidth with a free spectral range of $F \approx 50.14\,\mathrm{GHz}$. Figure 2.6 (b) depicts the transfer function of the terahertz system measured with a commercially available THz-FDS system (*Toptica Terascan 1550*). The transfer function is measured with a frequency resolution of 10 MHz, making it possible to accurately determine the values $|H_{\mathrm{THz}}(m\Omega)|$.

In the following, the results obtained with single-mode fiber lengths of $L = 0\,\mathrm{m}$ (virtually no chirp compensation), $L = 25\,\mathrm{m}$ (partial chirp compensation), and $L = 50\,\mathrm{m}$ (nearly perfect chirp compensation) are considered. Figure 2.7 depicts the optical phase spectra measured with the stepped-heterodyne technique proposed in Ref. [109].

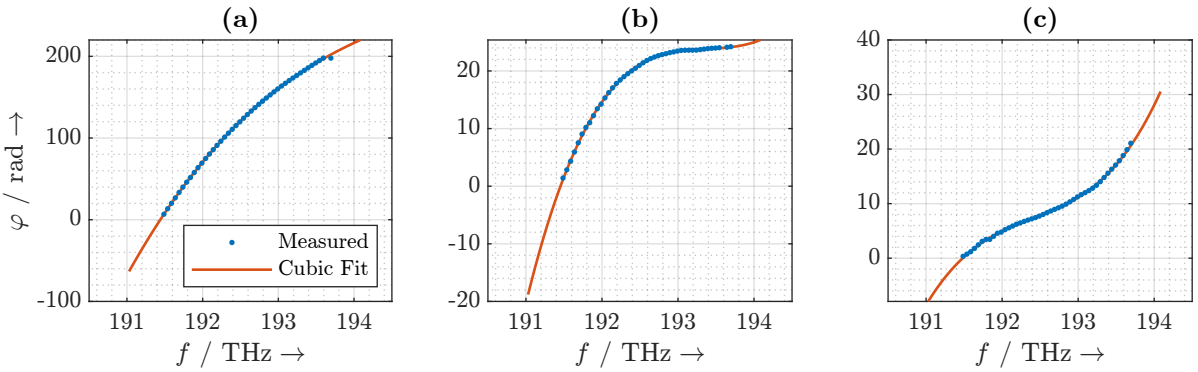

Figure 2.7: Optical phase spectra measured with the stepped-heterodyne method with single-mode fiber lengths of **(a)** 0 m, **(b)** 25 m, and **(c)** 50 m, respectively. The blue dots indicate the measured points. The red line represents a cubic fit of the measured phase values.

The measured data points are indicated by blue dots, and a cubic fit is depicted by a continuous red line.

Figure 2.8 shows the intensity autocorrelation calculated according to Equations (2.15) and (2.18) in red as well as the intensity autocorrelation measured with an SHG autocorrelator (*APE pulseCheck*). Figure 2.9 shows the Fourier transforms of these quantities. In the delay domain, it can be seen that the nearly perfectly chirp-compensated case leads to a narrow pulse with a full width at half maximum (FWHM) of approximately 750 fs.

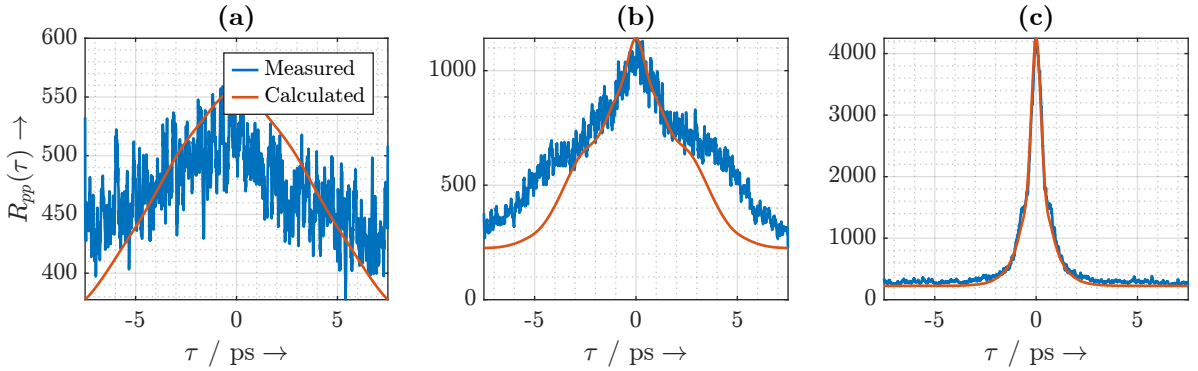

Figure 2.8: Intensity autocorrelation functions with single-mode fiber lengths of **(a)** 0 m, **(b)** 25 m, and **(c)** 50 m, respectively. The blue line represents the autocorrelation function measured with an SHG autocorrelator. The red line represents the autocorrelation function calculated from the complex optical spectrum.

Its Fourier transform, whose spectral amplitudes are equal to the amplitudes A_m according to Equation (2.18), exhibits a 40 dB bandwidth of about 1.8 THz. The uncompensated and partially compensated case exhibit a distorted pulse shape with a significantly wider pulse width and lower pulse amplitude. Their Fourier transforms show a much steeper drop-off towards higher frequencies than the well-compensated case. All plots show a good match between the calculated and the measured data. Notably, without chirp compensation or with only partial chirp compensation, there is a strong frequency selectivity. This confirms the predictions from the numerical analysis shown in Figure 2.3.

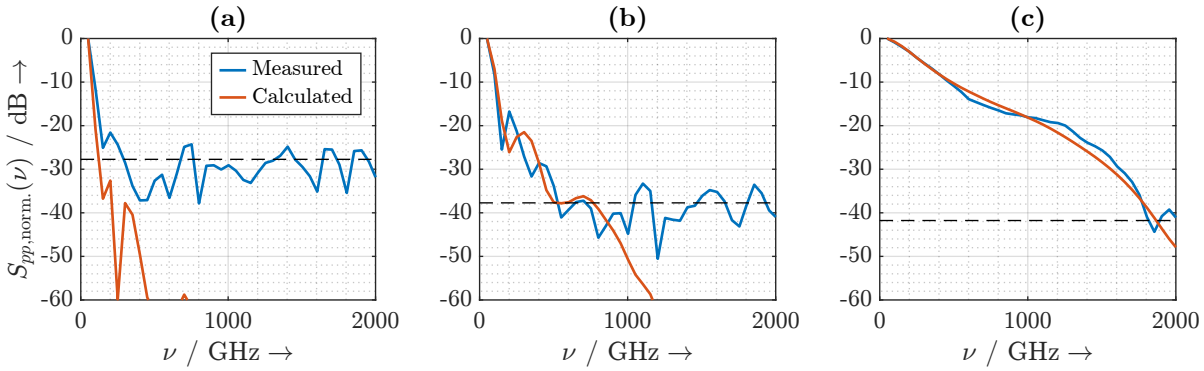

Figure 2.9: Fourier transform of the intensity autocorrelation functions with single-mode fiber lengths of **(a)** 0 m, **(b)** 25 m, and **(c)** 50 m, respectively. The blue line represents the Fourier transform of the autocorrelation function measured with an SHG autocorrelator. The red line represents the Fourier transform of the autocorrelation function calculated from the complex optical spectrum. The dashed black line indicates the measurement noise floor.

Figure 2.10 depicts several representations of the detected terahertz spectra. The continuous blue lines indicate the spectra measured with the UHRR-THz-TDS system. The red crosses mark the peaks of the spectral components. The yellow circles represent the spectral amplitudes calculated from the complex optical spectrum and the transfer function of the terahertz system. The purple squares indicate the spectral amplitudes calculated from the measured intensity autocorrelation and the transfer function of the terahertz system. The red, yellow, and purple plots show a remarkable agreement between the calculated and the measured spectra. In the well-compensated case, we can identify spectral components above the noise floor up to 1.3 THz. In the other cases, the bandwidth is severely reduced and a few spectral components are completely canceled.

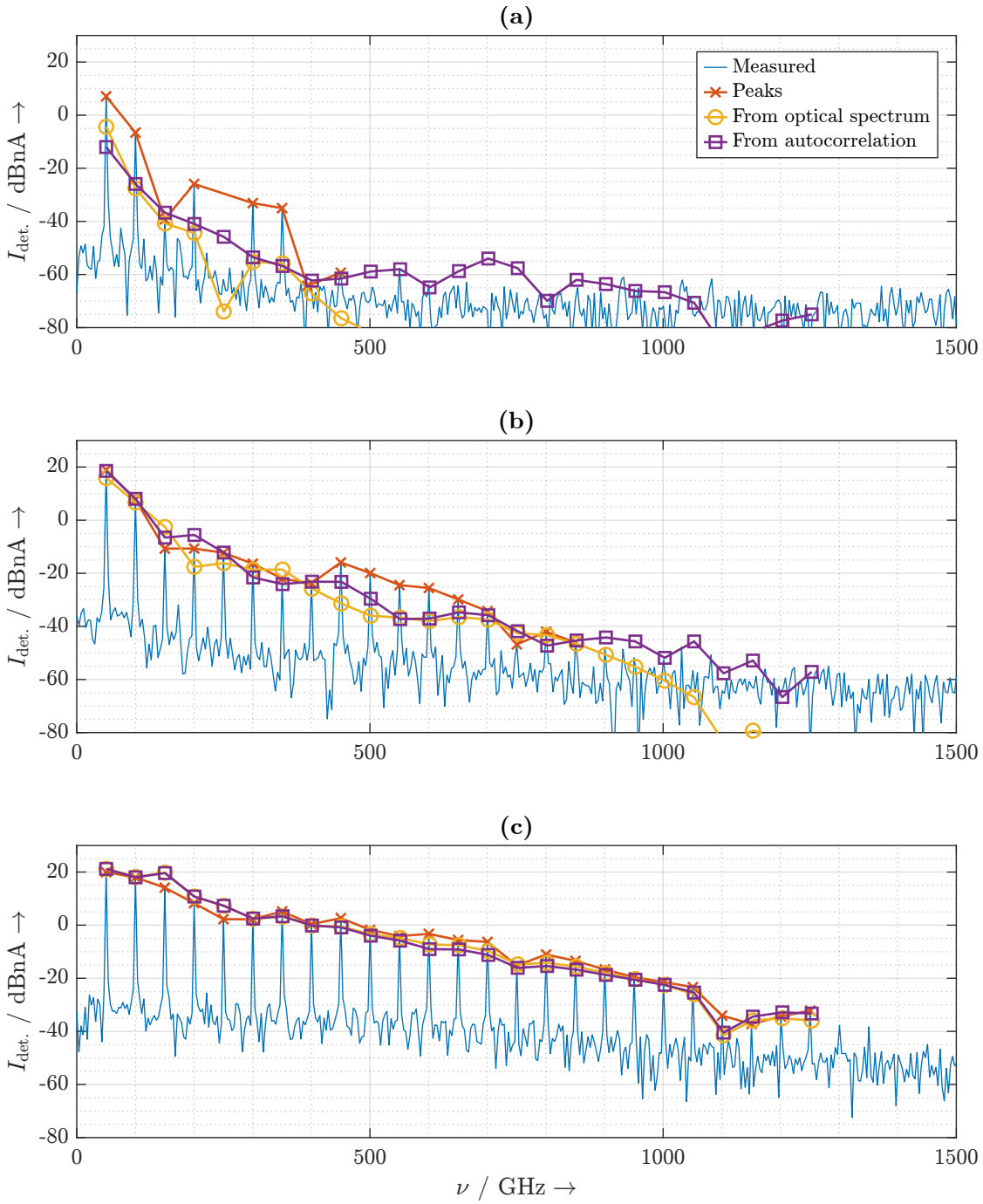

Figure 2.10: Detected terahertz spectra with single-mode fiber lengths of **(a)** 0 m, **(b)** 25 m, and **(c)** 50 m, respectively. The continuous blue lines indicate the spectra measured with the UHRR-THz-TDS system. The red crosses mark the peaks of the spectral components. The yellow circles represent the spectral amplitudes calculated from the complex optical spectrum and the transfer function of the terahertz system. The purple squares indicate the spectral amplitudes calculated from the measured intensity autocorrelation and the transfer function of the terahertz system.

CHAPTER

THREE

COMPARISON BETWEEN THZ-TDS, THZ-CCS, AND UHRR-THZ-TDS

In Chapter 1, first the conventional (typically fiber laser-driven) THz-TDS approach has been introduced and then two closely related alternative approaches have been discussed separately: THz-CCS using either an MMLD or an SLD as the light source and UHRR-THz-TDS using an MLLD as the light source. The detailed system-theoretical analysis of UHRR-THz-TDS in Chapter 2 has provided hints that these approaches are in fact quite complementary. In this chapter, it is attempted to provide a comprehensive comparison of these approaches based on typical spectral and coherence properties of the different light sources. Subsequently, this comparison is used to discuss the suitability of theses approaches for different applications.

3.1 Spectral and coherence properties of the light sources

	Fiber laser	MLLD	MMLD	SLD
Spectral width	> 10 THz	< 3 THz	< 3 THz	> 5 THz
Pulse width	< 100 fs	> 600 fs	n/a	n/a
Mode spacing	$\ll 1$ GHz	> 10 GHz	> 10 GHz	n/a
Apparent coherence length	Long	Long	Short	Virtually none

Table 3.1: Spectral and coherence properties of the considered light sources.

A summary of the spectral and coherence properties of the four light sources is given in Table 3.1. Fiber lasers and MLLDs are both mode-locked. Their spectra exhibit distinct modes with a small linewidth. With the proper chirp compensation, they emit optical pulses whose repetition rate is given by the spacing of the modes. The major difference between fiber lasers and MLLDs is in their spectral width and mode spacing, in other words their pulse width and repetition rate. While MMLDs also exhibit a mode structure, these modes are not locked and thus exhibit very large linewidths. Consequentially, the generated terahertz signals also exhibit a large linewidth. Moreover, because of the lack of mode locking, the phase relationship between the modes is random and rapidly changing, so that the emitted optical signal is not pulsed. MLLDs and MMLDs however have somewhat similar spectral widths and mode spacings. SLDs do not have a cavity and thus emit a noise-like optical signal with no mode structure.

Apparent coherence length

The coherence length is strictly defined only for single-mode lasers in terms of the interference behavior between two laser beams that travel different distances before being combined. Although it is oftentimes hand-wavingly explained as the distance after which the beams "no longer produce interference fringes" and it is commonly accepted that the coherence length is inversely proportional to the linewidth of the laser, the exact quantitative definition has been subject to much debate [110]. A useful and straightforward definition of coherence length is the propagation distance corresponding to the delay after which the envelope of the field autocorrelation function drops to

1/e its maximum value [6]. The field autocorrelation function of a single-mode laser is illustrated in Figure 3.1.

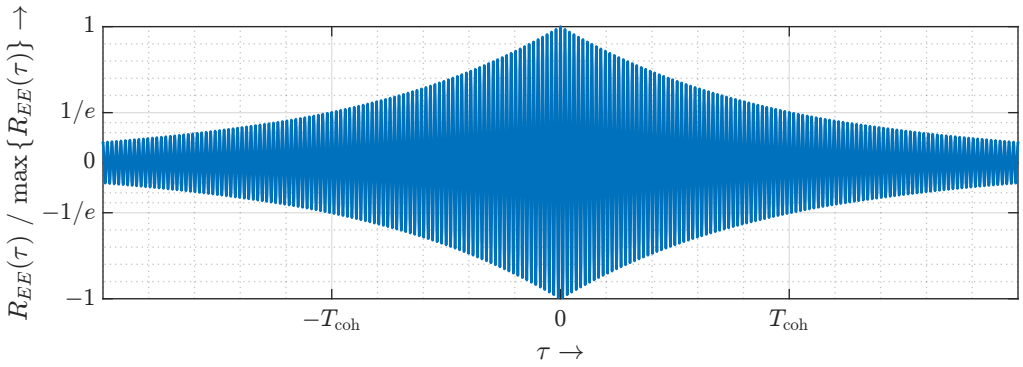

Figure 3.1: Qualitative field autocorrelation function of a single-mode laser. For illustrative purposes, an unusually short coherence time T_{coh} is depicted.

A mode-locked laser, be it a fiber laser or MLLD, simultaneously emits several longitudinal modes. All modes are emitted practically continuous-wave, so that their linewidths are in the ballpark of that of a single-mode laser. However, the common definition of the coherence length is not useful, as can be seen from the qualitative autocorrelation functions illustrated in Figure 3.2. The plot shows a simulated field autocorrelation function in blue and the corresponding intensity autocorrelation function in red.

The intensity autocorrelation function consists of repetitive pulses with the following relationships to the optical spectrum:

- The pulse width is inversely proportional to the width of the optical spectrum.
- The repetition period is inversely proportional to the free spectral range.
- The decay rate of the envelope of the pulse maxima is related to the linewidths of the longitudinal modes.

For the discussion in this section, the rate of decay of the envelope of the pulse maxima is of particular importance. Thus, the definition of an "apparent" coherence length

[6] The field autocorrelation function is traditionally measured with an unbalanced Michelson interferometer. Because the Fourier transform of the interferogram is equal to the optical spectrum according to the Wiener-Khinchin theorem, this apparatus is commonly called a "Fourier transform spectrometer".

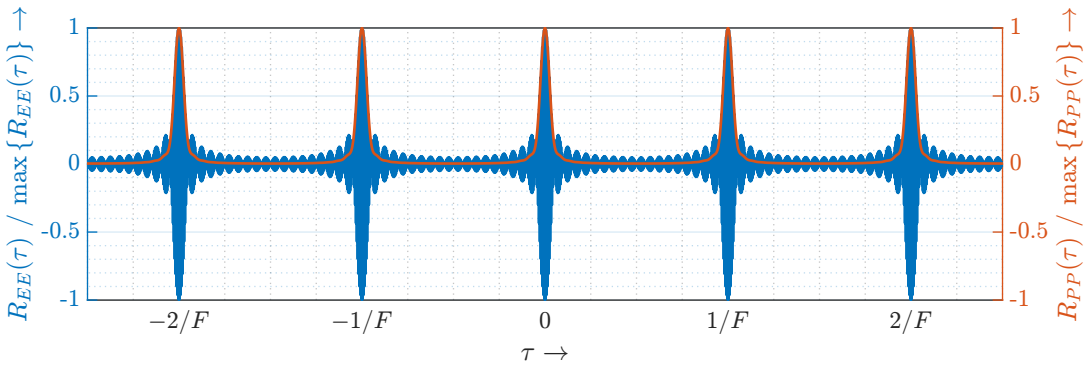

Figure 3.2: Illustrative field (blue) and intensity (red) autocorrelation function of a mode-locked laser.

introduced by Reisinger et al. [111] in 1979 appears to be very useful. The apparent coherence length is defined as the propagation distance after which the envelope of the field autocorrelation function has decayed to 1/e its maximum value. For a mode-locked laser, the apparent coherence length can be in the range of meters to hundreds of meters.

This concept is extended to MMLDs and SLDs by the qualitative autocorrelation functions illustrated in Figures 3.3 and 3.4, respectively. Because of the lack of mode-locking, the linewidths exhibited by MMLDs are orders of magnitude higher than those of MLLDs. Thus, the envelope decays much faster and we observe apparent coherence lengths in the centimeter range. SLDs emit broadband incoherent light, so that their autocorrelation functions exhibit a single coherence spike at $\tau = 0$.

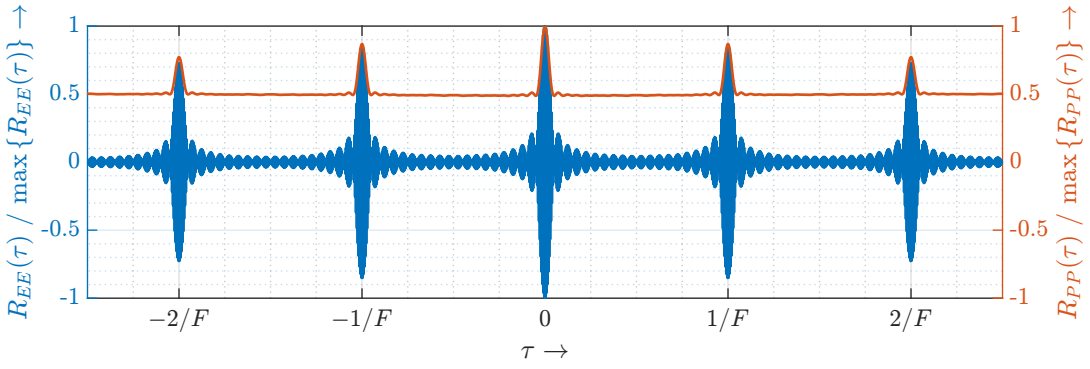

Figure 3.3: Illustrative field (blue) and intensity (red) autocorrelation functions of a multi-mode laser.

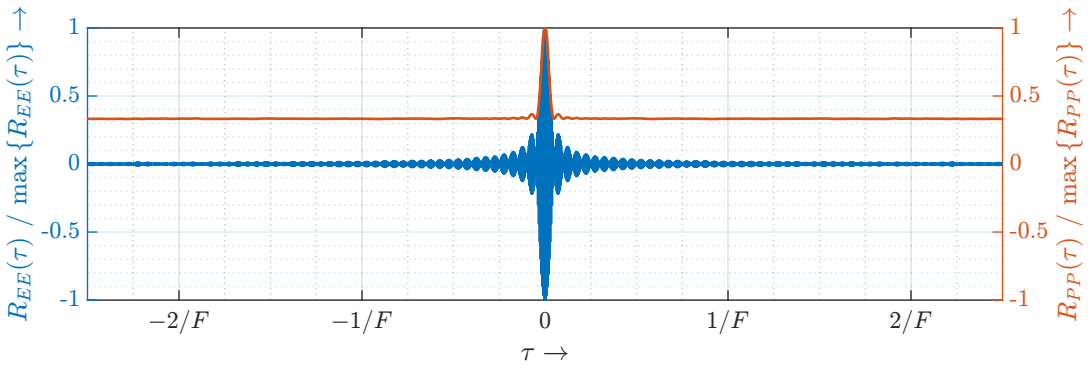

Figure 3.4: Illustrative field (blue) and intensity (red) autocorrelation functions of a superluminescent diode.

3.2 Practical implications of the properties of the light sources

In this section, the implications of the spectral and coherence properties as well as the physical properties of the light sources are discussed in four areas of practical interest: Spectroscopy, synthetic aperture radar (SAR) imaging, use in a distributed sensing system, and monolithic integration. A summary of these implications and a qualitative comparison are given in Table 3.2.

3.2.1 Spectroscopy

In this context, the term "spectroscopy" refers to sensing systems that operate in a relatively static configuration (typically in transmission mode) and rely on spectral information to characterize or classify materials. The most relevant parameters for these applications are the bandwidth and spectral resolution of the system.

As discussed at great length, the spectral width of the light source and the efficiency of the generation and detection processes influence the usable bandwidth of the terahertz system. This puts fiber laser-driven THz-TDS systems with bandwidths of several THz distinctly above the other approaches. UHRR-THz-TDS and SLD-driven THz-CCS systems follow with maximum bandwidths around 1.5 THz, and MMLD-driven systems trail close behind.

The maximum achievable spectral resolution is determined by the mode spacing of the

light source. Being mode-less, SLD-driven THz-CCS systems have virtually unlimited frequency resolution, followed by fiber laser-driven THz-TDS systems with sub-GHz frequency resolution. The frequency resolution of these systems is typically limited by the length of the ODU. UHRR-THz-TDS and MMLD-driven THz-CCS systems have a much worse spectral resolution of the order of several ten gigahertz.

3.2.2 Synthetic aperture radar imaging

An up-and-coming application of THz-TDS is SAR imaging. The use of the SAR principle with a commercial THz-TDS system was first demonstrated in our lab by Damyanov et al. [15]. Because this approach does not require any collimating or focusing optics, it is commonly referred to as "lensless" imaging. In a sense, the focusing of the image is performed in software by a back-projection algorithm. This leads to a very simple and flexible setup and has the advantage that the object under test does not have to be placed in the focus of an imaging system. Basically, the emitter and detector are placed besides each other, and both roughly face the object under test. By moving the antennas relative to the object under test (or vice versa), measurements are performed over a synthetic aperture. In a recent publication [13], I have demonstrated the use of the SAR principle with UHRR-THz-TDS and shown that this approach allows us to resolve sub-millimeter sized features [7].

There are four parameters of the photonic system that have a particularly strong influence on the behavior and performance of the imaging system:

- The bandwidth determines the range resolution.
- The dynamic range influences the distances, sizes, shapes, and materials of objects that can be detected.
- The field of view determines the distance range within which objects can be detected.
- The unambiguous range determines the distance range within which no ambiguity occurs.

[7] I would like to thank M. Sc. Dilyan Damyanov for implementing the back-projection algorithm.

As previously discussed, the detected amplitude of systems with mode-locked light sources is higher than that of incoherent light sources, and for mode-locked light sources the detected amplitude increases with the number of modes. In the first approximation, the dynamic range is proportional to the detected amplitude. Thus, fiber laser-driven systems have the highest dynamic range, followed by MLLD-driven systems.

To investigate the field of view and unambiguous range, we consider the vastly simplified block diagram of a prototype terahertz system depicted in Figure 3.5. The length L_{remote} represents the length of the fiber that connects the light source to the terahertz system. The lengths L_{Tx} and L_{Rx} represent the fiber lengths from the splitter to the emitter and detector, respectively. The length $L_{\text{ODU}}(\tau_0 + \tau)$ represents the variable length of the ODU, and the length L_{THz} represents the total length of the RF path from the emitter to the detector.

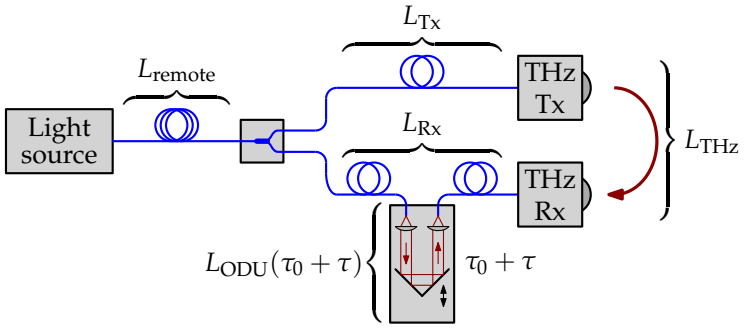

Figure 3.5: Simplified block diagram of a photonic terahertz system including all relevant lengths within the setup.

If we regard the system as an intensity autocorrelator, the zero point (and thus the maximum) of the autocorrelation function is at $L_{\text{Tx}} + L_{\text{THz}} = L_{\text{Rx}} + L_{\text{ODU}}(\tau_0)$. The autocorrelation function is then scanned with the variable delay τ of the ODU. While in static measurement scenarios, such as transmission-mode spectroscopy, the fiber lengths can be adjusted according to the length of the RF path such that the zero point of the autocorrelation falls within the delay range of the ODU, this may not be possible in SAR imaging. The round-trip path length from the emitter to the object under test and back to the detector may not be known *a priori* and may vary in use. Depending on the light source, this can have different effects:

- **Fiber laser:** Since the modes of a fiber laser are typically spaced much less than 1 GHz apart, the distance between the maxima of the autocorrelation is much greater than 30 cm. For most practical ODUs, this can possibly result in no autocorrelation maximum appearing within its delay range.
- **MLLD:** The modes of an MLLD are typically spaced more than 10 GHz apart, i.e. the distance between the maxima of the autocorrelation is typically less than 3 cm, which is within the range of most ODUs. Thus, supported by the long apparent coherence length of the MLLD, it is always possible to measure a pulse independent of the round-trip path length of the RF path.
- **MMLD:** The case of an MMLD is similar to that of an MLLD, however, the envelope of the autocorrelation function decays much faster, so that a significant loss of signal amplitude is observed as the distance to the zero point is increased.
- **SLD:** The autocorrelation of the SLD only has a single maximum in the zero point. Thus, a path length offset that is larger than the range of the ODU leads to no usable signal being observed.

While the field of view of UHRR-THz-TDS vastly exceeds that of the other approaches, this comes at the cost of a very short unambiguous range of $c_0/(2F)$. I have investigated the effects of the short unambiguous range in Ref. [13]. An illustrative extract of the results is depicted in Figures 3.6 and 3.7.

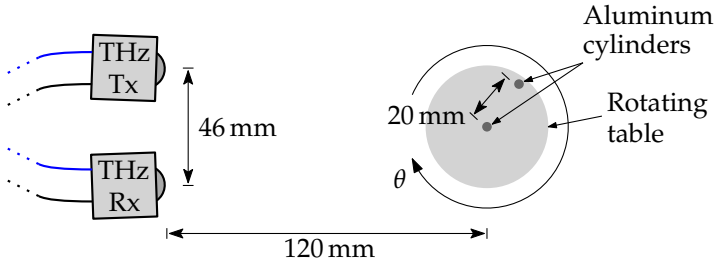

Figure 3.6: Sketch of the measurement setup for SAR imaging of two aluminum cylinders.

Figure 3.6 shows a sketch of the top-view of the measurement setup. The object under test consists of two aluminum cylinders with a height of 25 cm and a diameter of 4 mm that are placed vertically on a motorized rotation stage at a distance of about 12 cm from the terahertz emitter and detector. One of the cylinders is placed roughly in the center of the rotation stage, whereas the other cylinder is placed 20 mm off-center.

The resulting radargram after normalization against a reference reflector is depicted in Fig. 3.7 (a) [8]. We can identify two practically continuous lines that are repeated every $1/F \approx 20\,\text{ps}$. The line with the small delay amplitude represents the cylinder that is roughly in the center of rotation, whereas the line with the large delay amplitude represents the cylinder that is 20 mm off-center. We can also see that the two objects shadow each other after every 180° rotation. The resulting image after application of the back-projection algorithm is depicted in Figure 3.7 (b). The image shows two distinct circles with a radius of 4 mm as well as several ghost images caused by the ambiguity of the system. The resolution of this ambiguity will be of significant interest for future work.

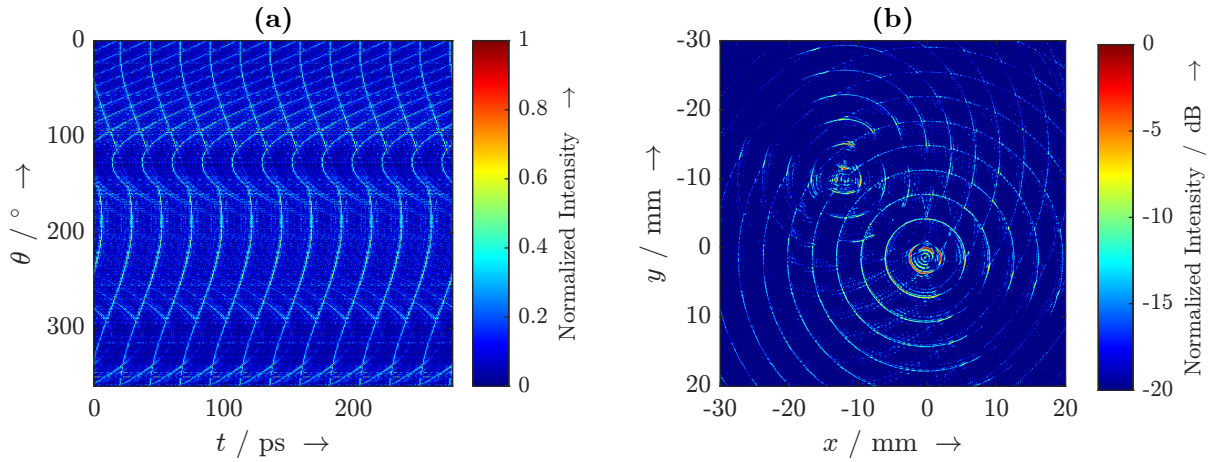

Figure 3.7: (a) Repeated radargram for the two aluminum cylinders. **(b)** SAR image of the two aluminum cylinders.

3.2.3 Distributed sensing system

As discussed in Section 2.1, mode-locked laser sources require a precisely chosen length of single-mode fiber between the light source and the emitter respectively detector for pulse compression, i.e. the lengths $L_{\text{remote}} + L_{\text{Tx}}$ and $L_{\text{remote}} + L_{\text{Rx}}$ have to be matched to the chirp of the light source with sub-meter precision. This puts a limit on the maximum distance between the light source and the emitter respectively detector. This can

[8] Since the frequency resolution of the system is F, the actual length of the measured radargram is $1/F$. Here, the radargram is repeated 12 times to virtually extend the field of view presented to the back-projection algorithm.

be relevant for distributed sensing systems in which emitters and detectors are placed far away from the light source. In the case of an MLLD, the maximum fiber length is typically in the range of a few dozen meters. In the case of a fiber laser, it is naturally in the range of a few meters. However, fiber lasers oftentimes have the option of pre-chirping the pulse at their output in order to extend this range. THz-CCS system have an inherent advantage in such applications because they do not require any pulse compression.

3.2.4 Monolithic integration

The degree of integration of photonic terahertz systems is still lagging way behind electronic systems due to the technological heterogeneity of the required components. Even though the only two components actually operating at terahertz frequencies, i.e. the emitter and detector, are fabricated on a semiconductor process, the rest of the system lacks monolithic integration. While MLLDs, MMLDs, and SLDs are suitable monolithic light sources, all three in principle still require an ODU, which cannot be easily realized in an integrated circuit. However, the long coherence length and tunability of MLLDs promise to allow the adaptation of the ASOPS or ECOPS concept with UHRR-THz-TDS. While this removes the need for an ODU, there is currently no monolithic replacement for the aforementioned section of single-mode fiber for pulse compression. On the other hand, MMLDs and SLDs do not require pulse compression but are not suitable for ASOPS or ECOPS.

	THz-TDS (e.g. fiber laser)	UHRR-THz-TDS (MLLD)	THz-CCS (MMLD)	THz-CCS (SLD)
Spectroscopy	+ Bandwidth + Spectral resolution	○ Bandwidth – Spectral resolution	○ Bandwidth – Spectral resolution	+ Spectral resolution ○ Bandwidth
SAR imaging	+ Range resolution + Dynamic range + Unambiguous range ○ Field of view	+ Field of view ○ Range resolution ○ Dynamic range – Unambiguous range	○ Range resolution ○ Field of view – Dynamic range – Unambiguous range	+ Unambiguous range ○ Range resolution – Dynamic range – Field of view
Distributed sensing systems	– Pulse compression required (short fiber)	○ Pulse compression required (long fiber)	+ No pulse compression required	+ No pulse compression required
Monolithic integration	– Light source – Pulse compressor – ODU	+ Light source – Pulse compressor – ODU	+ Light source + No pulse compression required – ODU	+ Light source + No pulse compression required – ODU

Table 3.2: Practical implications of the spectral, coherence, and physical properties of the four different light sources.

CHAPTER

FOUR

SPECTRAL SHAPING

As seen in Chapter 2, the detected terahertz spectrum in an UHRR-THz-TDS system depends on the optical spectrum of the MLLD and the transfer function of the terahertz system. The latter is determined by the frequency response of the terahertz emitter and detector as well as the RF channel between the two. As discussed in Chapter 1, the optimization of the frequency responses of the emitter and the detector is subject to active technological work on the semiconductor structures. The primary objectives are increasing the bandwidth and the dynamic range.

In this chapter, it is shown how the remaining contributor, namely the optical spectrum, can be purposefully modified to shape the detected terahertz spectrum. Such spectral shaping can have most diverse goals, for example

- maximizing the detectable bandwidth,
- maximizing the spectral amplitudes within a given bandwidth,
- maximizing the amplitudes of particular spectral components, or
- suppressing particular spectral components.

There are in principle three ways to modify the optical spectrum:

- **Technologically modifying the spectrum emitted by the MLLD:** This approach leads to the most compact and lowest-cost system, but it is technologically challenging and does not allow the spectrum to be changed subsequently.
- **Filtering the optical spectrum with a static optical filter:** This approach is technologically simple, but it only allows a limited set of spectral shapes and does not allow the spectrum to be changed subsequently.
- **Filtering the optical spectrum with a programmable optical filter:** This approach is technologically simple and allows the generation of virtually arbitrary spectral shapes that can be changed at any time, but it introduces a bulky and expensive instrument into the system.

In the following, a general approach for spectral shaping and a few numerical examples are presented. Subsequently, first experimental results are shown and practical limitations are discussed.

4.1 Concept and numerical results

Consider the schematic sketched in Figure 4.1. Assuming that the complex optical spectrum of the MLLD and the transfer function of the terahertz system are known, Equation (2.15) can be used to analyze the spectral amplitudes of the intensity autocorrelation and Equation (2.16) to analyze the spectral amplitudes of the detected terahertz spectrum. Vice versa, if the goal is to generate a terahertz spectrum with particular spectral amplitudes and if the transfer function of the terahertz system is known, we can invert Equation (2.16) to synthesize the required spectral amplitudes of the intensity autocorrelation. However, the required complex optical spectrum cannot directly be synthesized because Equation (2.15) is not analytically invertible. One solution is using numerical methods to find a complex optical spectrum that approximates the desired autocorrelation spectral amplitudes. Here a genetic algorithm is used for that purpose [9].

[9] This approach has been investigated under my supervision as part of the master project entitled "Optimization and realization of optical spectra for terahertz time-domain spectroscopy using genetic algorithms" by M. Sc. Muhamed Dedic and M. Sc. Peter Krämer. I have published a summary of their work in Ref. [10].

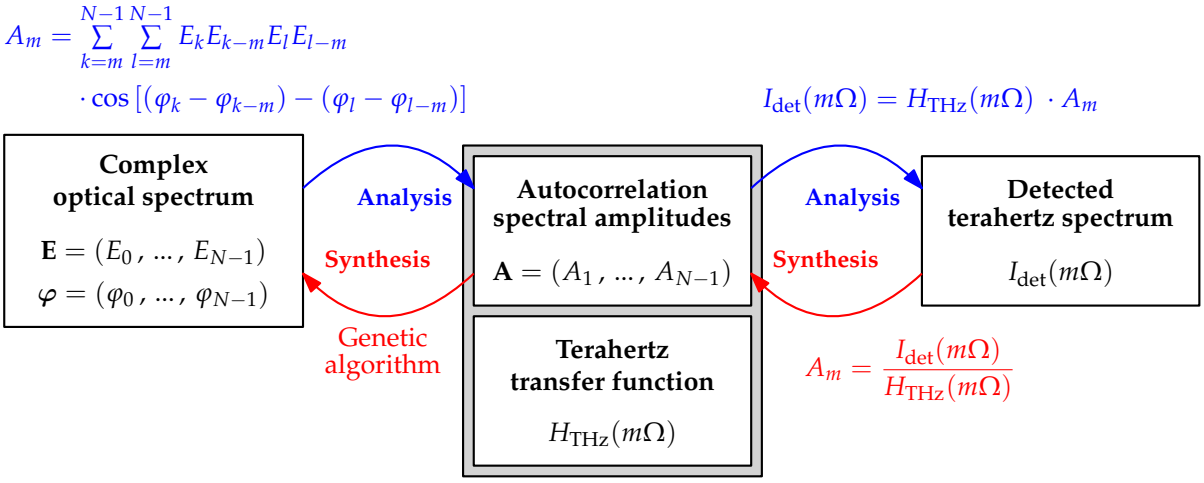

Figure 4.1: Concept for spectral shaping.

The genetic algorithm aims to minimize the value of a scalar fitness function ξ. In our case, the independent variables of the genetic algorithm are the optical amplitudes $\mathbf{E} = (E_0, E_1, \ldots, E_{N-1})$ and phases $\boldsymbol{\varphi} = (\varphi_0, \varphi_1, \ldots, \varphi_{N-1})$. Since the goal is to synthesize desired autocorrelation spectral amplitudes $\mathbf{A} = (A_1, A_2, \ldots, A_{N-1})$, we can intuitively define a suitable fitness function $\xi(\mathbf{A})$. The relationship between the independent variables $\mathbf{E}$ and $\boldsymbol{\varphi}$ and the spectral amplitudes $\mathbf{A}$ is in turn defined by Equation (2.15), which can be efficiently implemented in the genetic algorithm to obliquely reformulate the fitness function $\xi(\mathbf{A}) = f\big(\mathbf{A}(\mathbf{E}, \boldsymbol{\varphi})\big)$.

In this section, the optimization problem is simplified by fixing the optical phases $\boldsymbol{\varphi} = \mathbf{0}$ and only varying the optical amplitudes $\mathbf{E}$. There is good practical justification for this besides the reduced computational effort. Firstly, the maximum autocorrelation spectral amplitudes result in the case of a linear (or constant) optical phase due to constructive interference between the beat tones. Thus, the only justification for deviating from a linear optical phase is the potential to suppress particular autocorrelation spectral amplitudes through well-controlled destructive interference. This would, however, inevitably be at the cost of the other spectral amplitudes. There is no conceivable application in which that would be beneficial. Secondly, the relationship between the optical phases and the fitness function is highly volatile, causing the genetic algorithm to converge much slower than if only the optical amplitudes are considered. Thirdly, experiments have shown that if the optical phases are considered in

the optimization procedure, even the slightest deviation in the realized optical phases causes the measured spectrum to deviate vastly from its designed shape.

An important aspect in the use of the genetic algorithm is the bounding and normalization of the variables $\mathbf{E}$. Practically, the lower and upper bounds are defined by the lowest and highest amplitudes that can be achieved by filtering and amplification. For the sake of simplicity, the lower and upper bounds are set to zero and infinity, respectively. The normalization is required to get meaningful and comparable optimization results. To that end, the genetic algorithm calculates the spectral amplitudes $\mathbf{A}$ within the fitness function as functions of the normalized spectral amplitudes $\mathbf{E}/\left|\mathbf{E}\right|$. This normalization can be physically interpreted as a constant average optical power.

In the following, a few noteworthy numerical results for the spectral shaping approach is presented. To simplify the interpretation and keep the results generally applicable, the transfer function of the terahertz system is neglected and the optimization goals are defined in terms of the autocorrelation spectral amplitudes $\mathbf{A}$ considering $N = 100$ laser modes. The genetic algorithm is supplied by the *Optimization Toolbox* in *MATLAB R2021A*.

4.1.1 Maximizing the total power

The first optimization goal has the objective of maximizing the total "power" of the intensity autocorrelation, i.e. maximizing $\left|\mathbf{A}\right|^2$. To convert this into a minimization problem, the fitness function

$$\xi_{\text{max. power}}(\mathbf{A}) = \left|\mathbf{A}\right|^{-2} \tag{4.1}$$

is defined. This optimization goal can be interpreted as maximizing the *optical-to-detected power efficiency*. The resulting spectra are shown as red curves in Figure 4.2. Plot (a) shows the optical amplitude spectrum and plot (b) shows the resulting autocorrelation spectrum. For reference, the blue curves depict the spectra for a uniform optical spectrum with the same average optical power.

This optimization has yielded an increase in total power of $\left|\mathbf{A}_{\text{max. power}}\right|^2 / \left|\mathbf{A}_{\text{uniform}}\right|^2 = 1.166$. It can be seen that the optimization procedure has symmetrically favored the spectral components in the middle of the optical spectrum at the cost of the spectral components at the outer edges. This can be explained by the fact that these appear

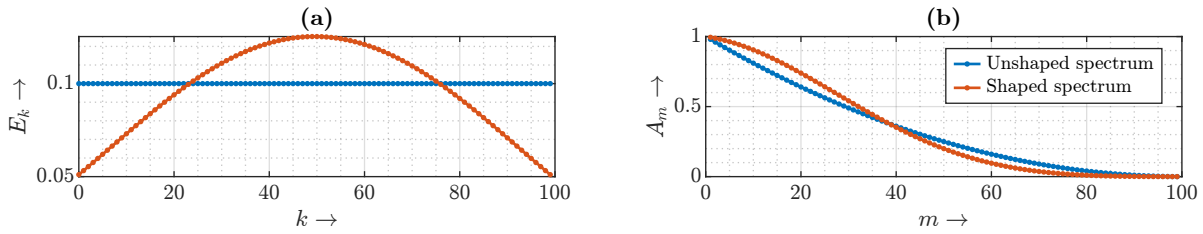

Figure 4.2: Optimization results for optimizing the total power of the intensity autocorrelation for the case of $N = 100$ laser modes. The red curve shows the optimized spectra, whereas the blue curve shows the spectra for a uniform optical spectrum for reference. **(a)** Optical amplitude spectrum $\mathbf{E}$. **(b)** Autocorrelation spectrum $\mathbf{A}$. The optical spectra are normalized so that $|\mathbf{E}| = 1$.

most frequently in the calculation of $\mathbf{A}$. As will be discussed later in this chapter, this optical spectrum can be realized comparatively easily, as its maximum is located in the middle and the ratio of the highest to the lowest mode is relatively small.

4.1.2 Maximizing the bandwidth

An optimization goal that has high practical value is the maximization of the bandwidth. There are different ways to mathematically define this goal. A particularly promising fitness function is

$$\xi_{\text{max. bandwidth}}(\mathbf{A}) = \frac{1}{\min\left\{{A_m}^2\right\}} \,. \tag{4.2}$$

With this fitness function, the genetic algorithm strives to maximize the squared magnitude of the weakest spectral component. For each individual within each generation, it identifies the spectral component with the smallest amplitude, and favors those individuals for which it is the highest. Over time, this has the effect of equalizing the spectrum by iteratively "pulling up" one spectral component after the other. The resulting spectra are depicted in Figure 4.3. Plot (b) shows that this approach generated an autocorrelation spectrum that is virtually flat for $m > 40$. This comes at the cost of the spectral components $m < 79$, but achieves a significant gain for $m > 79$. Plot (a) nicely visualizes how this is achieved. Since the highest spectral components of the autocorrelation result from the beating of the outermost components of the optical spectrum, these are enhanced to achieve the desired optimization goal. This leads to a "bathtub

shape“ of the optical spectrum. While attractive, we will later see that this approach is hard to realize and in practice leads to smaller gains than in theory.

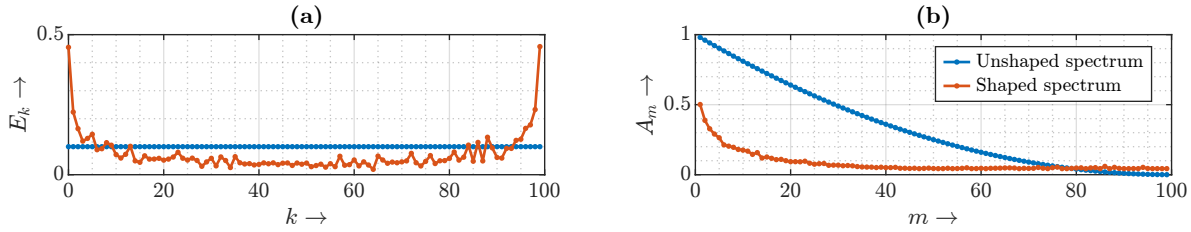

Figure 4.3: Optimization results for optimizing the bandwidth of the intensity autocorrelation for the case of $N = 100$ laser modes. The red curve shows the optimized spectra, whereas the blue curve shows the spectra for a uniform optical spectrum for reference. **(a)** Optical amplitude spectrum $\mathbf{E}$. **(b)** Autocorrelation spectrum $\mathbf{A}$. The optical spectra are normalized so that $|\mathbf{E}| = 1$.

4.1.3 Maximizing a particular spectral component

A straightforward optimization goal is the maximization of a particular spectral component $m = m_0$. It requires the simple fitness function

$$\xi_{\text{max. } m_0}(\mathbf{A}) = \frac{1}{{A_{m=m_0}}^2} \,. \tag{4.3}$$

Despite the simplicity of the fitness function, the interpretation of the results is quite involved because the resulting spectra strongly depend on the choice of m_0. Three distinct cases can be identified:

(a) $m_0 = 1$

The result for the case $m_0 = 1$ is depicted in Figure 4.4. The magnitude A_1 approaches 1, which means a small gain of $A_{1,\text{optim.}}/A_{1,\text{uniform}} = 1.0193$ compared to the uniform spectrum.

(b) $1 < m_0 < N/2$

The case $1 < m_0 < N/2$ is most complicated because it generates complex spectral shapes that are difficult to interpret. Examples of resulting spectra for four different

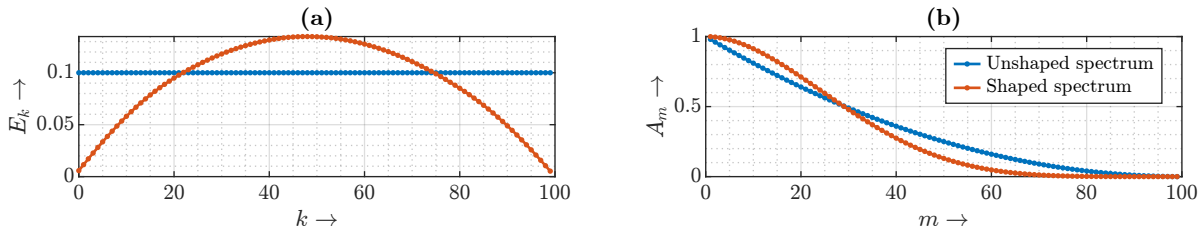

Figure 4.4: Optimization results for maximizing the spectral component $m = m_0 = 1$ for the case of $N = 100$ laser modes. The red curve shows the optimized spectra, whereas the blue curve shows the spectra for a uniform optical spectrum for reference. **(a)** Optical amplitude spectrum $\mathbf{E}$. **(b)** Autocorrelation spectrum $\mathbf{A}$. The optical spectra are normalized so that $|\mathbf{E}| = 1$.

choices of m_0 are depicted in Figure 4.5. While no simple rule can be extracted from these results, there appears to be a periodicity with the period m_0 in the optical spectra. The autocorrelation spectral amplitudes exhibit peaks around integer multiples of m_0. The width of these peaks decreases with increasing value of m_0.

(c) $N/2 \leq m_0$

The analysis of the case $N/2 \leq m_0$ gives quite conclusive and useful results. Examples of resulting spectra for four different choices of m_0 are depicted in Figure 4.6. For $m_0 = N/2$, the genetic algorithm produces a uniform optical spectrum

$$E_{k,\,\text{optim.},\,m_0=N/2} = N^{-1/2}\,,\; 0 \leq k \leq N-1\,. \tag{4.4}$$

For $m_0 = N-1$, the genetic algorithm produces an optical spectrum consisting of only the outer two modes

$$E_{k,\,\text{optim.},\,m_0=N-1} = \begin{cases} 2^{-1/2} & ,\quad k \in \{0\,,\,N-1\} \\ 0 & ,\quad \text{else} \end{cases}\,. \tag{4.5}$$

For $N/2 < m_0 < N-1$, the genetic algorithm produces optical spectra that consist of two blocks with roughly uniform amplitudes and a $2 \cdot m_0 - N$ wide gap in between. The existence of this gap is easy to explain by the fact that there are no laser modes located m_0 away from the modes within the gap. Thus, they cannot contribute to A_{m_0} and it is best so set their amplitudes to 0. Comparing the result for $N/2 < m_0 < N-1$ with the results for $m_0 \in \{N/2\,,\,N-1\}$, it is reasonable to assume that the optimum

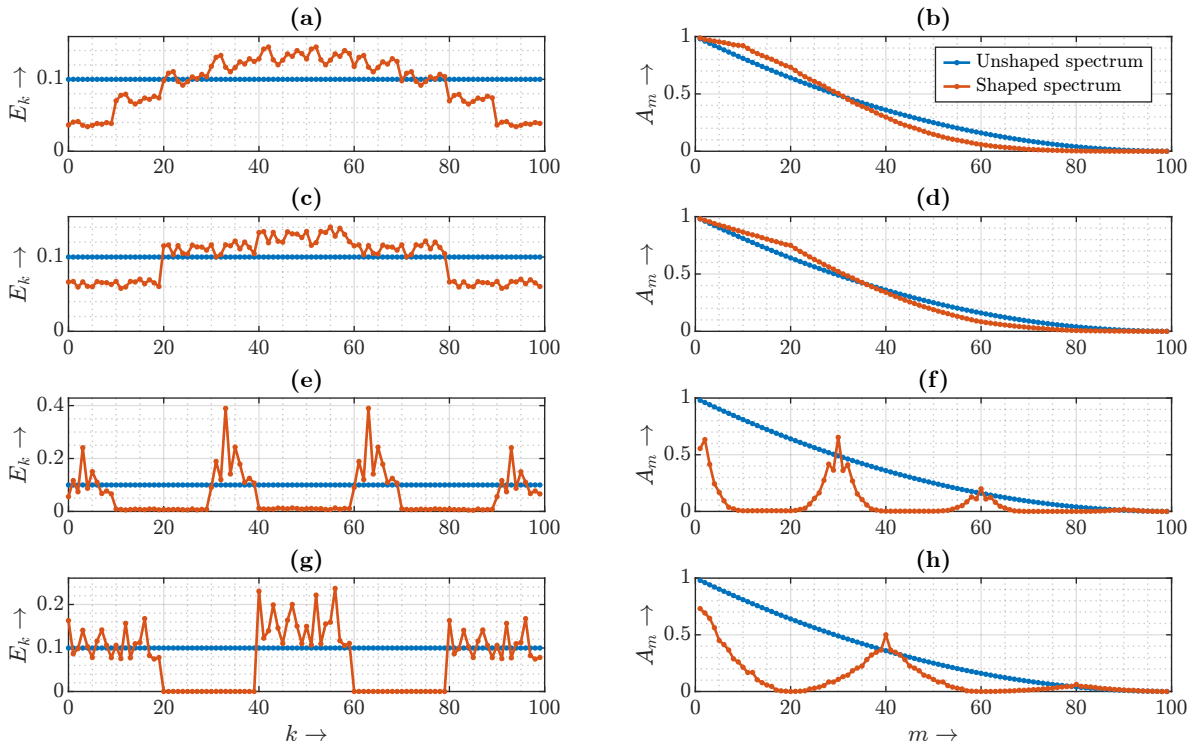

Figure 4.5: Example optimization results for maximizing spectral components $0 < m = m_0 < N/2$ for the case of $N = 100$ laser modes. The red curve shows the optimized spectra, whereas the blue curve shows the spectra for a uniform optical spectrum for reference. **(a,c,e,g)** Optical amplitude spectrum **E**. **(b,d,f,h)** Autocorrelation spectrum **A**. **(a,b)** $m_0 = 10$, **(c,d)** $m_0 = 20$, **(e,f)** $m_0 = 30$, **(g,h)** $m_0 = 40$. The optical spectra are normalized so that $|\mathbf{E}| = 1$.

solution results when the roughly uniform amplitudes are replaced with perfectly uniform amplitudes. The corresponding spectra are shown in yellow in Figure 4.6.

Upon closer inspection, it can be seen that these "guessed" spectra lead to a marginally higher amplitude A_{m_0} than the result of the genetic algorithm. The presumably optimum solution for the case $N/2 \leq m_0$ can be summarized as

$$E_{k,\,\text{optim.},\,m_0 \geq N/2} = \begin{cases} 0 & , \quad N - m_0 \leq k < m_0 \\ [2 \cdot (N - m_0)]^{-1/2} & , \quad \text{else} \end{cases} \tag{4.6}$$

with the resulting amplitude

$$A_{m_0,\,\text{optim.}}\big|_{m_0 \geq N/2} = 0.25\,. \tag{4.7}$$

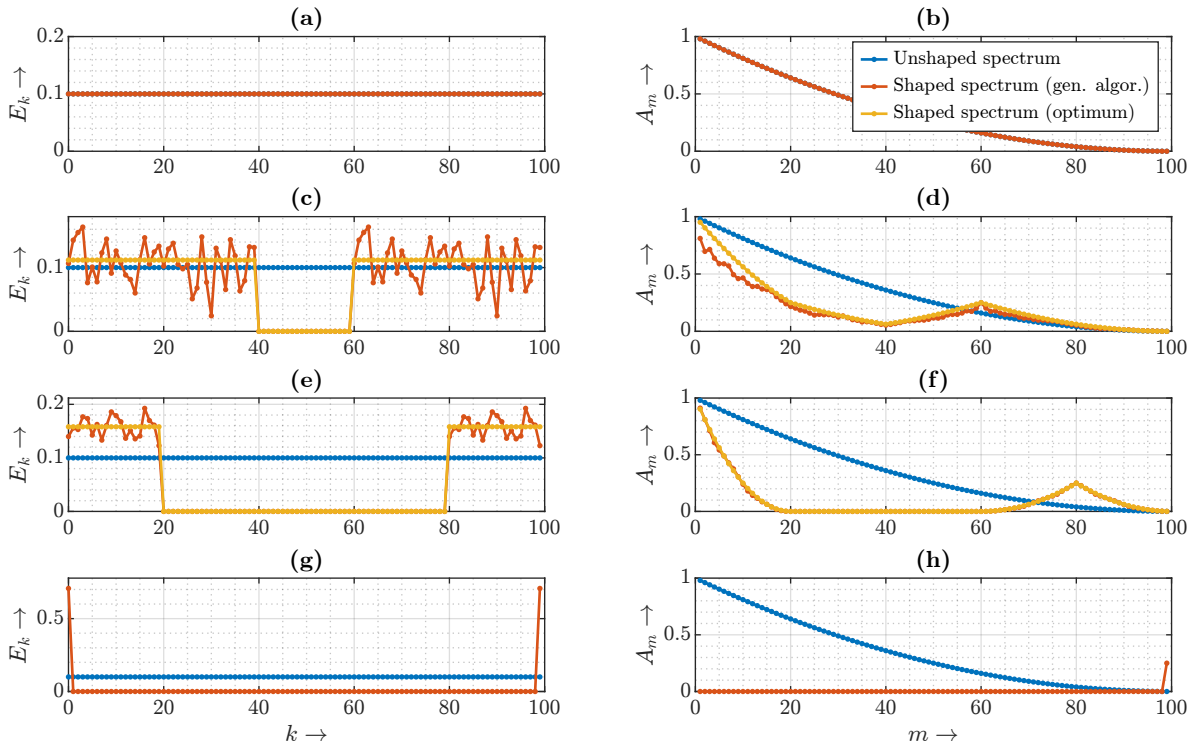

Figure 4.6: Example optimization results for maximizing spectral components $0 < m = m_0 < N/2$ for the case of $N = 100$ laser modes. The red curve shows the optimized spectra, whereas the blue curve shows the spectra for a uniform optical spectrum for reference. The yellow curve represents the presumably optimum solution according to Equation (4.6). **(a,c,e,g)** Optical amplitude spectrum $\mathbf{E}$. **(b,d,f,h)** Autocorrelation spectrum $\mathbf{A}$. **(a,b)** $m_0 = 50$, **(c,d)** $m_0 = 60$, **(e,f)** $m_0 = 80$, **(g,h)** $m_0 = 99$. The optical spectra are normalized so that $|\mathbf{E}| = 1$.

4.2 First experimental results

4.2.1 Spectral shaping testbed

In Ref. [10], I have presented a testbed to experimentally test the viability of spectral shaping for UHRR-THz-TDS and shown first experimental results. A block diagram of the testbed is depicted in Figure 4.7.

The centerpiece of the testbed is the combination of a *Finisar Waveshaper 1000A* programmable optical filter and a *Thorlabs EDFA100P* Erbium-doped fiber amplifier (EDFA). The polarization-maintaining Waveshaper can generate user-defined filter functions that are arbitrary both in magnitude and phase with a frequency resolution of 10 GHz

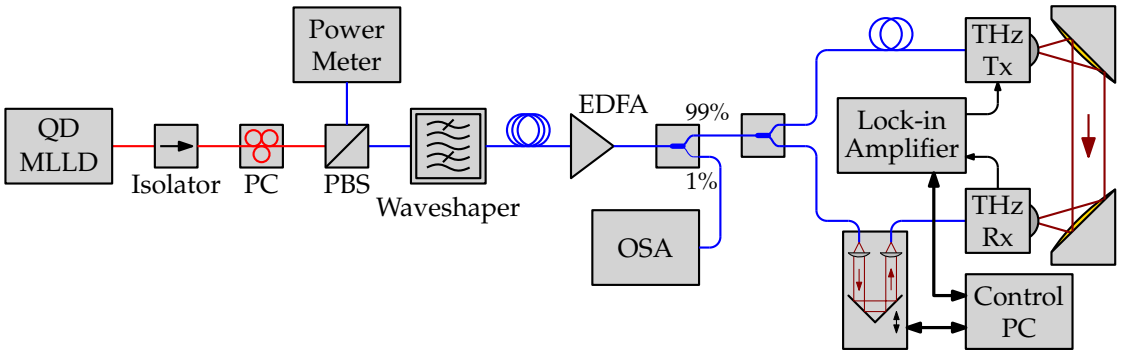

Figure 4.7: Block diagram of the spectral shaping testbed. Red lines indicate single-mode fibers, blue lines indicate polarization-maintaining fibers, and black lines indicate electrical connections.

across the frequency range from 191.25 to 196.275 THz. Because the filter is passive, it is followed by an EDFA to re-amplify the optical signal and ensure that its average power is constant independent of the chosen filter shape.

The light source for the testbed is the same two-section QD MLLD from Fraunhofer HHI with an FSR of about 50.14 GHz as used in Section 2.3. Because the FSR of the MLLD is higher than the frequency resolution of the Waveshaper, each laser mode can be independently adjusted both in amplitude and phase. The output signal of the MLLD first passes through an isolator to avoid back-reflections into the MLLD. The combination of a polarization controller (PC) and polarization beam splitter (PBS) is used to launch the light into the slow-axis of the PM fiber that is connected to the input of the Waveshaper. The PC is adjusted until the power at the orthogonal output of the PBS is minimized.

The pulse chirp is roughly compensated with a 50 m long section of PM fiber. The chirp compensation is then fine-tuned with the phase of the Waveshaper. A fraction of the signal at the output of the EDFA is split off and fed into an optical spectrum analyzer (OSA) to verify the generated amplitude spectrum. The majority of the optical signal is fed into a conventional terahertz spectrometer using a photodiode-based emitter module (THz Tx) and a photoconductive detector module (THz Rx), both from Fraunhofer HHI. The ODU is an *OZ Optics ODL-650* with a delay range of 330 ps. The data acquisition is performed with a *Zurich Instruments MFLI* lock-in amplifier. The lock-in detection is enabled by modulating the bias voltage of the terahertz emitter. The

RF path between emitter and detector is a simple collimated transmission geometry consisting of two off-axis parabolic mirrors.

This testbed allows the generation of a large variety of spectral shapes while allowing a fair comparison between the results by keeping the average optical power at the emitter and detector constant with the help of the EDFA. To demonstrate the viability of the spectral shaping approach and motivate further investigations, a particularly interesting spectral shape that I have first published in Ref. [10] is shown here.

4.2.2 Maximizing the bandwidth

The optimization goal is based on the maximization of the bandwidth described in the previous section. However, because we know that the bandwidth of our terahertz system is limited by the emitter and detector to about 1.3 THz, only the first 1.3 THz / 50.14 GHz $\approx$ 25 spectral components of the intensity autocorrelation are considered. This results in the fitness function

$$\xi_{\text{max. bandwidth}}(\mathbf{A}) = \frac{1}{\min\left\{{A_m}^2\right\}}\,,\ 1 \leq m \leq 25\,. \tag{4.8}$$

The measured spectra are depicted in Figure 4.8. Plot (a) shows the optical spectra and plot (b) shows the terahertz spectra. The fat blue lines indicate the unshaped spectra using the natural optical spectrum of the MLLD. The fat red lines indicate the spectra resulting after shaping with the Waveshaper. The thin lines highlight the maxima of the spectra peaks.

The measured terahertz spectra in plot (b) show that by spectral shaping the spectral components between 1 and 1.5 THz are enhanced by up to 8 dB. This is a quite remarkable improvement of the system's performance. However, it comes at the cost of the spectral components between 100 GHz and 1 THz. The optical spectra in plot (a) reveal how this change of the terahertz spectrum is achieved. The spectral shaping has generated an optical spectrum consisting of two hills with a valley in between. The distance between the crests of the hills is about $25 \cdot 50.14\,\text{GHz} \approx 1.25\,\text{THz}$. The highest spectral components of the terahertz spectrum result solely from the beating of the amplified laser modes within the two hills. The attenuated modes within the valley only contribute to the lower spectral components. By comparison with the theoretical case

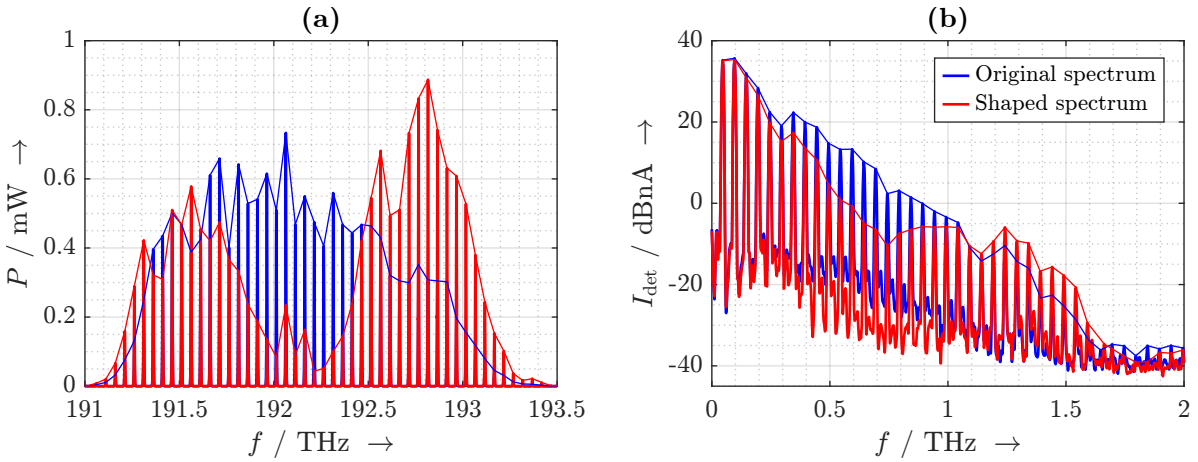

Figure 4.8: **(a)** Measured optical spectra of the MLLD without (blue) and with (red) spectral shaping. **(b)** Measured terahertz spectra without (blue) and with (red) spectral shaping.

depicted in Figure 4.3, it is evident that the distance between the crests of the hills is always determined by the highest spectral component that is considered in the fitness function.

4.3 Practical limitations

There are a few practical limitations to the spectral shaping concept that shall be briefly discussed here. This discussion is focused on the programmable optical filter approach. The limitations originate from the transfer function of the terahertz system, the programmable optical filter, the optical amplifier, and the spectrum of the MLLD.

4.3.1 Terahertz system

Due to the frequency response of the terahertz emitter and detector, the terahertz system exhibits a low-pass behavior. Considering Figure 2.6 (b), a 45 dB drop-off across a 1.3 THz bandwidth can be observed. This naturally puts high frequencies at a disadvantage over low frequencies. If the goal is to flatten the spectrum, the autocorrelation spectral amplitudes A_m would have to cancel this effect. However, as we have seen, the amplitudes A_m naturally drop off towards higher frequencies, too. Furthermore, the transfer function of the terahertz system can exhibit distinct nulls, for example

due to water absorption. Spectral components that fall within these absorption lines are nearly impossible to recover. Moreover, by considering the theoretical results for maximizing the bandwidth depicted in Figure 4.3, it is evident that a net gain is only achieved if the spectral components of the intensity autocorrelation that are enhanced do not experience excessive attenuation by the terahertz system.

4.3.2 Programmable optical filter and amplifier

The programmable optical filter is a passive device, that is to say it can only attenuate spectral components. The amplification of a spectral component requires an optical amplifier, as described in the previous section. However, the gain of the optical amplifier – in the case shown here an EDFA – is limited, typically between 20 and 30 dB. Consequentially, laser modes can only be amplified by a limited factor. Moreover, the attenuation that can be generated by the programmable optical filter is limited. In the case of the Waveshaper, it can be set between 0 and 30 dB. Furthermore, there are slight inaccuracies and interrelationships in the combined magnitude and phase functions of Waveshaper and EDFA.

4.3.3 Mode-locked laser diode

The spectrum of an MLLD typically exhibits an inverse U-shape, i.e. there is a natural drop-off towards the outer edges of the spectrum. In combination with the limitations of the programmable optical filter and the amplifier, this puts a lower and an upper bound on the amplitudes E_k that can be practically realized. The lower and upper bounds of the magnitude of a particular mode $k = k_0$ depend not only on the index k_0 but also on the chosen magnitudes for the other modes $E_{k \neq k_0}$.

In summary, while the spectral shaping concept proposed here allows severe and useful modifications of the detected terahertz spectrum, the limitations of the components as well as the terahertz generation and detection process itself restrict the spectral shapes that can be practically realized. The amplitudes of the highest spectral components are particularly limited. Ideally, all involved devices are well-characterized and their behavior considered in the determination of the filter coefficients. Furthermore, it may be viable to iteratively measure the terahertz spectrum and adjust the filter coefficients to approach the desired spectral shape.

CHAPTER

FIVE

INTERFEROMETRIC RECONSTRUCTION OF THE DELAY AXIS

One of the most critical components of an UHRR-THz-TDS system is the ODU. It is used to sample the received terahertz signal with a delayed version of the optical signal that has generated the transmitted terahertz signal. The accuracy of the delay that is introduced by the ODU is of utmost importance for the performance and accuracy of the system. In the previous chapters, we have assumed that the ODU delays the optical signal with a well-known and linearly increasing delay τ. However, in reality this assumption is not accurate. Generally, it is more accurate to state that the ODU introduces a delay $\tau(t)$ at the observation time t. The detected photocurrent at the time t thus becomes $i_{\text{det}}\big(\tau(t)\big)$. For the purposes of this discussion, it is assumed that the delay changes much slower with time than the infrared and terahertz signals.

5.1 State of the art and problem formulation

Conventionally, the ODU is a free-space optical device that is constructed as illustrated in Figure 2.1. The light at the input fiber is collimated into free space, reflected from a mirror (typically a hollow-roof prism), and focused into the output fiber. The mirror is mounted on a motorized translation stage, so that the length of the free-space path

– and thus the introduced delay – can be adjusted. Because the accuracy of the delay depends on the positioning accuracy of the mirror, typically great effort is spent on the mechanical quality of the device. This makes an accurate ODU quite bulky, heavy, expensive, and mechanically sensitive.

In a conventional THz-TDS system, the delay range of the ODU is usually in the order of a few hundred picoseconds. Thus, the device is typically several centimeters to a few decimeters long. It is important to note that for UHRR-THz-TDS the ODU can be much shorter than that. Because identical infrared and terahertz pulses arrive at the terahertz detector with the repetition rate of the MLLD, each pulse contains the full spectral information and thus – theoretically – a delay range of $1/F$ is sufficient.

The ODU can generally be operated in three different modes:

- **Stepped mode:** The mirror is moved in incremental steps and the detected photocurrent is measured in the times between the steps whenever the mirror is stationary. This mode generally has a high positioning accuracy and requires hardly any time synchronization between the ODU and the data acquisition. However, it is very slow and energetically inefficient due to the frequent acceleration and deceleration of the mirror.
- **Point-to-point continuous mode:** The mirror is moved continuously between two positions, for example its two end stops. This mode can be much faster than the stepped mode, but it requires accurate time synchronization between the movement of the ODU and the data acquisition. Moreover, during the acceleration and deceleration times at the ends of the delay range, the relationship between the measurement time and the delay is inevitably non-linear.
- **Harmonic mode:** If the mirror is driven by a voice-coil motor, it can be viable to drive it with a harmonic signal, such that the delay changes sinusoidally with time. This mode can be particularly fast and energy efficient, but it requires a technique to compensate the non-linear relationship between measurement time and delay. The harmonic mode is particularly interesting for UHRR-THz-TDS because the comparatively short stroke of voice-coil motors matches the ultra-high repetition rate.

We set aside the harmonic mode for a moment and first consider only the stepped and point-to-point continuous modes. In both cases, the delay can show both systematic and random deviations from its ideal linear characteristic. These are generally due to mechanical inaccuracies or external influences. A common cause of delay fluctuations are, for example, the threads of the lead screw that translates the rotation of the motor inside the ODU into a translation. The influences of these errors in conventional THz-TDS have been subject to extensive research [112–115]. Using system-theoretical models as well as numerical simulations and measurements, it has been found that these errors reduce the signal amplitude, increase the apparent noise floor, and reduce the spectral bandwidth. In the case of the point-to-point continuous mode, an additional source of error can be the synchronization between the movement of the ODU and the data acquisition. In the simplest case, a random delay between the start of the movement of the ODU and the sampling of the detected photocurrent causes a random delay offset between measurements. Since this offset cannot be differentiated from the delay introduced by the RF channel, it puts a direct limit on the time resolution of the system. It is thus necessary to either *eliminate* these errors by improving the ODU or *correct* them with a suitable reference signal.

In 2017, Molter et al. [114] demonstrated a promising concept for correcting the delay axis in a THz-TDS system by using a continuous-wave laser and a Mach-Zehnder interferometer to generate a reference signal. A block diagram of their concept is sketched in Figure 5.1.

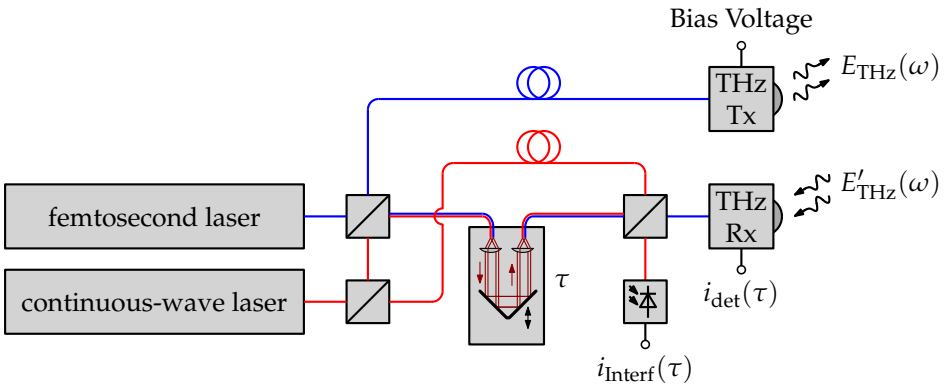

Figure 5.1: Block diagram of the interferometric concept for the reconstruction of the delay axis demonstrated by Molter et al. [114].

The setup is conceptually a conventional time-domain spectrometer driven by a femtosecond laser. In addition to the femtosecond laser, the light from a continuous-wave laser is polarization-multiplexed through the ODU with a pair of polarization beam splitters. Behind the ODU, the de-multiplexed delayed light from the continuous-wave laser is combined with a non-delayed version of itself and detected in a photodiode. By splitting the optical signal from the continuous-wave laser in front of the ODU and combining it again behind the ODU, a Mach-Zehnder inferometer is formed. The photocurrent generated in the photodiode is of the form

$$i_{\mathrm{Interf}}(\tau) \mathrel{\widetilde{\propto}} 1 + \cos(2\pi \cdot f_{\mathrm{cw}} \cdot \tau) \,, \tag{5.1}$$

where f_{cw} is the frequency of the continuous-wave laser. In Ref. [114] a HeNe laser with $f_{\mathrm{cw}} \approx 474\,\mathrm{THz}$ was used. Thus, the interferogram measured by the photodiode shows one minimum and maximum for every 2.1 fs change of the delay τ. By counting the extrema of the interferogram as the ODU is moved, the delay axis can be easily reconstructed with femtosecond accuracy. This approach has proven to generate a highly accurate delay axis without imposing demanding requirements on the ODU. In fact, this approach allows the use of a very simple and inaccurate ODU without any performance penalty. However, because the interferogram is perfectly periodic with the frequency of the continuous-wave laser, only relative information about the delay axis can be retrieved. It is not possible to use this interferogram for absolute synchronization, that is to say for eliminating a delay offset.

The interferometric concept can be adopted in a particularly elegant, simple, and useful way to UHRR-THz-TDS in a novel approach that I have first published in Ref. [3]. By using the optical signal from the MLLD in an interferometer, this new approach allows both absolute time synchronization and correction of the delay axis with minimal hardware effort. In the following, first the concept is introduced, the setup is explained, and a mathematical expression for the resulting interferogram is derived. Subsequently, the use of this concept for time synchronization is demonstrated, and it is shown how it can facilitate the efficient and accurate processing of measurement data. Finally, an outlook to using this concept for complete correction of the delay axis is given and some of the unique opportunities offered by its use are highlighted.

5.2 System setup and derivation of the interferogram

A block diagram of the concept is depicted in Figure 5.2. The setup consisting of the MLLD, chirp compensation, coupler 1, ODU, terahertz emitter, and terahertz detector resembles a conventional UHRR-THz-TDS system. The only addition is the part highlighted in gray consisting of couplers 2 through 4 and a pair of photodiodes.

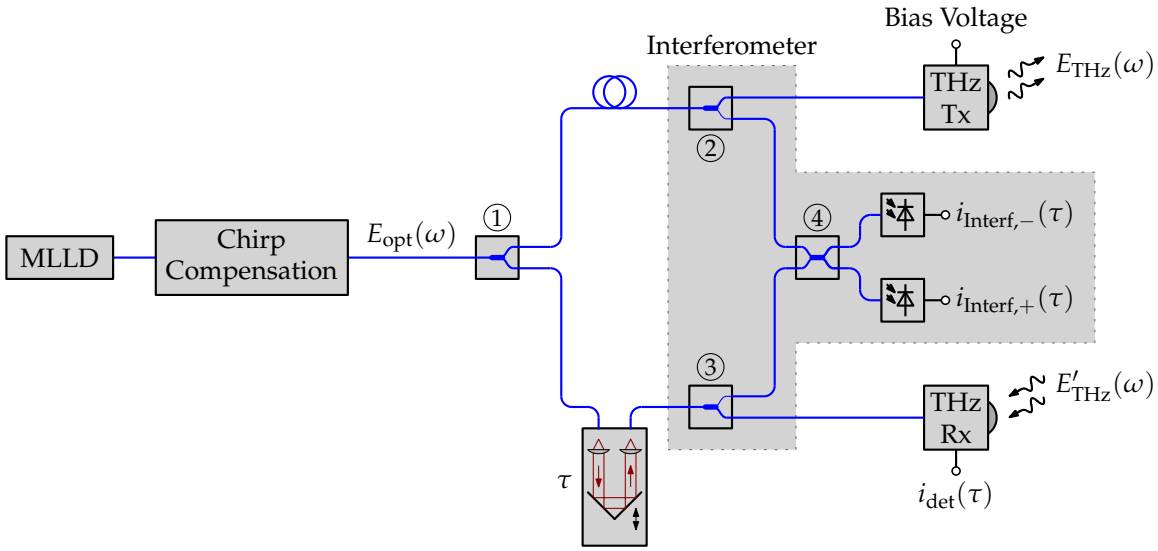

Figure 5.2: Block diagram of the novel interferometric concept for the reconstruction of the delay axis in UHRR-THz-TDS.

Couplers 2 and 3 split off a part of the optical signal going to the emitter and detector, respectively. These signals are then combined in coupler 4, and the combined signals are detected by a balanced pair of photodiodes. The four couplers in the system effectively form a Mach-Zehnder interferometer. If we assume the optical spectrum of the MLLD given in Equation (2.1), it can be shown that the resulting photocurrents are [3]

$$i_{\mathrm{Interf},-}(\tau) \propto \sum_{k=0}^{N-1} {E_k}^2 \cdot \{1 - \cos\left[2\pi \cdot (f_0 + kF) \cdot \tau\right]\} \tag{5.2}$$

and

$$i_{\mathrm{Interf},+}(\tau) \propto \sum_{k=0}^{N-1} {E_k}^2 \cdot \{1 + \cos\left[2\pi \cdot (f_0 + kF) \cdot \tau\right]\} \ . \tag{5.3}$$

The difference of these two photocurrents is then [3]

$$i_{\text{Interf}}(\tau) = i_{\text{Interf},+}(\tau) - i_{\text{Interf},-}(\tau) \propto \sum_{k=0}^{N-1} {E_k}^2 \cdot \cos\left[2\pi \cdot (f_0 + kF) \cdot \tau\right] \ . \tag{5.4}$$

This interferogram is simply the linear superposition of the individual interferograms of all laser modes. A calculated example is depicted in Figure 5.3. Plot (a) shows the normalized and discretized optical spectrum of the two-section MLLD used in Chapters 2 and 4. Plot (b) shows the corresponding interferogram. The interferogram consists of a carrier-frequency oscillation at approximately the frequency f_0 that is modulated by an envelope that is periodic with the repetition rate F of the MLLD. Incidentally, the Fourier transform of the interferogram is the power spectral density of the electric field emitted by the MLLD.

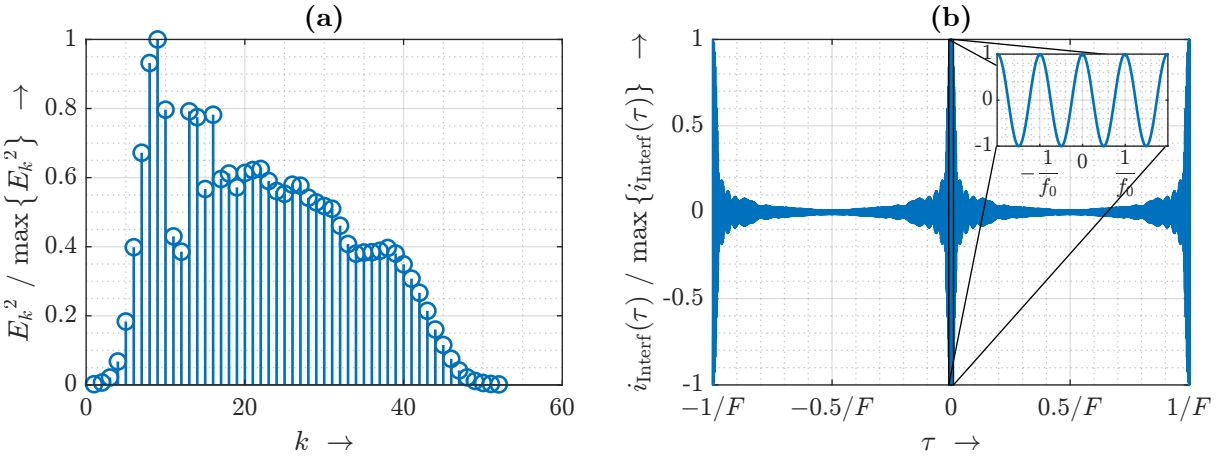

Figure 5.3: (a) Normalized and discretized optical spectrum of an MLLD. **(b)** Calculated interferogram for the optical spectrum in **(a)**.

The signal from the interferometer is obviously independent of the transfer function of the terahertz system. Its envelope exhibits the same periodicity as the detected terahertz photocurrent and serves as an accurate absolute time reference between measurements. This can, for example, be realized by defining the range between two maxima of the envelope as the range $0 \leq \tau \leq 1/F$. Doing so automatically establishes a stable time-relationship for the detected terahertz signal. At the same time, the internal oscillation of the interferometer signal can be used for accurate relative corrections of the delay axis.

5.3 Time synchronization and signal processing for UHRR-THz-TDS

The prerequisite for the proposed technique is that the signals from the terahertz detector and the interferometer are synchronously sampled with a sufficient sampling rate. The required sampling rate is determined by the bandwidth of the signal from the interferometer, which depends on the optical spectrum as well as the speed of the ODU $\mathrm{d}\tau(t)/\mathrm{d}t$. Assuming that the ODU stops at the outer ends of its range and moves with the maximum speed $\mathrm{d}\tau(t)/\mathrm{d}t|_{\max}$, the signal from the interferometer covers the frequency range

$$0 \;\leq\; f \;\leq\; [f_0 + (N-1)\cdot F]\cdot \left.\frac{\mathrm{d}\tau(t)}{\mathrm{d}t}\right|_{\max} . \tag{5.5}$$

If we assume a linear movement of the ODU and a scan rate of 1 Hz for the $2 \cdot 20$ ps scan range, the maximum frequency is approximately 7.8 kHz [10]. In the following paragraphs, first the synchronization algorithm using the signal from the interferometer is explained, and then a few experimental results using this concept for the thickness determination of thin dielectric layers together with the necessary signal processing steps are shown.

5.3.1 Synchronization algorithm

The time-discrete signals to be considered are the sampled photocurrents from the interferometer

$$i_{\mathrm{Interf}}[n] = i_{\mathrm{Interf}}(nT_{\mathrm{S}}) \;,\; n \in \mathbb{Z} \;, \tag{5.6}$$

and from the terahertz detector

$$i_{\mathrm{det}}[n] = i_{\mathrm{det}}(nT_{\mathrm{S}}) \;,\; n \in \mathbb{Z} \;, \tag{5.7}$$

where T_{S} is the sampling period. The first step of the synchronization algorithm is to determine the envelope of the interferometer signal and to find the locations n_1 and

[10] The bandwidth of the the interferogram is two orders of magnitude larger than that of the photocurrent from the terahertz detector. The use of the interferometer thus leads to a significant increase of the required sampling rate and storage capacity.

n_2 of two consecutive maxima of the envelope. Next, the signal from the terahertz detector is trimmed at the locations of the maxima to extract exactly one period

$$i_{\mathrm{det,sync}}[k] = i_{\mathrm{det}}[n_1 + k] \ , \ 0 \leq k < N_{\mathrm{S}} = n_2 - n_1 \ , \tag{5.8}$$

where N_{S} is the number of samples within one period. Finally, assuming a linear delay axis, we specify the delays

$$\tau[k] = \frac{k}{N_{\mathrm{S}}} \cdot \frac{1}{F} \ , \ 0 \leq k < N_{\mathrm{S}} \ . \tag{5.9}$$

Besides synchronizing the samples between measurements, this approach has the benefit that the trimmed signal $i_{\mathrm{det,sync}}[k]$ is exactly one period of the periodic detected photocurrent. Thus, the discrete terahertz spectrum

$$I_{\mathrm{det,sync}}[i] = I_{\mathrm{det,sync}}(iF) \ , \ 0 \leq i < N_{\mathrm{S}} \ , \tag{5.10}$$

can be precisely determined by discrete Fourier transform of $i_{\mathrm{det,sync}}[k]$. Notably, the accurate cropping of the signal alleviates the need for windowing in the time domain. Moreover, the frequency resolution of the sampled signal is exactly equal to the theoretical frequency resolution achievable with the MLLD.

5.3.2 Experimental results

To test the synchronization concept and to evaluate its accuracy, transmission-mode measurements of dielectric layers with well-known thicknesses were performed using the measurement setup sketched in Figure 5.4. The MLLD used here is the Thorlabs FPL1009P with the free spectral range $F \approx 43.45\,\mathrm{GHz}$.

The terahertz path consists of two pairs of polymethylpentene (TPX) lenses in a focused transmission-mode geometry. The interferometer is realized by splitting off fractions of the optical signals going to the terahertz emitter and detector, respectively, with a pair of 90:10 fused-fiber couplers and combining them in a 50:50 fused-fiber coupler. Two low-cost fiber-coupled telecom photodiodes are used to detect the interference signal. Their photocurrents are transimpedance-amplified with two variable-gain transimpedance amplifiers (TIAs), whose gains are adjusted to compensate any imbalances between the two photocurrents. The difference voltage is then generated by an analog difference amplifier. As explained in the previous paragraph, the signals from

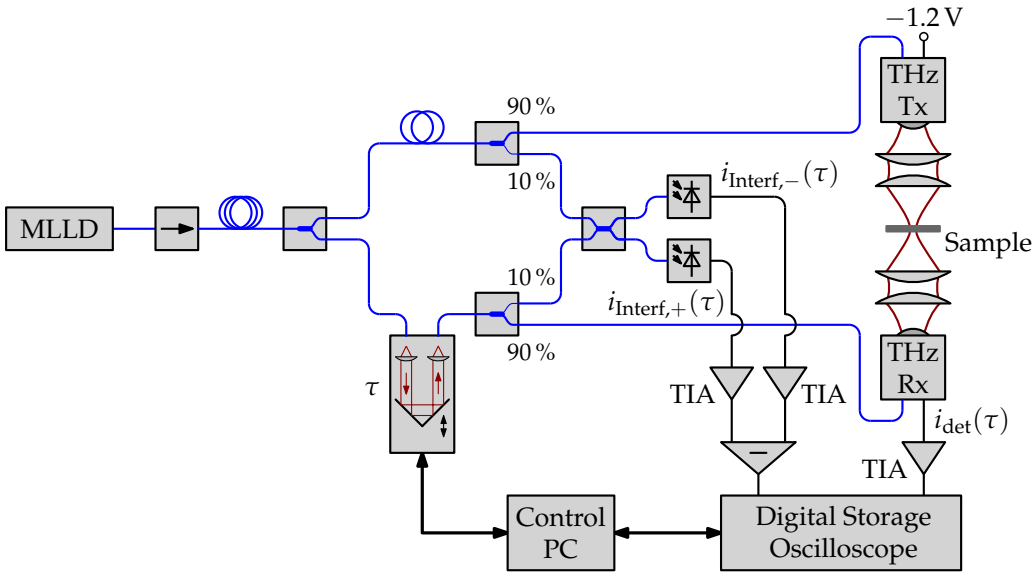

Figure 5.4: Experimental setup for the interferometric synchronization concept.

the terahertz detector and the interferometer, respectively, are synchronously sampled on two channels of a digital storage oscilloscope (DSO). Conveniently, the DSO is triggered on the rising edge of the signal from the interferometer, so that the traces from the DSO are already roughly synchronized. Further experimental details can be found in Ref. [3].

An example of the sampled voltages is depicted in Figure 5.5. Plot (a) shows the signals without a sample in the terahertz path (i.e. the reference signals) and plot (b) shows the signals when a 1 mm thick cyclic olefin copolymer (COC) sample is placed in the focus of the terahertz path. The blue curve represents the signal from the interferometer, the yellow curve represents its envelope, and the black crosses mark two maxima. The red curve represents the synchronously sampled signal from the terahertz detector. It can be seen that due to the DSO being triggered off of the signal from the interferometer, the positions of the maxima change only slightly between the measurements, whereas the signal from the terahertz detector – as expected – changes its position and shape as the COC sample is placed in the terahertz path.

After applying the synchronization algorithm, averaging over 100 traces, and scaling with the gain of the transimpedance amplifier, the photocurrents depicted in Figure 5.6 (a) result. The discrete Fourier transform of these photocurrents yields the

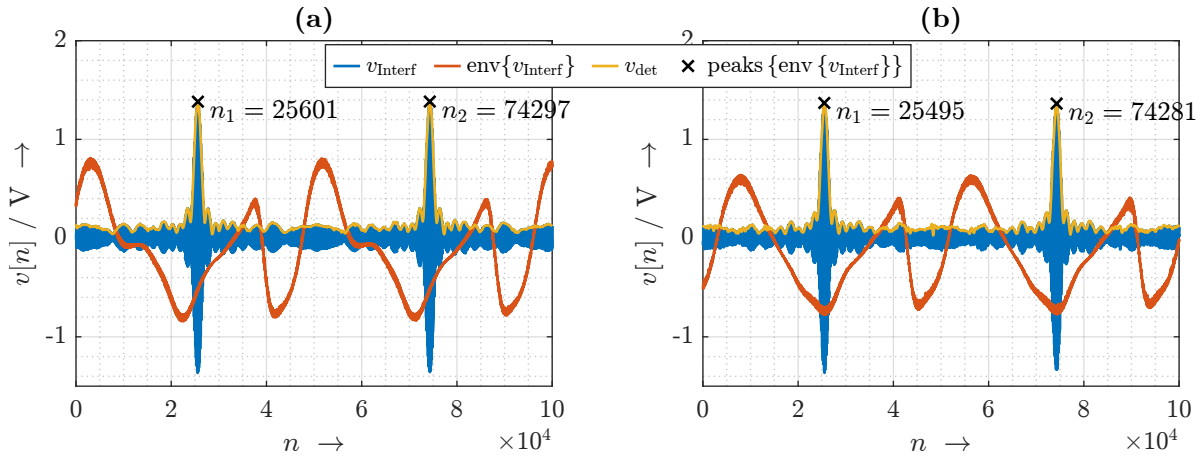

Figure 5.5: Sampled voltages **(a)** without a sample in the terahertz path and **(b)** with the COC sample in the focus of the terahertz path. The blue curve represents the signal from the interferometer, the yellow curve represents its envelope, and the black crosses mark two maxima. The red curve represents the synchronously sampled signal from the terahertz detector.

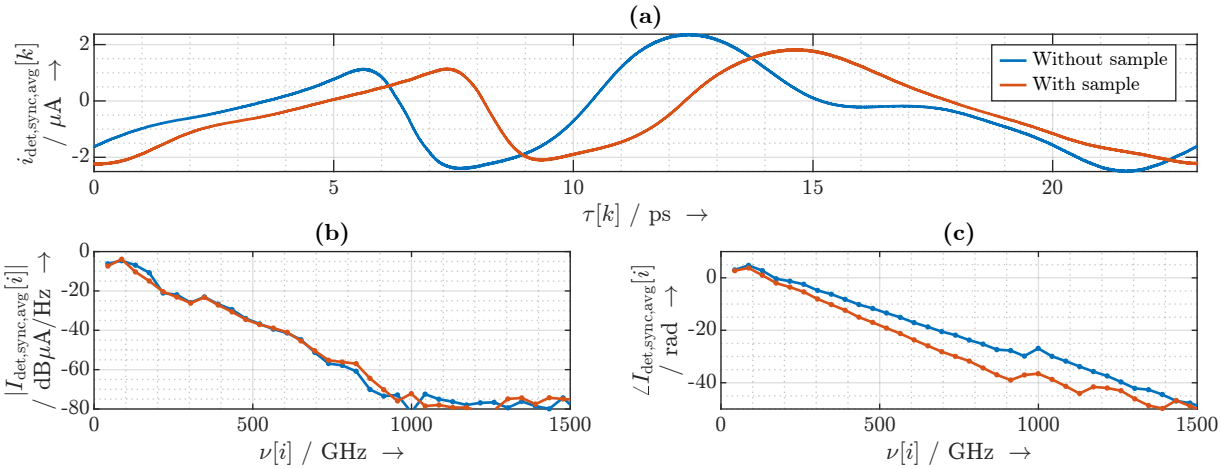

Figure 5.6: **(a)** Synchronized and scaled detected photocurrents without and with the COC sample in the terahertz path. Absolute value **(b)** and phase **(c)** of the photocurrents in plot **(a)**.

discrete amplitude and phase spectra depicted in plots (b) and (c), respectively. The amplitude spectra in plot (b) are virtually identical with and without the sample due to the negligible loss of the COC material. They intersect the noise floor at a frequency of about 1 THz. The phase spectra exhibit a linear behavior for frequencies below that frequency. Congruent with the delay introduced by the dielectric sample, the slope with the sample is more negative than without.

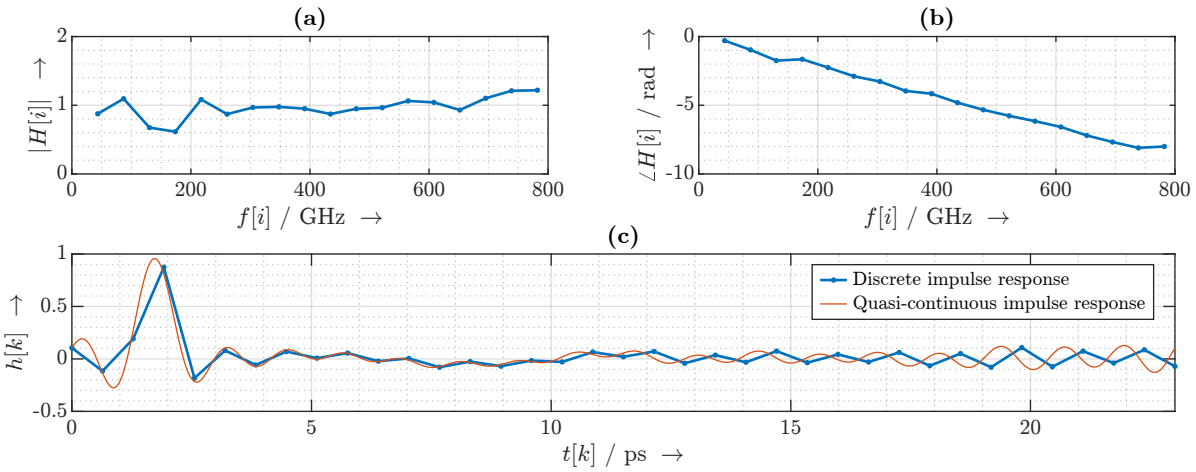

Figure 5.7: (a) Magnitude and **(b)** phase of the discrete transfer function of the sample. **(c)** Impulse response of the sample.

By zero-forcing equalization, the discrete transfer function

$$H[i] = \frac{I_{\text{det,sync,avg,sample}}[i]}{I_{\text{det,sync,avg,reference}}[i]}\,,\ 1 \leq i \leq i_{\max} \tag{5.11}$$

of the sample is calculated. The magnitude and phase of the discrete transfer function for the case $i_{\max} = 18$ are depicted in Figure 5.7 (a) and (b), respectively. The discrete and periodic impulse response calculated by discrete inverse Fourier transform is shown as the blue trace in plot (c). The red trace shows the quasi-continuous impulse response determined by zero-padding interpolation of the blue trace. The pulse maximum of the interpolated trace is at $t = 1.74\,\text{ps}$. This value is congruent with the slope of the discrete transfer function and in good agreement with the calculated position

$$t_{\text{calc}} = \frac{d \cdot (n-1)}{c_0} \approx \frac{1\,\text{mm} \cdot (1.52-1)}{c_0} \approx 1.73\,\text{ps}\,, \tag{5.12}$$

where $d = 1\,\text{mm}$ is the thickness of the sample, $n \approx 1.52$ is the average refractive index of COC within the considered frequency range measured with a commercially available THz-TDS system, and c_0 is the speed of light in vacuum [11].

[11] I would like to thank M. Sc. Tobias Kubiczek for 3D-printing the COC sample and characterizing it with a Menlo K15 THz-TDS system.

5.4 Interferometric correction of the delay axis

In the previous paragraph, it has been shown that the envelope of the interferogram can be used to accurately synchronize the sampled photocurrent from the terahertz detector. This was, however, under the assumption that the delay increased linearly within one period of the interferogram's envelope. To correct possible non-linearities of the delay axis in between these two points, we can employ the internal oscillation of the interferogram. There are certainly many approaches to do so. In this paragraph, a particularly simple implementation is described.

As previously mentioned, under the assumption of a linear delay axis, the Fourier transform of the interferogram is equal the power spectral density of the electric field emitted by the MLLD. Thus, the bandwidth of the interferogram also matches that of the MLLD's spectrum. Although the bandwidth is of the order of 2 to 3 THz, this is still small compared to the optical carrier frequency $f_0 \approx 192\,\mathrm{THz}$. Thus, the interferogram can be considered a "narrow-band" signal. Consequentially, the distance between the zeros of the interferogram is roughly constant and approximately equal to ${f_0}^{-1}/2 \approx 2.6\,\mathrm{fs}$. The numerically determined distance between neighboring zeros of the interferogram depicted in Figure 5.3 (b) is shown in Figure 5.8. It can be seen that the distance fluctuates between 2.599 and 2.626 fs. The inset histogram in Figure 5.8 shows the distribution of the distances between two neighboring zeros.

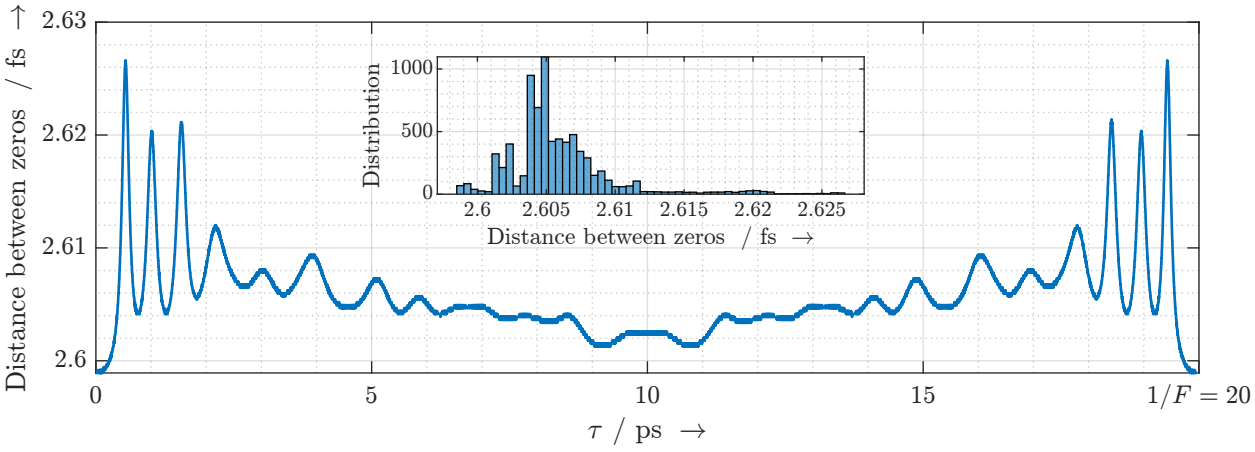

Figure 5.8: Numerically determined distance between neighboring zeros of the interferogram depicted in Figure 5.3. The inset shows the distribution of the distances.

In the first approximation, the zeros are assumed to be equidistant. Under this assumption, the determination of the delay axis is as simple as determining the sample indices of the zeros of the sampled interferogram and assigning to them their respective delay values according to the optical carrier frequency of the MLLD. One period of the interferogram contains

$$N_{\text{zeros}} = \frac{2 \cdot f_{\text{avg}}}{F} \tag{5.13}$$

zeros, where $f_{\text{avg}} \gtrapprox f_0$ is the "mean" frequency of the MLLD. Zeros can be found at the sample indices $k_{\text{zero},m}$, $1 \leq m \leq N_{\text{zeros}}$, i.e.

$$i_{\text{Interf}}[k_{\text{zero},m}] = 0 \text{ , } 1 \leq m \leq N_{\text{zeros}} \text{ .} \tag{5.14}$$

The delays at these indices are then

$$\tau[k_{\text{zero},m}] = \frac{k_{\text{zero},m}}{2 \cdot f_{\text{avg}}} \text{ , } 1 \leq m \leq N_{\text{zeros}} \text{ .} \tag{5.15}$$

This corrected delay axis can then be used for the evaluation of the sampled photocurrent from the terahertz detector. However, there are a few aspects to be considered:

- The interferogram needs to be sampled with a sufficiently high sampling rate for accurate localization of its zeros.
- The delay is accurately determined only for the sample indices $k_{\text{zero},m}$. For the indices k in between, the values need to be interpolated for complete retrieval of the delay axis. However, this is only a hypothetical problem, as the distance between the zeros of the interferogram is orders of magnitude smaller than the period of the highest-frequency component in the detected terahertz signal: $f_{\text{avg}} \gg (N-1) \cdot F$. The photocurrent from the terahertz detector can be resampled with virtually no loss of information.
- As depicted in Figure 5.8, the distance between the zeros of the calculated interferogram is not actually constant. The resulting error of the delay axis for a well-chosen value of f_{avg} is depicted in Figure 5.9. It can be seen that the error does not exceed 4 fs, which is negligible for a terahertz signal that does not exceed a frequency of 2 THz.

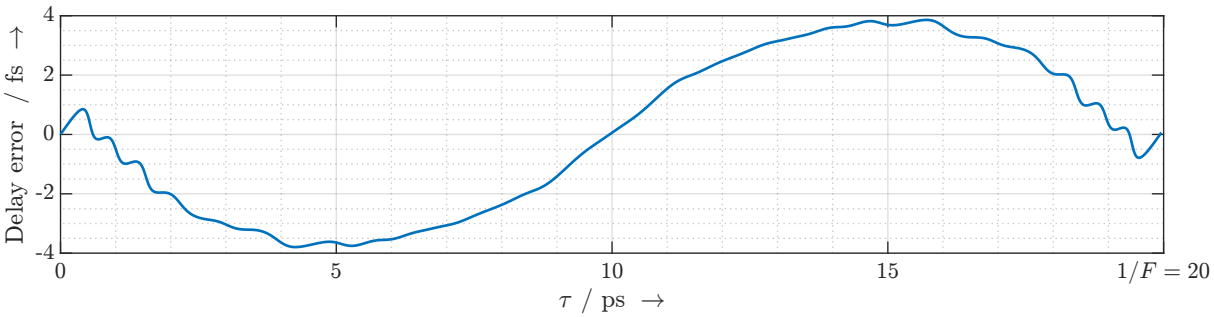

Figure 5.9: Delay error resulting from the assumption of equidistant zeros of the interferogram. The "mean" frequency $f_{\text{avg}} \approx 191.88\,\text{THz}$ has been chosen such that the error is equal to zero at the beginning and at the end of the period.

We can see that the synchronous sampling of the interferogram between the non-delayed and the delayed optical signal in an UHRR-THz-TDS system makes it possible to both synchronize and correct the delay axis [12]. Besides improving the phase accuracy, bandwidth, and dynamic range achievable with a conventional ODU, this concept allows the implementation of methods to simplify the system and to increase the measurement speed. Firstly, the movement of the ODU does not have to be synchronized with the data acquisition, as the synchronization is performed *a posteriori* according to the measured data. Secondly, the entire range of the ODU, including the acceleration and deceleration phases, can be used. Beyond that, the movement of the ODU may be inherently non-linear, as is, for example, the case if the mirror is moved sinusoidally by a voice-coil motor.

[12] First experimental results for the correction of the delay axis have been demonstrated under my supervision as part of the master thesis entitled "Model-supported interferometric reconstruction of the time axis in an ultra-high repetition rate terahertz time-domain spectrometer" by M. Sc. Peter Krämer. Using the setup shown in Figure 5.4, it was found that the mode-locking of the Thorlabs FPL1009P is very unstable, leading to a noisy interferogram. As part of the thesis, an elaborate but computational expensive algorithm for the noise-resilient determination of the zeros was developed. It was found that by correcting the delay axis, the apparent width of all spectral components of the detected photocurrent is decreased while the magnitude of most spectral components is increased by up to 8 dB. The increased magnitude is particularly noticeable at the upper end of the spectrum in the frequency range from 1.0 to 1.3 THz. Above all, it was found that a superior improvement in signal-to-noise ratio is achievable by averaging of the measured traces after correction of the delay axis. Later experiments have shown that the interferogram generated with the two-section QD laser from Fraunhofer HHI is significantly less noisy, so that its zeros can be directly determined after adequate low-pass filtering.

CHAPTER

SIX

ASPECTS OF PHOTONIC BEAM STEERING FOR UHRR-THZ-TDS

Beam steering is the ability of an RF transmitter to change the direction to which it transmits a signal or, vice versa, the ability of an RF receiver to change the direction from which it receives signals. Historically, as the carrier frequencies and bandwidths of RF systems have increased, beam steering has always been one of the last techniques to be implemented because its high system complexity requires a high degree of technological maturity. Traditionally, in each frequency range beam steering has evolved from mechanically rotating a directional antenna, over analog beam steering in the RF band, to complex digital beam forming in the baseband. Beam steering can fulfill a variety of purposes. In communications applications, it can be as simple as maximizing the power transfer between a transmitter and a receiver by directing their radiation pattern maxima towards each other or as complex as maximizing the signal-to-noise power ratio of multiple communication channels between multiple transmitters and multiple receivers. In sensing applications, it can be as simple as maximizing the power density and sensitivity towards a target or as complex as achieving high spatial resolution by overlapping narrow beams from the transmitter and receiver.

Beam steering at terahertz frequencies is still at a very early stage due to the relative immaturity of terahertz technology and a few unique challenges. Some of these

challenges are due to the high carrier frequency, some are due to the extremely wide bandwidth. However, the frequency-discrete nature of UHRR-THz-TDS can lead to some significant simplifications. The exploitation of these simplifications is the subject of this chapter.

In Section 6.1, the fundamentals of antenna array theory are summarized, some of the challenges of wideband beam steering at terahertz frequencies are discussed, and the use of photonic beam steering for that purpose is motivated. In Section 6.2, a *quasi*-true time delay photonic beam steering concept for UHRR-THz-TDS is introduced. Finally, in Section 6.3, it is demonstrated that non-uniform array element distributions promise to show good performance across the entire frequency range of the system.

6.1 Fundamentals and challenges of wideband beam steering at terahertz frequencies

6.1.1 Fundamentals of phased array beam steering

The prototype of a linear N-element phased array is sketched in Figure 6.1.

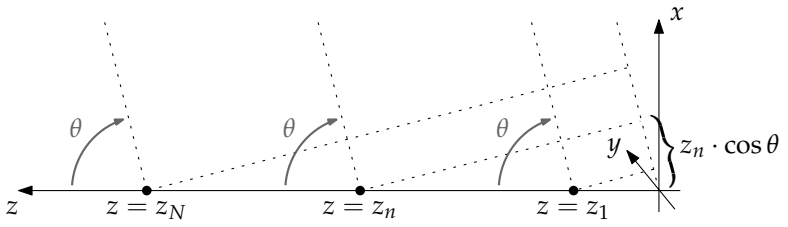

Figure 6.1: Sketch of a linear N-element array of antennas located at $x = y = 0$, $z = z_n$.

The array consists of N antennas that are located at the coordinates $z = z_n$ along the z-axis. We assume that each element n of the array is driven by a current

$$\begin{aligned} i_n(t) &= \mathrm{Re}\left\{ I_n \cdot \exp\left(\mathrm{j} \cdot 2\pi \cdot f \cdot t\right) \right\} \\ &= \mathrm{Re}\left\{ \hat{I}_n \cdot \exp\left(\mathrm{j}\,\varphi_n\right) \cdot \exp\left(\mathrm{j} \cdot 2\pi \cdot f \cdot t\right) \right\} \ , \end{aligned} \tag{6.1}$$

where f is the operating frequency and the phasor I_n describes the magnitude and phase of the current driving the element n. In the far field, the electric field generated by each antenna is proportional to the current flowing in the antenna. At a distance d

from the array, the electric field generated by the antenna n at the elevation angle θ can be approximated by the phasor

$$E_n \propto I_n \cdot \exp\left(\mathrm{j} \cdot \frac{2\pi \cdot f \cdot z_n \cdot \cos\theta}{c_0}\right) \cdot \frac{\exp\left(-\mathrm{j} \cdot \frac{2\pi \cdot f \cdot d}{c_0}\right)}{d} \,. \tag{6.2}$$

The term $\exp\left(-\mathrm{j} \cdot 2\pi \cdot f \cdot d/c_0\right)/d$ describes the phase change and decay of the electric field due to the propagation along the distance d. It is approximately equal for all elements of the array. The term $\exp\left(\mathrm{j} \cdot 2\pi \cdot f \cdot z_n \cdot \cos\theta/c_0\right)$ describes the phase lead of the field generated by the antenna at the position $z = z_n$ relative to a virtual antenna at the position $z = 0$. We can define a term

$$A_n = \hat{A}_n \cdot \exp\left[\mathrm{j} \cdot \left(\frac{2\pi \cdot f \cdot z_n \cdot \cos\theta}{c_0} + \varphi_n\right)\right] \tag{6.3}$$

that describes the relative contribution of the element n. The sum over the contributions of all elements

$$g(\theta, f) = \sum_{n=1}^{N} A_n = \sum_{n=1}^{N} \hat{A}_n \cdot \exp\left[\mathrm{j} \cdot \left(\frac{2\pi \cdot f \cdot z_n \cdot \cos\theta}{c_0} + \varphi_n\right)\right] \tag{6.4}$$

is the so-called *array factor*. It quantifies the ratio of the electric field generated by the array in the direction θ relative to that generated by a single antenna assuming that all antennas exhibit the same antenna pattern. The array factor $g(\theta, f)$ describes the interference pattern generated by the interference between the fields emitted by the elements of the antenna array. Perfect constructive interference leads to main lobes, perfect destructive interference leads to nulls in the interference pattern. The array factor is the basis for phased array beam steering, and there are hundreds of papers and textbooks describing its use.

With the knowledge of the array factor and the element factor, i.e. the antenna pattern of the array elements, the directivity of the array can be calculated. Assuming isotropic radiators, the directivity of the linear array becomes

$$D(\theta, f) = \frac{2 \cdot |g(\theta, f)|^2}{\int_0^{\pi} |g(\theta, f)|^2 \cdot \sin\theta \, \mathrm{d}\theta} \,. \tag{6.5}$$

The angle-dependent directivity $D(\theta, f)$ describes the power density in the direction θ relative to the average radiated power density.

In the following, the simplest possible implementation, in which the amplitudes $\hat{A}_n \equiv \hat{A}_0$ are constant and the phases φ_n are chosen such that a main lobe is created at the angle $\theta = \theta_0$ at the frequency $f = f_0$, is considered. Intuitively, this is achieved by choosing the phases

$$\varphi_n(\theta_0) = -\frac{2\pi \cdot f_0 \cdot z_n \cdot \cos\theta_0}{c_0} \,. \tag{6.6}$$

While the concept of phased array beam steering is in principle simple, its implementation in a wideband terahertz system is not. Deliberately leaving aside the technological hurdles, the key challenges can be located in three areas.

6.1.2 Scarcity of terahertz power

At microwave and millimeter-wave frequencies, RF signals with a power of several watts can be generated and, most importantly, amplified to compensate for losses. In the terahertz range, RF power is a much more scarce resource. The generated power is typically in the low milliwatt range in the case of electronic sources and even lower for photonic sources like those described in the previous chapters. The radiated power of photonic terahertz sources typically drops from a few hundred microwatt at the lower end of the terahertz range to a few hundred nanowatt around 1 THz. Moreover, it is categorically impossible to construct an efficient amplifier that supports the same frequency range due to the bandwidth limitations of the required matching networks as well as due to the limited cutoff frequency of transistors.

Although the low available power and the lack of amplifiers complicate their realization, phased arrays can play a key role in increasing the range of wideband terahertz systems. Considering an N-element array with the uniform amplitudes $\hat{A}_0$, the array factor of the main lobe reaches the maximum value

$$g(\theta = \theta_0) = \sum_{n=1}^{N} \hat{A}_0 = N \cdot \hat{A}_0 \,. \tag{6.7}$$

The value of the amplitude $\hat{A}_0$ depends on the implementation of the beam steering network. Consider the three different topologies of a photodiode-driven beam steering network sketched in Figure 6.2.

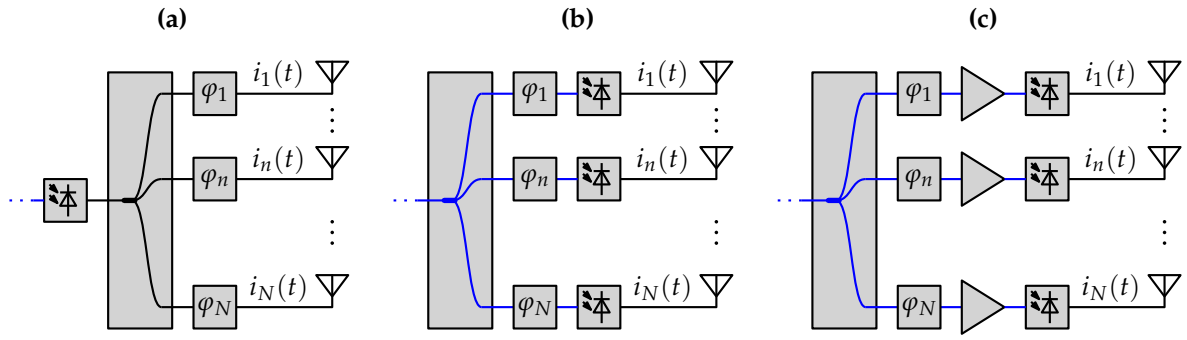

Figure 6.2: Topologies of a photodiode-driven beam steering network. **(a)** Electric, **(b)** passive photonic, and **(c)** active photonic. Blue lines indicate optical and black lines indicate electrical signals.

The topology in sketch (a) represents a classical electric beam steering network. The RF signal from the photodiode is split into N branches, each of which feeds one element of the antenna array. Setting aside losses in the splitter and in the waveguides, the power splitting causes the amplitude of each antenna to be $\hat{A}_0 = \hat{A}_{\text{in}}/\sqrt{N}$. Thus, the array factor of the main lobe is

$$g_{\text{a}}(\theta = \theta_0) = N \cdot \frac{\hat{A}_{\text{in}}}{\sqrt{N}} = \sqrt{N} \cdot \hat{A}_{\text{in}} \,. \tag{6.8}$$

The power density in the main lobe is thus increased by the factor

$$\frac{{g_{\text{a}}}^2(\theta = \theta_0)}{\hat{A}_{\text{in}}^2} = N \tag{6.9}$$

compared to the case of a single antenna with the amplitude $\hat{A}_{\text{in}}$. In other words, the total radiated power is not increased, but it is directed towards the main lobe.

The topology in sketch (b) represents a passive photonic beam steering network. The optical signal from the light source is split into N branches, each of which feeds one photodiode. Each photodiode in turn feeds one element of the antenna array. In this case, the optical power from the light source is shared between N photodiodes. However, since the photocurrent generated in a photodiode is proportional to the optical power, the amplitude of each antenna becomes $\hat{A}_0 = \hat{A}_{\text{in}}/N$. This yields the array factor

$$g_{\text{b}}(\theta = \theta_0) = N \cdot \frac{\hat{A}_{\text{in}}}{N} = \hat{A}_{\text{in}} \,. \tag{6.10}$$

We can see that in this case the power density is not increased compared to a single antenna. The increase in directivity is compensated by the decrease in transmitted power. However, the topology in sketch (b) neglects that optical signals can very well be amplified. Optical power is not scarce in the way terahertz power is.

Sketch (c) shows an active photonic beam steering network in which the optical signal in each branch is amplified such that it remains constant independent of the number of branches N. In this case, the amplitude of each antenna remains $\hat{A}_0 = \hat{A}_{\mathrm{in}}$, and the array factor becomes

$$g_{\mathrm{c}}(\theta = \theta_0) = N \cdot \hat{A}_{\mathrm{in}} \,. \tag{6.11}$$

Now the power density in the main lobe is increased by the factor N^2 compared to a single antenna. This highlights that a properly designed photonic beam steering network is the optimum solution for a photodiode-driven transmitter. It should be noted that the optical power of the light source or of a single amplifier is typically larger than the damage threshold of a photodiode, so that realistically fewer amplifiers than photodiodes are needed. The interested reader is referred to Ref. [4], in which I show a complete power budget analysis that assumes realistic values for all components of the photonic beam steering network.

6.1.3 Grating lobes

Looking at the formula for the array factor

$$g(\theta, f_0) = \sum_{n=1}^{N} \hat{A}_0 \cdot \exp\left[\mathrm{j} \cdot \left(\frac{2\pi \cdot f_0 \cdot z_n \cdot \cos\theta}{c_0} + \varphi_n\right)\right] \tag{6.12}$$

at the frequency $f = f_0$, it is evident that perfect constructive interference, and thus a main lobe, occurs for

$$\exp\left[\mathrm{j} \cdot \left(\frac{2\pi \cdot f \cdot z_n \cdot \cos\theta}{c_0} + \varphi_n\right)\right] = \text{const.} \; \forall \; n \,, \tag{6.13}$$

Without loss of generality, we can consider the simple case

$$\exp\left[\mathrm{j} \cdot \left(\frac{2\pi \cdot f_0 \cdot z_n \cdot \cos\theta}{c_0} + \varphi_n\right)\right] = 1 \; \forall \; n \,, \tag{6.14}$$

i.e.

$$\frac{2\pi \cdot f_0 \cdot z_n \cdot \cos\theta}{c_0} + \varphi_n = p \cdot 2\pi \ , \ p \in \mathbb{Z} \ , \ \forall \ n \ . \tag{6.15}$$

Thus, to steer the beam to the angle $\theta = \theta_0$, the phase shifts

$$\varphi_n = -\frac{2\pi \cdot f_0 \cdot z_n \cdot \cos\theta_0}{c_0} \ . \tag{6.16}$$

are chosen. In this case, perfect constructive interference results for

$$\cos\theta - \cos\theta_0 = \frac{p \cdot c_0}{f_0 \cdot z_n} \ , \ p \in \mathbb{Z} \ , \ \forall \ n \ . \tag{6.17}$$

Depending on the steering angle θ_0 and the locations z_n of the antennas, this equation has one or more solutions for θ. Assuming that the antennas are equidistantly spaced along the z-axis with the element spacing d, i.e.

$$z_n = n \cdot d \ , \tag{6.18}$$

perfect constructive interference results for all angles θ that fulfill the equation

$$\cos\theta - \cos\theta_0 = \frac{p \cdot c_0}{f_0 \cdot n \cdot d} \ , \ p \in \mathbb{Z} \ , \ \forall \ n \ . \tag{6.19}$$

Because n is an integer number and p is an arbitrary integer number, we can substitute $r = p/n$ to get the simplified equation

$$\cos\theta - \cos\theta_0 = r \cdot \frac{c_0}{f_0 \cdot d} \ , \ r \in \mathbb{Z} \ . \tag{6.20}$$

For $0 \leq \theta \leq 180°$, the equation has the solutions

$$r \in \left\{ -\left\lfloor \frac{f_0 \cdot d}{c_0} \cdot (1 - \cos\theta_0) \right\rfloor \ , \ \ldots \ , \ -1 \ , \ 0 \ , 1 \ , \ \ldots \ , \ \left\lfloor \frac{f_0 \cdot d}{c_0} \cdot (1 - \cos\theta_0) \right\rfloor \right\} \tag{6.21}$$

with the corresponding beam directions

$$\theta_r = \cos^{-1}\left(r \cdot \frac{c_0}{f_0 \cdot d} + \cos\theta_0 \right) \ . \tag{6.22}$$

The case $r = 0$ represents the main lobe of the array's radiation pattern, whereas the cases $|r| > 0$ represent so-called *grating lobes*. When the beam is steered in the broadside direction $\theta_0 = 90°$, there are no grating lobes if the element spacing is less than

one wavelength, i.e. for $d < c_0/f_0$. As the beam is steered away from the broadside, the maximum element spacing that does not exhibit grating lobes decreases. In the end-fire case, grating lobes appear if the element spacing exceeds half a wavelength, i.e. for $d \geq c_0/(2 \cdot f_0)$.

At the same time, it can be shown [116] that the directivity of the main lobe of a uniform antenna array that is steered to the broadside direction is given by

$$D_{\text{max, broadside}} = \frac{2 \cdot L}{c_0/f_0}\,, \tag{6.23}$$

where L is the total length of the array. To maximize the directivity while at the same time avoiding grating lobes, it is thus common to choose the "half-wavelength" element spacing $d = c_0/(2 \cdot f_0)$. However, the targeted high frequency and large bandwidth of photonic terahertz systems impose a couple of challenges.

Minimum spacing

The minimum achievable element spacing is determined by the size of the individual antennas as well as their feeding network. If we consider a system operating from 50 to 1000 GHz, the relative signal bandwidth is more than a decade. The efficient radiation of this signal requires broadband antennas. However, the transversal dimensions of planar broadband antennas, such as logarithmic spiral antennas or bowtie antennas, are typically of the order of half a wavelength at the *lowest* frequency. At the same time, the antenna spacing that is required to avoid grating lobes across the entire bandwidth is half a wavelength at the *highest* frequency. A possible solution is optimizing the antennas for the upper end of the spectrum and accepting their reduced radiation efficiency at the lower end of the spectrum. This unideal approach may be acceptable for some applications given that the transmit power at the lower end of the spectrum is orders of magnitude higher than at the upper end.

However, another factor that limits the minimum element spacing is the feeding network, as the waveguides leading to the antennas have a certain width. For example, it has been noted in Ref. [117] that in the case of a fiber-coupled photonic beam steering array, the thickness of the fiber cladding forces the distance between the antennas

to be larger than 125 µm [13]. This problem can be addressed with integrated optical waveguides that couple the light into the individual antenna-integrated photodiodes.

Operating bandwidth

The large targeted bandwidth leads to conflicting requirements for the element distribution of the array. On the one hand, the array shall be electrically large to achieve a high directivity. On the other hand, the element spacing shall be small enough to avoid grating lobes. Both requirements are under the constraint that the technological effort is proportional to the number of array elements.

This conflicting requirement is illustrated in Figure 6.3. It shows the frequency-dependent directivity of a uniformly spaced linear 10-element array of isotropic radiators across the frequency range from 50 to 1000 GHz for the broadside case $\theta_0 = 90°$. Plot (a) shows the case where the element spacing is half a wavelength at 1000 GHz, i.e. $d \approx 0.15$ mm. Plot (b) shows the case where the element spacing is half a wavelength at 50 GHz, i.e. $d \approx 3$ mm. The frequency-dependent directivity is calculated according to Equation (6.5) with the array factor

$$g(\theta, f) = \sum_{n=1}^{10} \exp\left(\mathrm{j} \cdot \frac{2\pi \cdot f \cdot n \cdot d \cdot \cos\theta}{c_0} \right) . \tag{6.24}$$

The radiation pattern for the case of a half-wavelength element spacing at 1000 GHz, as expected, shows one main lobe as well as several lower-amplitude side lobes across the entire frequency range. The side lobes are due to the uniform amplitude distribution of the array. For this dense element distribution, the directivity increases monotonically from approximately 0 dBi at 50 GHz to 10 dBi at 1000 GHz.

The radiation patterns for the case of a half-wavelength element spacing at 50 GHz show a complex structure due to a large number of grating lobes. Grating lobes appear when the element spacing exceeds one wavelength, i.e. for $f \geq 100$ GHz. As expected from Equations (6.21) and (6.22), the number of grating lobes increases with increasing

[13] In most cases, the antennas are placed behind a dielectric lens to facilitate efficient radiation into free space. In those cases, the refractive index of the lens needs to be considered in the array factor. The wavelength in the dielectric medium is shorter than in air, so – as discussed in Ref. [117] – the antennas need to be placed closer together than if they were placed in air.

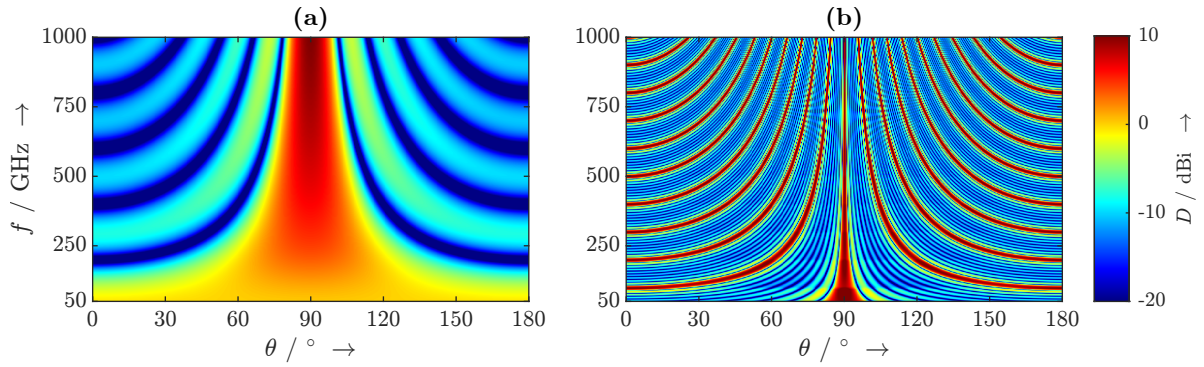

Figure 6.3: Calculated radiation pattern of a uniformly spaced linear 10-element array of isotropic radiators in the broadside case $\theta_0 = 90°$. The distance between the elements is **(a)** $d \approx 0.15\,\text{mm}$ and **(b)** $d \approx 3\,\text{mm}$, respectively.

frequency, and the grating lobes move towards the main lobe. Notably, the directivity of the main lobe fluctuates between 8.7 and 12.2 dBi.

This behavior is easy to explain. As the array grows electrically larger with increasing frequency, the theoretical maximum directivity increases linearly. However, since power is equally shared between the main lobe and the grating lobes, the directivity of the main lobe decreases in a stepwise fashion with each appearance of a grating lobe. It is shown in Section 6.3 that optimized non-uniform spatial element distributions can be used to construct an array that shows reasonable directivity across the entire frequency range without the appearance of grating lobes.

6.1.4 Beam squint

In the previous section, we have seen how the beam is steered to the angle θ_0 at the frequency f_0 by driving the elements of the array with the phases

$$\varphi_n = -\frac{2\pi \cdot f_0 \cdot z_n \cdot \cos\theta_0}{c_0} \,. \tag{6.25}$$

If the array is now considered at an arbitrary frequency f, the array factor becomes

$$\begin{aligned} g(\theta, f) &= \sum_{n=1}^{N} \hat{A}_0 \cdot \exp\left[\mathrm{j} \cdot \left(\frac{2\pi \cdot f \cdot z_n \cdot \cos\theta}{c_0} + \varphi_n\right)\right] \\ &= \sum_{n=1}^{N} \hat{A}_0 \cdot \exp\left[\mathrm{j} \cdot \left(\frac{2\pi \cdot f \cdot z_n \cdot \cos\theta}{c_0} - \frac{2\pi \cdot f_0 \cdot z_n \cdot \cos\theta_0}{c_0}\right)\right] \\ &= \sum_{n=1}^{N} \hat{A}_0 \cdot \exp\left[\mathrm{j} \cdot \frac{2\pi \cdot z_n \cdot (f \cdot \cos\theta - f_0 \cdot \cos\theta_0)}{c_0}\right] , \end{aligned} \tag{6.26}$$

so that the condition for perfect constructive interference becomes

$$\frac{f}{f_0} \cdot \cos\theta - \cos\theta_0 = \frac{p \cdot c_0}{f_0 \cdot z_n} \,,\; p \in \mathbb{Z} \,,\; \forall\, n \,. \tag{6.27}$$

We get the direction of the main lobe from the fundamental case $p = 0$, i. e.

$$\cos\theta = \frac{f_0}{f} \cdot \cos\theta_0 \,. \tag{6.28}$$

Only if the condition

$$\frac{f_0}{f} \cdot \cos\theta_0 \leq 1 \tag{6.29}$$

is fulfilled, there is a main lobe in the direction

$$\theta = \cos^{-1}\left(\frac{f_0}{f} \cdot \cos\theta_0\right) \,. \tag{6.30}$$

The direction of the main lobe obviously changes with frequency. This effect is well-known from wideband communication or radar systems under the name *beam squint*. However, these systems typically have relative bandwidths of a few percent, whereas

the wideband terahertz systems considered in this thesis exhibit a relative bandwidth of more than a decade. The beam squint not only causes the direction of the main lobe to change by an unacceptable amount, there can even be cases where there is no main lobe because Equation (6.29) is not fulfilled. These effects are illustrated in Figure 6.4 for the case of a 100-element uniformly spaced array with an element spacing that is equal to half a wavelength at 1000 GHz, i.e. $d \approx 0.15\,\mathrm{mm}$. The beam is steered in the directions $\theta_0 \in \{0^\circ\,,\, 45^\circ\,,\, 90^\circ\}$ at the frequency $f_0 = 500\,\mathrm{GHz}$. The frequency-dependent directivity is calculated according to Equation (6.5) using the array factor

$$g(\theta, f) = \sum_{n=1}^{100} \exp\left[\mathrm{j} \cdot \left(\frac{2\pi \cdot f \cdot n \cdot d \cdot \cos\theta}{c_0} + \varphi_n(\theta_0)\right)\right] \tag{6.31}$$

with the phases

$$\varphi_n(\theta_0) = -\frac{2\pi \cdot f_0 \cdot n \cdot d \cdot \cos\theta_0}{c_0}\,. \tag{6.32}$$

No beam squint occurs in the broadside case $\theta_0 = 90^\circ$ because the associated phase shifts are all zero. However, in the cases $\theta_0 = 0^\circ$ and $\theta_0 = 45^\circ$ the position of the main lobe is at the desired angle only at the frequency $f_0 = 500\,\mathrm{GHz}$. It moves away significantly from that angle for lower and higher frequencies. As expected, the beam disintegrates as it squints towards the end-fire position at the lower end of the frequency range.

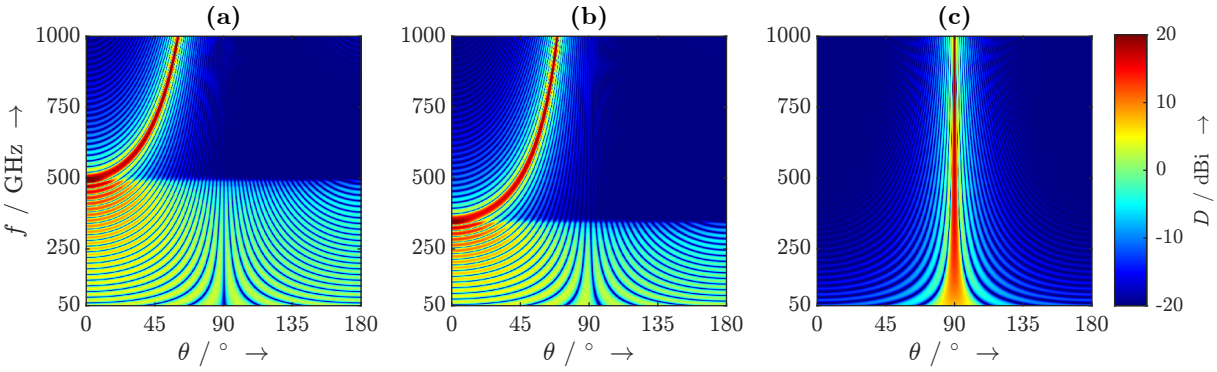

Figure 6.4: Calculated radiation pattern of a uniformly spaced linear 100-element phased array of isotropic radiators with the element spacing $d \approx 0.15\,\mathrm{mm}$. The beam is steered in the directions **(a)** $\theta_0 = 0^\circ$, **(b)** $\theta_0 = 45^\circ$, and **(c)** $\theta_0 = 90^\circ$, respectively, at the frequency $f_0 = 500\,\mathrm{GHz}$.

True time delay beam steering

A solution to the problem of beam squint is the well-known concept of *true time delay* (TTD) beam steering. The idea of TTD beam steering is to delay the signals at the individual elements of the array rather than shifting their phases. For TTD beam steering, the signal emitted by the array element n is delayed by

$$\tau_n = \frac{z_n \cdot \cos\theta_0}{c_0} \,. \tag{6.33}$$

By replacing the phase shifts in the phased array with "true" time delays, the array factor becomes

$$\begin{aligned} g(\theta, f) &= \sum_{n=1}^{N} \hat{A}_0 \cdot \exp\left[\mathrm{j} \cdot \left(\frac{2\pi \cdot f \cdot z_n \cdot \cos\theta}{c_0} - 2\pi \cdot f \cdot \tau_n\right)\right] \\ &= \sum_{n=1}^{N} \hat{A}_0 \cdot \exp\left[\mathrm{j} \cdot \frac{2\pi \cdot f \cdot z_n \cdot (\cos\theta - \cos\theta_0)}{c_0}\right] , \end{aligned} \tag{6.34}$$

so that the condition for perfect constructive interference at the frequency f becomes

$$\cos\theta - \cos\theta_0 = \frac{p \cdot c_0}{f \cdot z_n} \,,\ p \in \mathbb{Z} \,,\ \forall\, n \,. \tag{6.35}$$

The fundamental solution $p = 0$ gives the main lobe direction

$$\theta = \theta_0 \,. \tag{6.36}$$

By delaying the signal radiated by the element n with the delay τ_n, the TTD beam steering network compensates the phase lead it acquires in air in the direction θ_0 relative to the other elements. This causes the beam to be steered in the direction θ_0 independent of frequency. A simple visual explanation is sketched in Figure 6.5 assuming a pulsed signal. By delaying the signals before they are radiated, they are tempo-spatially prealigned, so that the pulse maxima overlap in the desired direction.

Photonic true time delay beam steering

While the TTD concept is theoretically simple, it is notoriously difficult to implement. The generation of a "true" time delay in an electric beam steering network requires the changing of the electrical length of transmission lines. Possible solutions are adjusting

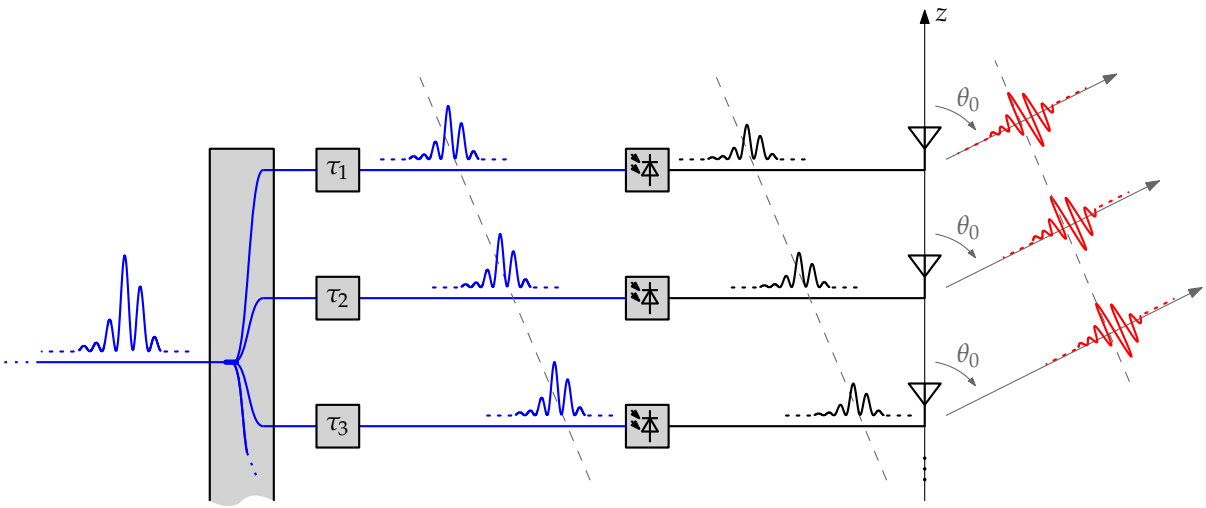

Figure 6.5: Illustration of the tempo-spatial alignment of the pulses emitted by an antenna array with TTD beam steering.

the propagation constant of a transmission line [118] or switching between transmission lines of different lengths [119]. However, none of these can achieve the necessary bandwidth due to the lack of sufficiently wideband single-mode waveguides and electronic components. The most promising solution is provided by photonic beam steering. It can be shown that a delay introduced to the optical signal driving a photonic transmitter is directly translated into the terahertz signal generated by the photonic transmitter. That makes it possible to perform beam steering of a terahertz signal by adjusting the delays in the optical domain. This concept is illustrated in Figure 6.5. The generation of adjustable delays is much easier and almost lossless in the optical domain, but only solutions that can be realized in a photonic integrated circuit (PIC) are practically meaningful. However, large arrays require large delays. For an array with the length L, the delay range that is required to be able to steer from one end-fire position to the other is $2L/c_0$. Realizing such delays in a PIC, for example with switched waveguides, is difficult and requires a lot of chip area. In the following section, it is shown that in the particular case of UHRR-THz-TDS a small delay range is sufficient to realize wideband beam steering without beam squint.

6.2 Quasi-true time delay photonic beam steering for UHRR-THz-TDS

In the case of UHRR-THz-TDS, it is possible to implement an approach that is a simplified adaptation of TTD. I have first published this concept under the name "*quasi*-true time delay" (QTTD) beam steering in Ref. [2] [14].

The transmit signal of an UHRR-THz-TDS system contains spectral components only at the frequencies $f = mF$, $m \in \mathbb{N}$. Thus, in the time domain it is periodic with $1/F$. This means that delaying the signal by an integer multiple of $1/F$ leads to the exact same signal. If we consider this in the calculation of the delays required for TTD beam steering, Equation (6.33) can be modified to

$$\boxed{\tau_{n,\,\mathrm{mod}} = \frac{z_n \cdot \cos\theta_0}{c_0} \bmod \frac{1}{F}\,,} \tag{6.37}$$

where "mod" denotes the modulo operator. This equation gives a value between 0 and $1/F$ by which the signal that is radiated by the element n needs to be delayed in order to steer the beam in the direction θ_0. To analyze the functionality of this approach, the direction of the main lobe needs to be verified and the resulting radiation patterns need to be evaluated.

Plugging the delays calculated according to Equation (6.37) into Equation (6.34) yields the array factor

$$g(\theta, f) = \sum_{n=1}^{N} \hat{A}_0 \cdot \exp\left[\mathrm{j} \cdot 2\pi \cdot f \cdot \left(\frac{z_n \cdot \cos\theta}{c_0} - \frac{z_n \cdot \cos\theta_0}{c_0} \bmod \frac{1}{F})\right)\right]. \tag{6.38}$$

Evaluating this array factor at the discrete frequency $f = mF$, we get

$$g(\theta, f = mF) = \sum_{n=1}^{N} \hat{A}_0 \cdot \exp\left[\mathrm{j} \cdot 2\pi \cdot mF \cdot \left(\frac{z_n \cdot \cos\theta}{c_0} - \frac{z_n \cdot \cos\theta_0}{c_0} \bmod \frac{1}{F}\right)\right]. \tag{6.39}$$

[14] Ref. [2] is a joint paper between M. Sc. Xuan Liu and myself, to which we have equally contributed. We share its first authorship, and the individual author contributions are listed in the paper.

Using the definition

$$x \bmod y = x - \left\lfloor \frac{x}{y} \right\rfloor \cdot y \ , \ x, \, y \in \mathbb{R} \tag{6.40}$$
$$= x - \mu \cdot y \ , \ \mu \in \mathbb{N}$$

of the modulo operation, this can be rewritten as

$$g(\theta, f = mF) \tag{6.41}$$
$$= \sum_{n=1}^{N} \hat{A}_0 \cdot \exp\left\{ \mathrm{j} \cdot 2\pi \cdot \left[mF \cdot \left(\frac{z_n \cdot \cos\theta}{c_0} - \frac{z_n \cdot \cos\theta_0}{c_0} \right) + m\mu \right] \right\} , \mu \in \mathbb{N} \, .$$

Considering that $m\mu$ is an integer number, this can be simplified to

$$g(\theta, f = mF) = \sum_{n=1}^{N} \hat{A}_0 \cdot \exp\left(\mathrm{j} \cdot \frac{2\pi \cdot mF \cdot z_n \cdot (\cos\theta - \cos\theta_0)}{c_0} \right) . \tag{6.42}$$

This equation is equivalent to evaluating the array factor in the TTD case (see Equation (6.34)) only at the frequencies $f = mF$. It is thus easy to see that the main lobe is at the angle θ_0 at the frequencies $f = mF$. This QTTD approach is a promising solution for photonic beam steering for UHRR-THz-TDS because the required delays in the range from 0 to $1/F$ are quite realistic to be realized as switched waveguides in a PIC.

Exemplary radiation patterns using the QTTD approach are illustrated in Figures 6.6 and 6.7. The plots show the calculated radiation patterns of a 100-element uniformly spaced array with an element spacing that is equal to half a wavelength at 1000 GHz, i.e. $d \approx 0.15\,\mathrm{mm}$. The beam is steered in the directions $\theta_0 \in \{0^\circ \ , \ 45^\circ \ , \ 90^\circ\}$ by applying the delays

$$\tau_{n,\,\mathrm{mod}} = \frac{nd \cdot \cos\theta_0}{c_0} \bmod \frac{1}{F} \, , \tag{6.43}$$

with $F = 50\,\mathrm{GHz}$. The frequency-dependent directivity is calculated according to Equation (6.5) using the array factor

$$g(\theta, f) = \sum_{n=1}^{100} \exp\left[\mathrm{j} \cdot 2\pi \cdot f \cdot \left(\frac{nd \cdot \cos\theta}{c_0} - \frac{nd \cdot \cos\theta_0}{c_0} \bmod \frac{1}{F}) \right) \right] . \tag{6.44}$$

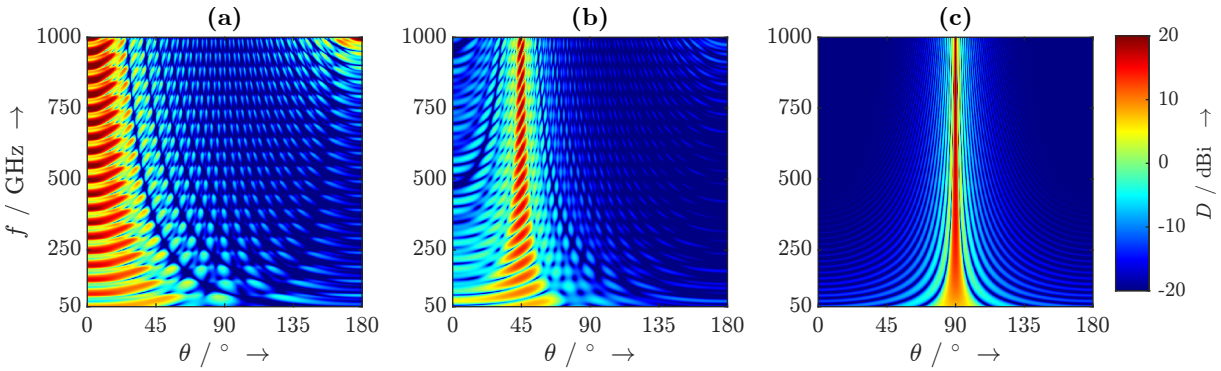

Figure 6.6: Calculated radiation pattern of a uniformly spaced linear 100-element array of isotropic radiators with the element spacing $d = 0.15\,\text{mm}$. The beam is steered in the directions **(a)** $\theta_0 = 0°$, **(b)** $\theta_0 = 45°$, and **(c)** $\theta_0 = 90°$, respectively, using the QTTD approach for $F = 50\,\text{GHz}$. The radiation patterns are plotted with a frequency resolution of 1 GHz.

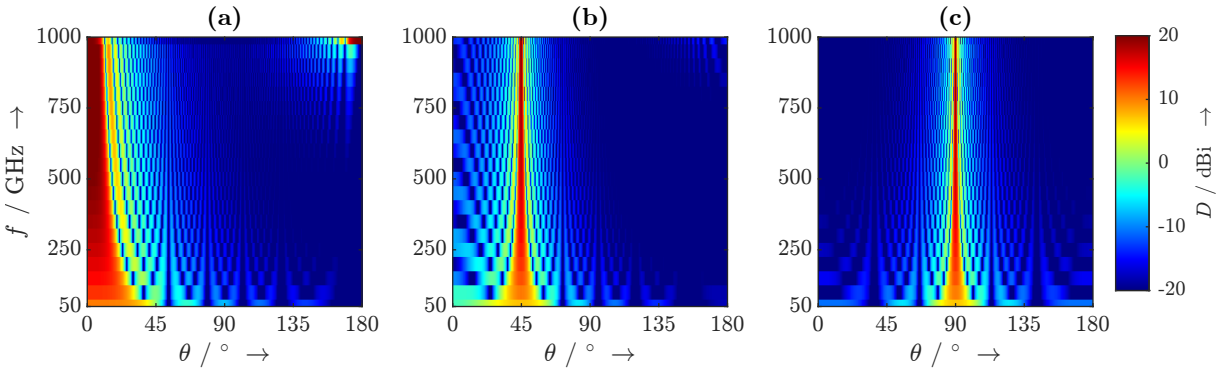

Figure 6.7: Calculated radiation pattern of a uniformly spaced linear 100-element array of isotropic radiators with the element spacing $d = 0.15\,\text{mm}$. The beam is steered in the directions **(a)** $\theta_0 = 0°$, **(b)** $\theta_0 = 45°$, and **(c)** $\theta_0 = 90°$, respectively, using the QTTD approach for $F = 50\,\text{GHz}$. The radiation patterns are plotted only at the frequencies $f = m \cdot 50\,\text{GHz}$.

To visualize the effects of the *quasi*-true time delays, Figure 6.6 shows the radiation patterns plotted with a frequency resolution of 1 GHz, and Figure 6.7 shows the radiation patterns only at the frequencies $f = m \cdot 50\,\text{GHz}$.

The cases $\theta_0 = 0°$ and $\theta_0 = 45°$ in Figure 6.6 illustrate that the main lobe is at the correct angles for $f = m \cdot 50\,\text{GHz}$ and squints away from these angles between those frequencies. By only showing those frequencies, Figure 6.7 highlights that the beam shows the proper shape at the frequencies $f = mF$.

6.3 Spatial element distributions for UHRR-THz-TDS

As discussed in Section 6.1.3, the optimum element spacing of a uniformly spaced antenna array depends on the operating frequency. This is a problem for beam steering in a wideband UHRR-THz-TDS system, as a small element spacing leads to low directivity at the lower frequencies, whereas a large element spacing leads to grating lobes at the higher frequencies. A promising solution is a well-chosen non-uniform spatial element distribution. By breaking the periodicity of the array, the condition for perfect constructive interference can be made to possess only a single exact solution, so that true grating lobes are avoided while maintaining a high directivity of the main lobe. However, depending on the chosen element distribution, the radiation pattern can still exhibit side lobes with varying amplitudes.

In the following, two different solutions for striking a compromise between directivity and side lobe suppression over the considered frequency range from 50 to 1000 GHz are presented. In Section 6.3.1, the use of a zero-redundancy element distribution based on a Golomb ruler is demonstrated. In Section 6.3.2, different numerically optimized element distributions are shown.

All radiation patterns shown on the following pages are calculated using Equation (6.5) with the array factor

$$g(\theta, f = mF) = \sum_{n=1}^{10} \exp\left[\mathrm{j} \cdot 2\pi \cdot mF \cdot \left(\frac{z_n \cdot \cos\theta}{c_0} - \frac{z_n \cdot \cos\theta_0}{c_0} \bmod \frac{1}{F}\right)\right] \tag{6.45}$$

for $F = 50\,\mathrm{GHz}$.

6.3.1 Zero-redundancy spatial element distribution

As the name suggests, grating lobes result from the periodic nature of an antenna array. More precisely, a main lobe or grating lobe appears when multiple pairs of antennas share the same interference maximum. This is naturally the case in an array of equidistantly spaced antennas. Intuitively, this means that grating lobes can be suppressed if the element distribution is made "as non-uniform as possible" in the form of a so-called *minimum-redundancy* distribution. I have first demonstrated the use of a minimum-redundancy antenna array for UHRR-THz-TDS in Ref. [2] [15]. Reducing

[15] See footnote 14.

redundancy in an antenna array had previously been proposed as a solution for maximizing directivity with a limited number of elements [120–122] as well as for increasing the bandwidth of an array [123, 124].

A promising minimum-redundancy distribution is a *Golomb ruler*. A Golomb ruler is a set of integers that are chosen such that no two pairs of elements within the set have the same difference. The number of elements in the set is called the *order* of the set. To design a linear N-element array, we consider the N^{th}-order Golomb ruler $G_N = \{g_0\,,\, g_1\,,\, \ldots\,,\, g_{N-1}\}$ and choose a minimum element spacing d. The locations of the antennas are then

$$z_n = g_n \cdot d\;,\; n = 0 \ldots N-1\;. \tag{6.46}$$

In the following, the design of a 10-element array is considered. The 10^{th}-order Golomb ruler consists of the elements [125, 126]

$$G_{10} = \{0\,,\, 1\,,\, 6\,,\, 10\,,\, 23\,,\, 26\,,\, 34\,,\, 41\,,\, 53\,,\, 55\}\;. \tag{6.47}$$

To avoid grating lobes up to $f = 1000\,\text{GHz}$ when steering the beam to the broadside direction, the element spacing is chosen to be half a wavelength at that frequency, i.e.

$$d = \frac{c_0}{2 \cdot 1000\,\text{GHz}} \approx 150\,\mu\text{m}\;. \tag{6.48}$$

The resulting element distribution is sketched in Figure 6.8. To analyze the performance of the minimum-redundancy array, the resulting frequency-dependent radiation patterns of a linear 10-element array of isotropic radiators that are arranged according to Equations (6.46) through (6.48) are depicted and evaluated for their key parameters in Figure 6.9. The rows (a), (b), and (c) represent the cases where the beam is steered in the directions $\theta_0 = 0°$, $\theta_0 = 45°$, and $\theta_0 = 90°$, respectively. In conformance with the use for UHRR-THz-TDS, only the frequencies $f = m \cdot 50\,\text{GHz}$ are considered.

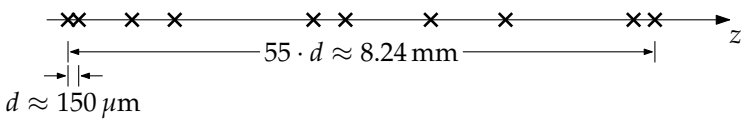

Figure 6.8: Minimum-redundancy element distribution according to a 10^{th}-order Golomb ruler with the minimum element spacing d.

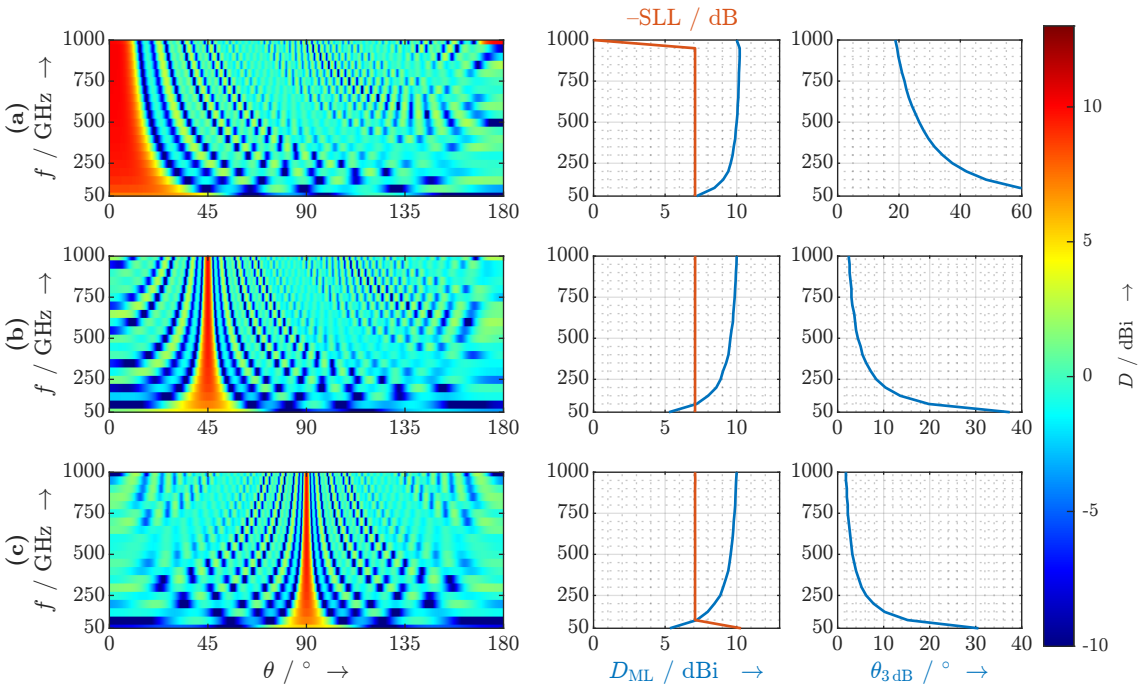

Figure 6.9: Calculated frequency-dependent radiation pattern, main lobe directivity D_{ML}, side lobe level SLL, and beam width $\theta_{3\,\mathrm{dB}}$ of a linear 10-element array of isotropic radiators that are arranged according to a 10^{th}-order Golomb ruler with the minimum spacing $d \approx 150\mu\mathrm{m}$. The beam is steered in the directions **(a)** $\theta_0 = 0°$, **(b)** $\theta_0 = 45°$, and **(c)** $\theta_0 = 90°$, respectively. Only the frequencies $f = m \cdot 50\,\mathrm{GHz}$ are considered.

Comparing the resulting radiation patterns to the corresponding patterns of dense and sparse uniformly-spaced arrays depicted in Figure 6.3, we can see that the minimum-redundancy array achieves a much narrower beam width than the dense uniform array. At the same time, it does not produce any grating lobes across the entire frequency and steering range. Only in the end-fire case at 1000 GHz, a back lobe is produced at $\theta = 180°$. While the minimum-redundancy array does not produce true grating lobes, it does produce several side lobes. Most notably, the side lobe level (SLL) is constant at 7.1 dB across the entire frequency and steering range [16]. The directivity of the main lobe increases monotonically from 5.3 dBi at 50 GHz to 10 dBi at 1000 GHz.

[16] The side lobe level (SLL) is defined as the ratio between the maximum directivity outside the main lobe and the directivity of the main lobe in dB.

In summary, the minimum-redundancy array is well-behaved across the entire considered frequency range and exhibits a remarkably consistent performance throughout the entire range of steering angles. These properties make this element distribution a good choice for applications that utilize the entire frequency range and require fair directivity as well as good angular selectivity.

6.3.2 Numerically optimized spatial element distributions

Since the minimum-redundancy element distribution offers a compromise between all parameters, it is instructive to evaluate whether it is possible to find alternative element distributions that imprint desired characteristics on the frequency-dependent radiation pattern. Based on the experience with numerical optimization for spectral shaping (see Chapter 4), a genetic algorithm has been chosen to be employed for that purpose. In the following, first the formulation of the optimization problem and its constraints are described. Subsequently, fitness functions for three different optimization goals are developed and the respective results are presented.

Formulation and constraints of the optimization problem

The goal of the genetic algorithm is finding the locations z_n , $n = 0 \ldots N-1$, of the elements of a linear 10-element array that minimize the value of a fitness function ξ that is defined as a function of the angle- and frequency-dependent array factor $g(\theta, f)$. Because steering angles close to broadside are practically most relevant, the optimization is simplified by only considering the case $\theta_0 = 90°$. To ensure comparability with the element distributions shown in the previous sections and to prevent the genetic algorithm from generating unfeasible results, it is necessary to enforce constraints on the locations z_n. It is chosen that the spacing between any two elements shall not be less than half a wavelength at 1000 GHz and shall not be larger than half a wavelength at 50 GHz. This places any generated result between the two cases depicted in Figure 6.3. The constraints are practically implemented by allowing the genetic algorithm to choose the distances d_k , $k = 1 \ldots N-1$, between the elements with

$$\frac{c_0}{2 \cdot 1000\,\mathrm{GHz}} \leq d_k \leq \frac{c_0}{2 \cdot 50\,\mathrm{GHz}} \; \forall \, k \tag{6.49}$$

and defining the locations

$$z_n = \sum_{k=1}^{n} d_k \,,\; n = 0 \,...\, N-1 \,. \tag{6.50}$$

The array factor is only considered at the discrete frequencies $m \cdot 50\,\mathrm{GHz}$, $m = 1 \,...\, 20$, for the discrete angles $l \cdot 0.1^\circ$, $l = 0 \,...\, 1800$. The discrete array factor is calculated as

$$\begin{aligned} g[l,m] &= g(l \cdot 0.1^\circ \,,\, m \cdot 50\,\mathrm{GHz}) \\ &= \sum_{n=0}^{9} \exp\left(\mathrm{j} \cdot \frac{2\pi \cdot m \cdot 50\,\mathrm{GHz} \cdot z_n \cdot \cos\left(l \cdot 0.1^\circ\right)}{c_0} \right) . \end{aligned} \tag{6.51}$$

Minimizing the deviation from a hypothetical "ideal" array

The first – admittedly quite heuristic – optimization goal is the minimization of the deviation of the resulting array factor from that of a hypothetical "ideal" array. The fitness function is defined as

$$\xi_{\text{total deviation}} = \sum_{m=1}^{20} \sum_{l=0}^{1800} \left(g[l,m] - g_{\text{ideal}}[l,m] \right)^2 , \tag{6.52}$$

where $g_{\text{ideal}}[l,m]$ is the targeted array factor depicted in Figure 6.10.

It is determined by calculating the array factor of a uniformly spaced 10-element array with an element spacing that is equal to half a wavelength at 50 GHz, and removing all side lobes, i.e.

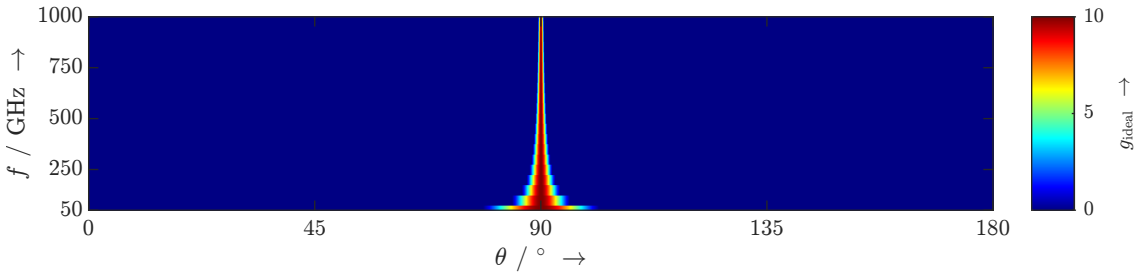

Figure 6.10: Hypothetical side lobe-free array factor of a uniformly spaced 10-element array with an element spacing that is equal to half a wavelength at 50 GHz.

$$g_{\text{ideal}}[l,m] = \begin{cases} \sum_{n=0}^{9} \mathrm{e}^{\mathrm{j}\cdot\pi\cdot m\cdot n\cdot\cos(l\cdot 0.1^\circ)} & , \quad \cos^{-1}\left(\frac{1}{5m}\right) \leq \cos^{-1}\left(-\frac{1}{5m}\right) \\ 0 & , \quad \text{else} \end{cases} . \tag{6.53}$$

The angles $\cos^{-1}\left(\pm\frac{1}{5m}\right)$ are the positions of the first nulls on the left and right of the main lobe. The element distribution generated by the genetic algorithm is sketched in Figure 6.11, and the resulting radiation patterns are depicted in Figure 6.12.

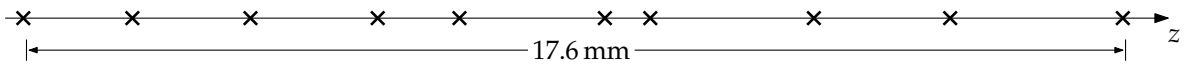

Figure 6.11: Numerically optimized element distribution that minimizes the deviation from a hypothetical "ideal" array.

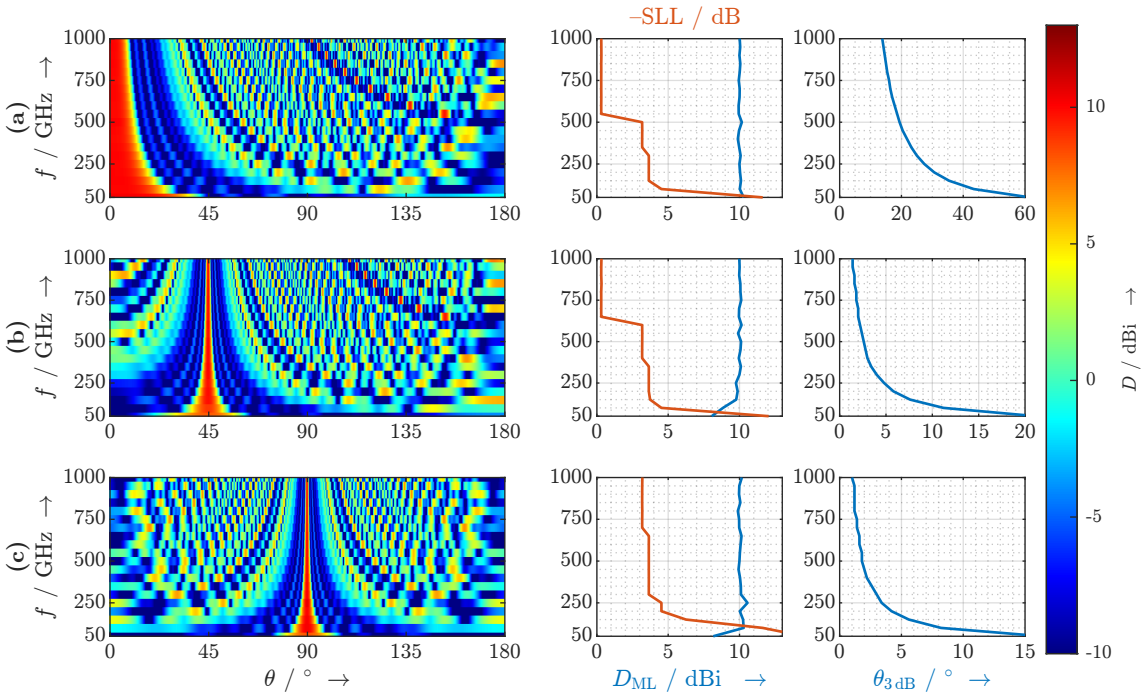

Figure 6.12: Calculated frequency-dependent radiation pattern, main lobe directivity D_{ML}, side lobe level SLL, and beam width $\theta_{3\,\text{dB}}$ of a linear 10-element array of isotropic radiators that are arranged according to the numerically optimized distribution shown in Figure 6.11. The beam is steered in the directions **(a)** $\theta_0 = 0°$, **(b)** $\theta_0 = 45°$, and **(c)** $\theta_0 = 90°$, respectively.

They have the interesting property that the directivity of the main lobe is almost constant at 10 dBi across the entire frequency range for all steering angles. It only drops below that value by any significant amount at 50 GHz. However, the high directivity comes at the cost of an increased side lobe level. In the broadside case depicted in (c), significant side lobes appear for $f \geq 150\,\mathrm{GHz}$ with a level between -4.5 and $-3.2\,\mathrm{dB}$. As the beam is steered away from the broadside direction, "true" grating lobes appear for $f \geq 650\,\mathrm{GHz}$ and $f \geq 550\,\mathrm{GHz}$ in the $\theta_0 = 45^\circ$ and $\theta_0 = 0^\circ$ case, respectively. Notably, the side lobes are located far away from the main lobe across the entire range of frequencies and steering angles, creating a quiet zone around the main lobe. This is quite beneficial in practical applications because it supports good angular selectivity. Moreover, the element pattern of real non-isotropic antennas naturally attenuates radiation off-broadside.

Minimizing the deviation from a mask

Minimizing the total deviation of the array factor of the optimized element distribution from a desired array factor is a quite simple approach. However, we have seen that it is not possible to find a perfect solution because the requirements interfere with each other across the large frequency range. With the approach shown above, there is no means of weighting these conflicting requirements. An alternative approach for defining a fitness function that optimizes practically relevant parameters has recently been proposed by Sheikholeslami and Atlasbaf [127] in the context of re-configurable reflect arrays [17]. They specify a lower and an upper mask for the normalized array factor, and define a fitness function that is minimized if the array factor lies between the lower and upper mask. Using the notation introduced in this section, the value of the fitness function at the normalized frequency m is [127]

$$\begin{aligned}\xi_{\mathrm{mask}}[m] = \sum_{l=0}^{1800} &\left(g_{\mathrm{U}}^2[l,m] - |g_{\mathrm{norm.}}[l,m]|^2\right) \cdot \left(g_{\mathrm{L}}^2[l,m] - |g_{\mathrm{norm.}}[l,m]|^2\right) \\ &+ \left|g_{\mathrm{U}}^2[l,m] - |g_{\mathrm{norm.}}[l,m]|^2\right| \cdot \left|g_{\mathrm{L}}^2[l,m] - |g_{\mathrm{norm.}}[l,m]|^2\right| ,\end{aligned} \tag{6.54}$$

where $g_{\mathrm{L}}[l,m]$ and $g_{\mathrm{U}}[l,m]$ are the lower and the upper mask, respectively, and

[17] I would like to thank M. Sc. Xuan Liu for pointing out Ref. [127] to me.

$$g_{\text{norm.}}[l,m] = \frac{g[l,m]}{\max\limits_{l}\{|g[l,m]|\}} \tag{6.55}$$

is the normalized array factor. The masks are typically specified according to the desired beam width and side lobe level. To enable a comparison with the previous optimization result, masks that match the hypothetical array factor shown in Figure 6.10 are chosen. The lower and upper mask are depicted in Figure 6.13 (a) and (b), respectively. The lower mask represents the 3 dB beamwidth of the hypothetical array, and the upper mask aims to enforce a side lobe level of –13.26 dB. This value is chosen because it represents the minimum side lobe level of an array that is excited with uniform amplitudes.

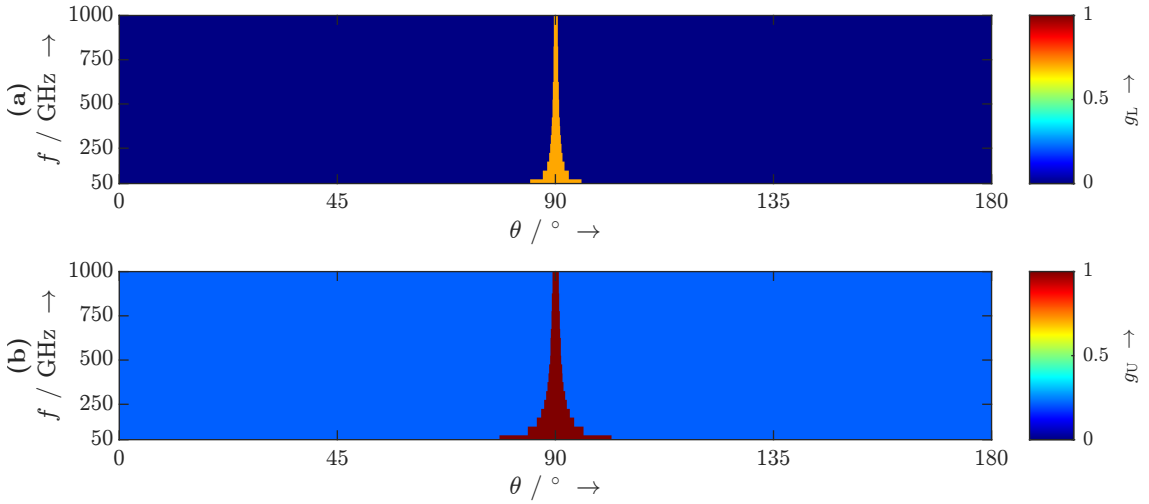

Figure 6.13: (a) Lower and **(b)** upper mask extracted from the array factor in Figure 6.10.

To minimize the deviation from the mask across the entire frequency range, the fitness function

$$\begin{aligned}\xi_{\text{mask, max.}} = \max_{m}\Bigg\{ &\sum_{l=0}^{1800}\left(g_{\text{U}}^2[l,m] - |g_{\text{norm.}}[l,m]|^2\right)\cdot\left(g_{\text{L}}^2[l,m] - |g_{\text{norm.}}[l,m]|^2\right) \\ &+ \left|g_{\text{U}}^2[l,m] - |g_{\text{norm.}}[l,m]|^2\right|\cdot\left|g_{\text{L}}^2[l,m] - |g_{\text{norm.}}[l,m]|^2\right|\Bigg\}\end{aligned} \tag{6.56}$$

is chosen. The element distribution generated by the genetic algorithm is sketched in Figure 6.14, and the resulting radiation patterns are depicted in Figure 6.15.

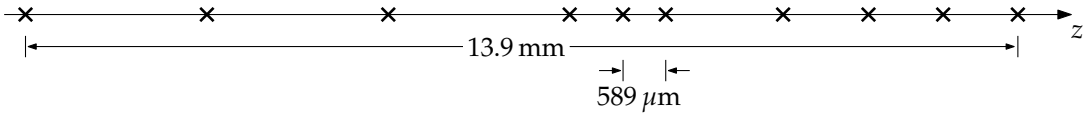

Figure 6.14: Numerically optimized element distribution that minimizes the deviation from the mask depicted in Figure 6.13.

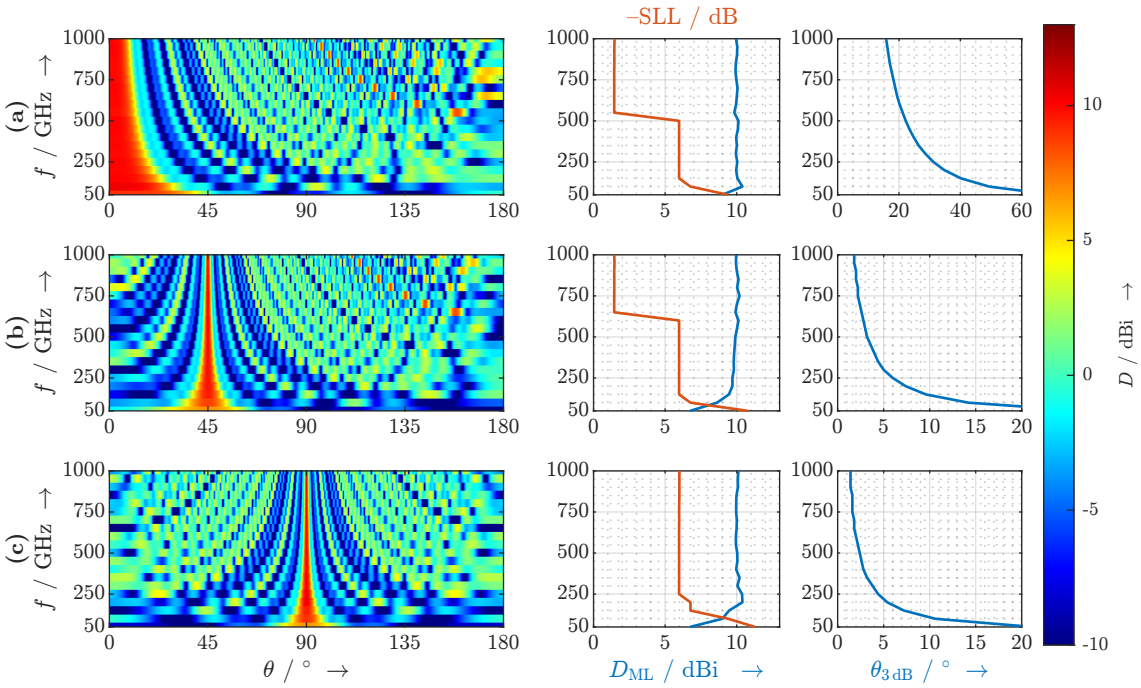

Figure 6.15: Calculated frequency-dependent radiation pattern, main lobe directivity D_{ML}, side lobe level SLL, and beam width $\theta_{3\,\mathrm{dB}}$ of a linear 10-element array of isotropic radiators that are arranged according to the numerically optimized distribution shown in Figure 6.14. The beam is steered in the directions **(a)** $\theta_0 = 0°$, **(b)** $\theta_0 = 45°$, and **(c)** $\theta_0 = 90°$, respectively. Only the frequencies $f = m \cdot 50\,\mathrm{GHz}$ are considered.

In the broadside case, the directivity has the value 6.7 dBi at 50 GHz and rapidly increases to around 10 dBi for frequencies above 150 GHz. The side lobe level is constant at -6 dB for frequencies above 250 GHz. Compared to the case depicted in Figure 6.12, this optimization goal has achieved an improvement of the side lobe level by up to 3 dB at the cost of a slightly decreased directivity at the lower end of the frequency range.

Minimizing the maximum side lobe level

The effective angular selectivity that can be achieved with the antenna array is largely determined by the prominence of the main lobe, i.e. the ratio between the directivity of the main lobe and the maximum directivity outside the main lobe. This ratio is in fact quantified by the side lobe level. Since the side lobe level is in general frequency-dependent, an important optimization goal is the minimization of the maximum side lobe ratio in the observed frequency range. For that purpose, the fitness function

$$\xi_{\mathrm{SLL}} = \left(\min_{m} \left\{ \frac{g_{\mathrm{ML}}[m]}{g_{\mathrm{SL}}[m]} \right\} \right)^{-1} \tag{6.57}$$

has been defined, where

$$g_{\mathrm{ML}}[m] = g[900, m] \tag{6.58}$$

is the value of the array factor of the main lobe at the frequency $m \cdot 50\,\mathrm{GHz}$ and

$$g_{\mathrm{SL}}[m] = \max_{l} \left\{ g[l, m] \;,\; l < l_{\mathrm{left}} \vee l > l_{\mathrm{right}} \right\} \tag{6.59}$$

is the maximum directivity outside the main lobe at the same frequency. The indices l_{left} and l_{right} denote the left and right borders of the main lobe. These are determined by finding the nearest local minima of the array factor on the left and right of the main lobe. Rather than defining a fixed angular range for the main lobe *a priori*, this method adapts the limits l_{left} and l_{right} to the actual width of the main lobe for each individual that is generated by the genetic algorithm.

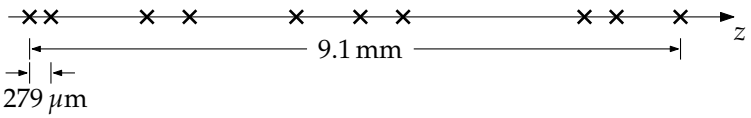

Figure 6.16: Numerically optimized element distribution that minimizes the side lobe level across the entire frequency range.

The element distribution generated by the genetic algorithm is sketched in Figure 6.16, and the resulting radiation patterns are depicted in Figure 6.17. Looking at the resulting radiation patterns and the parameters extracted therefrom, there is great similarity with the minimum-redundancy array. There are no grating lobes in the broadside

case, and the side lobe level is constant at 7.1 dB. The directivity increases from 5.6 dB at 50 GHz to 10.26 dB at 1000 GHz. As the beam is steered off-broadside, a grating lobe appears for frequencies above 650 GHz. These results are a strong indication that the element distribution according to a Golomb ruler shown in the previous section is in fact the optimum solution for minimizing the side lobe level across the considered range of frequencies and steering angles.

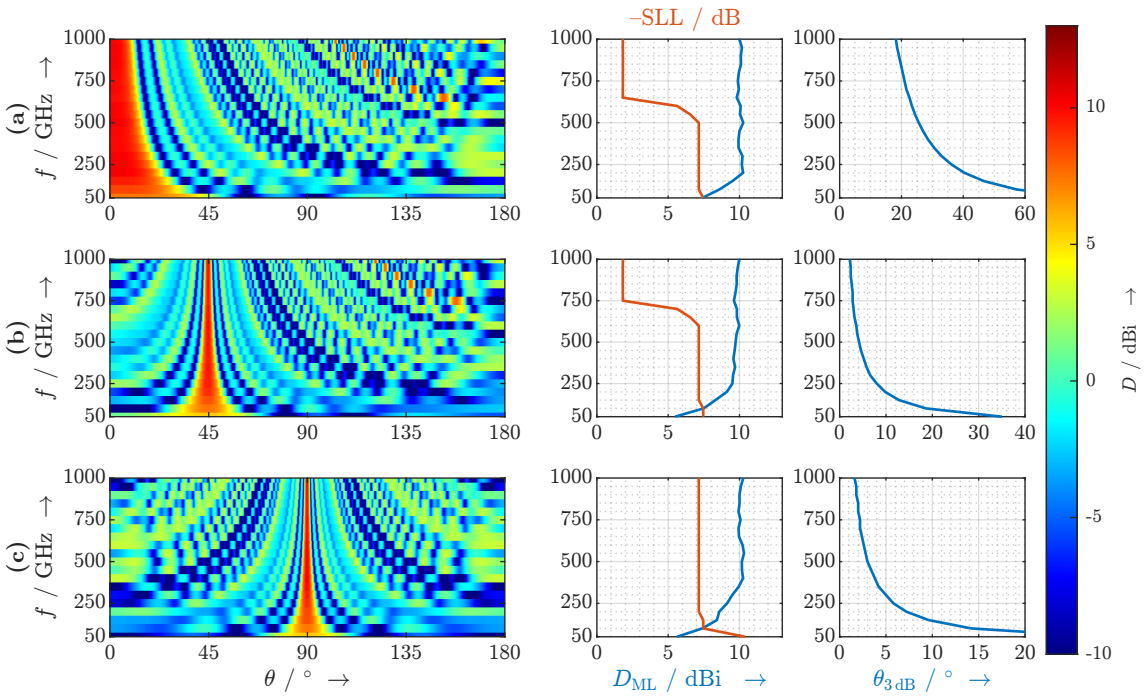

Figure 6.17: Calculated frequency-dependent radiation pattern, main lobe directivity D_{ML}, side lobe level SLL, and beam width $\theta_{3\,\mathrm{dB}}$ of a linear 10-element array of isotropic radiators that are arranged according to the numerically optimized distribution shown in Figure 6.16. The beam is steered in the directions **(a)** $\theta_0 = 0°$, **(b)** $\theta_0 = 45°$, and **(c)** $\theta_0 = 90°$, respectively. Only the frequencies $f = m \cdot 50\,\mathrm{GHz}$ are considered.

CONCLUSION AND OUTLOOK

Conclusion

This thesis provides a comprehensive treatment of UHRR-THz-TDS. Starting from a recapitulation of the development of photonic terahertz spectroscopy systems, it is shown that MLLDs are currently competing with MMLDs and SLDs as monolithic light sources that are suitable for THz-TDS. The main property setting them apart is their effective coherence length. Due to the locking of the laser modes, MLLDs exhibit a long effective coherence length that give UHRR-THz-TDS properties similar to "classical" THz-TDS. On the other hand, MMLDs and SLDs emit light that has a very short effective coherence length or virtually no coherence, respectively, so that the associated THz-CCS approach behaves quite differently from UHRR-THz-TDS.

Based on this consideration, advantages and disadvantages of the concepts for different applications and systems are established. On the one hand, a long effective coherence length is beneficial in applications in which the round-trip time of the terahertz signal is not known *a priori* or changes with time. These applications most prominently include SAR imaging. On the other hand, the fixed phase relationship between the laser modes of an MLLD demands the optical pulse to be properly compressed at the terahertz emitter and detector. Therefore, the required precisely defined length of fiber between the MLLD and the emitter-detector pair puts an – admittedly generous – limit on the total distance between the light source and the terahertz system. More importantly, the required pulse compression is yet another hurdle on the way towards a completely monolithically integrated terahertz spectroscopy system. A particular em-

phasis of this work is on the effects of the ultra-high repetition rate of MLLDs. While causing a poor spectral resolution for spectroscopic applications, its effects on SAR imaging are a little more nuanced. On the one hand, it causes the unambiguous range to be extremely short. On the other hand, it provides a deep field of view, as the range in which objects can be detected no longer depends on the length of the ODU. MLLD- and SLD-driven systems are strikingly complementary. While the former are preferable for imaging due to their deep field of view, the latter are preferable for spectroscopic applications given their high spectral resolution.

An important contribution of this work is the development of a system-theoretical model for UHRR-THz-TDS. The presented model allows to calculate the detected terahertz spectrum from the complex optical spectrum and the complex transfer function of the terahertz system. Moreover, it establishes the relationship between the complex optical spectrum, the intensity autocorrelation, and the detected terahertz spectrum. The model shows that the spectrum of the MLLD only affects the amplitudes but not the phases of the detected terahertz spectrum. It also shows that the corresponding amplitude factors can be calculated either from the amplitude and phase spectrum of the MLLD or from the Fourier transform of the intensity autocorrelation function.

These results have great practical relevance. Firstly, they explain the importance of pulse compression and quantify the effect of pulse chirp on the emitted as well as the detected terahertz spectrum. Secondly, they allow a prediction of the MLLD's performance in an UHRR-THz-TDS system based on its optical spectrum. An interesting result of this analysis is that for a constant average optical power, the emitted and detected spectral amplitudes increase with the number of laser modes. Consequentially, an MLLD with a wide and dense optical spectrum generates the highest spectral amplitudes. As a byproduct, this analysis shows that the transmitter of a terahertz-photonic communication system exhibits a higher transmit power if it is driven by an MLLD compared to the conventional case where it is driven by two single-mode lasers.

Based on the improved understanding of UHRR-THz-TDS, several improvements of the concept are devised and solutions for existing problems of wideband terahertz systems are developed. Making use of the system-theoretical model, a concept for shaping the detected terahertz spectrum by shaping the spectrum of the MLLD is investigated. It is shown that a genetic algorithm can be used to synthesize the complex optical spectrum that is required to generate a desired terahertz spectrum. Fitness functions for the

genetic algorithm that maximize the total detected power, a particular spectral component, or the bandwidth of the detected spectrum are developed. First experimental results using a programmable optical filter show that a spectral shape that maximizes the detected bandwidth leads to an improvement of the spectral components above 1 THz by up to 8 dB.

To further enhance the performance and practicality of UHRR-THz-TDS, a novel technique for correcting errors caused by the ODU in the system is developed. This new technique uses the light from the MLLD in a Mach-Zehnder interferometer to generate a reference signal for synchronizing and correcting the delay axis. It has numerous advantages over previously used approaches. Firstly, it increases the hardware effort of the system only by a minimal amount and facilitates the data acquisition by providing a low-noise trigger signal. Secondly, it provides absolute time synchronization and corrects non-linearities of the delay axis with femtosecond-accuracy using a simple algorithm. This can prospectively allow the use of a fast free-running ODU for achieving a high spectral update rate. Thirdly, the demonstrated concept allows the detected terahertz signal to be trimmed to exactly one period. This step allows an accurate discrete Fourier transform and efficient processing of the measurement data.

Finally, beam steering for UHRR-THz-TDS is addressed. To that end, some of the fundamental challenges of beam steering for a wideband terahertz system are discussed and solutions that make use of the frequency-discrete spectrum generated by the MLLD are presented. It is reasoned – based on a simple power budget analysis – that photonic beam steering is the most useful approach for UHRR-THz-TDS. It is then mathematically shown that a delay range equal to one repetition period of the MLLD is sufficient to enable beam steering across the entire frequency range of the system without beam squint. This approach is named *quasi*-true time delay beam steering. Based on this approach, it is then demonstrated with numerical simulations that non-uniform spatial element distributions of a linear antenna array with a limited number of array elements can achieve a high directivity without grating lobes. On the one hand, numerically optimized element distributions that aim to match the radiation pattern of the array to that of a hypothetical “ideal” array or minimize the side lobe level are developed. On the other hand, it is shown that a minimum-redundancy element distribution according to a Golomb ruler in fact realizes the best side lobe level across the entire frequency range for all steering angles between broadside and end-fire.

Outlook

This thesis opens up several paths for future work. First and foremost, the presented description and analytical modeling of UHRR-THz-TDS will be of great benefit to the interpretation of future experimental results. In order to make less restrictive assumptions about the light source, it will be of great interest to develop a more general stochastic model of the system. Such a stochastic model should be formulated in a way that the detected terahertz spectrum can be calculated for arbitrary optical spectra. Not only would such a description allow for a more accurate quantitative comparison between different light sources, but it would also make it possible to quantify the effect of the finite linewidth of real MLLDs.

The proposed approach for spectral shaping leaves plenty of room for future work. A technique that can be expected to deliver improved results will be to include the transfer function of the terahertz system in the model-driven optimization procedure and to follow this up with measurement-driven iteration cycles. Moreover, it will be of great interest to determine customized optimization goals for specific applications. In the long run, it may be viable to consider these results in the design of new MLLDs that are optimized for UHRR-THz-TDS.

The presented method for the interferometric reconstruction of the delay axis will be of great practical relevance. Because its benefits greatly outweigh the additional hardware effort, it should be used in all future UHRR-THz-TDS measurements. Beyond that, attempts should be made to construct a fast ODU with a delay range that matches the repetition rate of the MLLD and to combine this with a fast data acquisition device. Such a system will be an important step towards making the UHRR-THz-TDS approach commercially attractive. In the same context, the possible applications of UHRR-THz-TDS should be further investigated. Particular attention should be paid to applications that make use of the deep field of view. On the other hand, effort should be spent on developing methods for resolving the problem of ambiguity. A promising solution may be a sensor fusion approach that combines the data from the UHRR-THz-TDS system with that from another sensor. While the UHRR-THz-TDS system provides a high resolution, the other sensor (for example an electronic terahertz radar) determines the “rough” location of the object under test to resolve the ambiguity.

Finally, the presented concepts for wideband beam steering still require experimental validation. This will be a massive undertaking due to the technological challenges involved in the realization of an on-chip array of antenna-integrated photodiodes and the photonic beam steering network. A likely first step that will enable a proof of concept will be the construction of a small on-chip array that is driven by a fiber-optic beam steering network. Besides the experimental proof of concept, there are several more areas that deserve further investigation. One of them is the antenna structure. An important research question is the development of antenna structures that efficiently radiate over an extremely wide frequency range but are small enough to be used in an array. In that context, mutual coupling between the array elements and efficient coupling into free space will be important aspects to consider. In the spirit of this thesis, it should be evaluated if the frequency-discrete nature of the wideband radiated signals can be exploited in the design of the antenna structures. On the side of the beam steering network, the realization of fast tunable delay elements will be of utmost importance. Currently, the most promising approach is a switched delay line. The underlying technological challenge of the proposed concepts will be the hetero-integration of the passive beam steering network, the antenna-integrated photodiodes, and optical amplifiers. However, it can be expected that the synergy with current research on sixth-generation wireless communication systems operating at terahertz frequencies will deliver solutions within a few years.

LIST OF ABBREVIATIONS

3D	three-dimensional
ASOPS	asynchronous optical sampling
Be	beryllium
COC	cyclic olefin copolymer
CPM	colliding pulse mode locking
DBR	distributed Bragg reflector
DFB	distributed feedback
DFT	discrete Fourier transform
DSO	digital storage oscilloscope
ECOPS	electronically controlled optical sampling
ELF	extremely low frequency
ErAs	erbium arsenide
Fe	iron
FMCW	frequency-modulated continuous-wave
FSR	free spectral range
FWHM	full width at half maximum
GaAs	gallium arsenide

HHI	Heinrich Hertz Institute
InAlAs	indium aluminum arsenide
InGaAs	indium gallium arsenide
InGaAsP	indium gallium arsenide phosphide
LTG	low-temperature-grown
MBE	molecular beam epitaxy
MLHS	multilayer heterostructure
MLL	mode-locked laser
MLLD	mode-locked laser diode
MMLD	multi-mode laser diode
MOCVD	metal-organic chemical vapor deposition
MQW	multiple quantum well
ODU	optical delay unit
OSA	optical spectrum analyzer
OSCAT	optical sampling by laser cavity tuning
PAPR	peak-to-average power ratio
PBS	polarization beam splitter
PC	polarization controller
PCA	photoconductive antenna
PM	polarization maintaining
QD	quantum dot
QDash	quantum dash
QTDS	quasi time-domain spectroscopy
QTTD	quasi-true time delay
RF	radio frequency

Rx	receiver
SAR	synthetic aperture radar
SHG	second harmonic generation
SLAPCOPS	single-laser polarization-controlled optical sampling
SLD	superluminescent diode
SLL	side lobe level
SOS	silicon on sapphire
THz-CCS	terahertz cross-correlation spectroscopy
THz-FDS	terahertz frequency-domain spectroscopy
THz-TDS	terahertz time-domain spectroscopy
Ti:sapphire, Ti:Al_2O_3	titanium-sapphire
TIA	transimpedance amplifier
TPX	polymethylpentene
TTD	true time delay
Tx	transmitter
UHRR-THz-TDS	ultra-high repetition rate terahertz time-domain spectroscopy

REFERENCES

[36] P. Jepsen, D. Cooke, and M. Koch, "Terahertz spectroscopy and imaging – modern techniques and applications," *Laser & Photonics Reviews*, vol. 5, no. 1, pp. 124–166, 2011. doi: 10.1002/lpor.201000011

[37] J. D. Jackson, "Classical electrodynamics," New York, 1999.

[38] G. Mouret, S. Matton, R. Bocquet, D. Bigourd, F. Hindle, A. Cuisset, J. F. Lampin, and D. Lippens, "Anomalous dispersion measurement in terahertz frequency region by photomixing," *Applied Physics Letters*, vol. 88, no. 18, p. 181105, 2006. doi: 10.1063/1.2200393

[39] G. Mouret, S. Matton, R. Bocquet, D. Bigourd, F. Hindle, A. Cuisset, J. F. Lampin, K. Blary, and D. Lippens, "Thz media characterization by means of coherent homodyne detection, results and potential applications," *Applied Physics B*, vol. 89, no. 2, pp. 395–399, Nov 2007. doi: 10.1007/s00340-007-2785-5

[40] A. Roggenbuck, K. Thirunavukkuarasu, H. Schmitz, J. Marx, A. Deninger, I. C. Mayorga, R. Güsten, J. Hemberger, and M. Grüninger, "Using a fiber stretcher as a fast phase modulator in a continuous wave terahertz spectrometer," *J. Opt. Soc. Am. B*, vol. 29, no. 4, pp. 614–620, Apr 2012. doi: 10.1364/JOSAB.29.000614

[41] A. M. Sinyukov, Z. Liu, Y. L. Hor, K. Su, R. B. Barat, D. E. Gary, Z.-H. Michalopoulou, I. Zorych, J. F. Federici, and D. Zimdars, "Rapid-phase modulation of terahertz radiation for high-speed terahertz imaging and spectroscopy," *Opt. Lett.*, vol. 33, no. 14, pp. 1593–1595, Jul 2008. doi: 10.1364/OL.33.001593

[42] A. Roggenbuck, H. Schmitz, A. Deninger, I. C. Mayorga, J. Hemberger, R. Güsten, and M. Grüninger, "Coherent broadband continuous-wave terahertz spectroscopy on solid-state samples," *New Journal of Physics*, vol. 12, no. 4, p. 043017, apr 2010. doi: 10.1088/1367-2630/12/4/043017

[43] S. Hisatake, J.-Y. Kim, K. Ajito, and T. Nagatsuma, "Self-heterodyne spectrometer using uni-traveling-carrier photodiodes for terahertz-wave generators and optoelectronic mixers," *Journal of Lightwave Technology*, vol. 32, no. 20, pp. 3683–3689, 2014. doi: 10.1109/JLT.2014.2321004

[44] S. Hisatake, Y. Koda, R. Nakamura, N. Hamada, and T. Nagatsuma, "Terahertz balanced self-heterodyne spectrometer with snr-limited phase-measurement sensitivity," *Opt. Express*, vol. 23, no. 20, pp. 26 689–26 695, Oct 2015. doi: 10.1364/OE.23.026689

[45] I.-M. Lee, N. Kim, E. S. Lee, S.-P. Han, K. Moon, and K. H. Park, "Frequency modulation based continuous-wave terahertz homodyne system," *Opt. Express*, vol. 23, no. 2, pp. 846–858, Jan 2015. doi: 10.1364/OE.23.000846

[46] L. Liebermeister, S. Nellen, R. B. Kohlhaas, S. Lauck, M. Deumer, S. Breuer, M. Schell, and B. Globisch, "Optoelectronic frequency-modulated continuous-wave terahertz spectroscopy with 4 thz bandwidth," *Nature Communications*, vol. 12, no. 1, p. 1071, Feb 2021. doi: 10.1038/s41467-021-21260-x

[47] E. R. Brown, K. A. McIntosh, K. B. Nichols, and C. L. Dennis, "Photomixing up to 3.8 thz in low-temperature-grown gaas," *Applied Physics Letters*, vol. 66, no. 3, pp. 285–287, 1995. doi: 10.1063/1.113519

[48] K. A. McIntosh, E. R. Brown, K. B. Nichols, O. B. McMahon, W. F. DiNatale, and T. M. Lyszczarz, "Terahertz photomixing with diode lasers in low-temperature-grown gaas," *Applied Physics Letters*, vol. 67, no. 26, pp. 3844–3846, 1995. doi: 10.1063/1.115292

[49] S. Verghese, K. A. McIntosh, S. Calawa, W. F. Dinatale, E. K. Duerr, and K. A. Molvar, "Generation and detection of coherent terahertz waves using two photomixers," *Applied Physics Letters*, vol. 73, no. 26, pp. 3824–3826, 1998. doi: 10.1063/1.122906

[50] K. J. Siebert, H. Quast, R. Leonhardt, T. Löffler, M. Thomson, T. Bauer, H. G. Roskos, and S. Czasch, "Continuous-wave all-optoelectronic terahertz imaging," *Applied Physics Letters*, vol. 80, no. 16, pp. 3003–3005, 2002. doi: 10.1063/1.1469679

[51] I. S. Gregory, W. R. Tribe, C. Baker, B. E. Cole, M. J. Evans, L. Spencer, M. Pepper, and M. Missous, "Continuous-wave terahertz system with a 60 db dynamic range," *Applied Physics Letters*, vol. 86, no. 20, p. 204104, 2005. doi: 10.1063/1.1935032

[52] R. Mendis, C. Sydlo, J. Sigmund, M. Feiginov, P. Meissner, and H. L. Hartnagel, "Coherent generation and detection of continuous terahertz waves using two photomixers driven by laser diodes," *International Journal of Infrared and Millimeter Waves*, vol. 26, no. 2, pp. 201–207, Feb 2005. doi: 10.1007/s10762-005-3000-6

[53] R. Wilk, A. Klehr, M. Mikulics, T. Hasek, M. Walther, and M. Koch, "Terahertz generation with 1064 nm dfb laser diode," *Electronics Letters*, vol. 43, pp. 108–110(2), January 2007. doi: 10.1049/el:20073415

[54] D. Stanze, H.-G. Bach, R. Kunkel, D. Schmidt, H. Roehle, M. Schlak, M. Schell, and B. Sartorius, "Coherent cw terahertz systems employing photodiode emitters," in *2009 34th International Conference on Infrared, Millimeter, and Terahertz Waves*, 2009. doi: 10.1109/ICIMW.2009.5324653

[55] D. Stanze, A. Deninger, A. Roggenbuck, S. Schindler, M. Schlak, and B. Sartorius, "Compact cw terahertz spectrometer pumped at 1.5 μm wavelength," *Journal of Infrared, Millimeter, and Terahertz Waves*, vol. 32, no. 2, pp. 225–232, Feb 2011. doi: 10.1007/s10762-010-9751-8

[56] N. Kim, S.-P. Han, H. Ko, Y. A. Leem, H.-C. Ryu, C. W. Lee, D. Lee, M. Y. Jeon, S. K. Noh, and K. H. Park, "Tunable continuous-wave terahertz generation/detection with compact 1.55 μm detuned dual-mode laser diode and ingaas based photomixer," *Opt. Express*, vol. 19, no. 16, pp. 15 397–15 403, Aug 2011. doi: 10.1364/OE.19.015397

[57] T. Göbel, D. Stanze, B. Globisch, R. J. B. Dietz, H. Roehle, and M. Schell, "Telecom technology based continuous wave terahertz photomixing system with 105 decibel signal-to-noise ratio and 3.5 terahertz bandwidth," *Opt. Lett.*, vol. 38, no. 20, pp. 4197–4199, Oct 2013. doi: 10.1364/OL.38.004197

[58] L. Duvillaret, F. Garet, J.-F. Roux, and J.-L. Coutaz, "Analytical modeling and optimization of terahertz time-domain spectroscopy experiments, using photoswitches as antennas," *IEEE Journal of Selected Topics in Quantum Electronics*, vol. 7, no. 4, pp. 615–623, 2001. doi: 10.1109/2944.974233

[59] E. Ippen, C. Shank, and A. Dienes, "Passive mode locking of the cw dye laser," *Applied Physics Letters*, vol. 21, no. 8, pp. 348–350, 1972. doi: 10.1063/1.1654406

[60] C. V. Shank and E. P. Ippen, *Mode-Locking of Dye Lasers*. Berlin, Heidelberg: Springer Berlin Heidelberg, 1973, pp. 121–143. ISBN 978-3-662-11579-4

[61] R. L. Fork, B. I. Greene, and C. V. Shank, "Generation of optical pulses shorter than 0.1 psec by colliding pulse mode locking," *Applied Physics Letters*, vol. 38, no. 9, pp. 671–672, 1981. doi: 10.1063/1.92500

[62] G. Mourou, C. V. Stancampiano, A. Antonetti, and A. Orszag, "Picosecond microwave pulses generated with a subpicosecond laser-driven semiconductor switch," *Applied Physics Letters*, vol. 39, no. 4, pp. 295–296, 1981. doi: 10.1063/1.92719

[63] D. H. Auston, K. P. Cheung, and P. R. Smith, "Picosecond photoconducting hertzian dipoles," *Applied Physics Letters*, vol. 45, no. 3, pp. 284–286, 1984. doi: 10.1063/1.95174

[64] C. Fattinger and D. Grischkowsky, "Point source terahertz optics," *Applied Physics Letters*, vol. 53, no. 16, pp. 1480–1482, 1988. doi: 10.1063/1.99971

[65] ——, "Terahertz beams," *Applied Physics Letters*, vol. 54, no. 6, pp. 490–492, 1989. doi: 10.1063/1.100958

[66] S. Gupta, J. Whitaker, and G. Mourou, "Ultrafast carrier dynamics in iii-v semiconductors grown by molecular-beam epitaxy at very low substrate temperatures," *IEEE Journal of Quantum Electronics*, vol. 28, no. 10, pp. 2464–2472, 1992. doi: 10.1109/3.159553

[67] S. Gupta, J. F. Whitaker, S. L. Williamson, G. A. Mourou, L. Lester, K. C. Hwang, P. Ho, J. Mazurowski, and J. M. Ballingall, "High-speed photodetector applications of gaas and in$_x$ga$_{1-x}$as/gaas grown by low-temperature molecular beam

epitaxy," *Journal of Electronic Materials*, vol. 22, no. 12, pp. 1449–1455, Dec 1993. doi: 10.1007/BF02649997

[68] J. Kafka, M. Watts, and J.-W. Pieterse, "Picosecond and femtosecond pulse generation in a regeneratively mode-locked ti:sapphire laser," *IEEE Journal of Quantum Electronics*, vol. 28, no. 10, pp. 2151–2162, 1992. doi: 10.1109/3.159524

[69] R. Takahashi, Y. Kawamura, T. Kagawa, and H. Iwamura, "Ultrafast 1.55μm photoresponses in low-temperature-grown ingaas/inalas quantum wells," *Applied Physics Letters*, vol. 65, no. 14, pp. 1790–1792, 1994. doi: 10.1063/1.112870

[70] M. Suzuki and M. Tonouchi, "Fe-implanted ingaas photoconductive terahertz detectors triggered by 1.56μm femtosecond optical pulses," *Applied Physics Letters*, vol. 86, no. 16, p. 163504, 2005. doi: 10.1063/1.1901817

[71] ——, "Fe-implanted ingaas terahertz emitters for 1.56μm wavelength excitation," *Applied Physics Letters*, vol. 86, no. 5, p. 051104, 2005. doi: 10.1063/1.1861495

[72] A. Takazato, M. Kamakura, T. Matsui, J. Kitagawa, and Y. Kadoya, "Terahertz wave emission and detection using photoconductive antennas made on low-temperature-grown ingaas with 1.56μm pulse excitation," *Applied Physics Letters*, vol. 91, no. 1, p. 011102, 2007. doi: 10.1063/1.2754370

[73] B. Sartorius, H. Roehle, H. Künzel, J. Böttcher, M. Schlak, D. Stanze, H. Venghaus, and M. Schell, "All-fiber terahertz time-domain spectrometer operating at 1.5 µm telecom wavelengths," *Opt. Express*, vol. 16, no. 13, pp. 9565–9570, Jun 2008. doi: 10.1364/OE.16.009565

[74] H. Roehle, R. J. B. Dietz, H. J. Hensel, J. Böttcher, H. Künzel, D. Stanze, M. Schell, and B. Sartorius, "Next generation 1.5 µm terahertz antennas: mesa-structuring of ingaas/inalas photoconductive layers," *Opt. Express*, vol. 18, no. 3, pp. 2296–2301, Feb 2010. doi: 10.1364/OE.18.002296

[75] C. D. Wood, O. Hatem, J. E. Cunningham, E. H. Linfield, A. G. Davies, P. J. Cannard, M. J. Robertson, and D. G. Moodie, "Terahertz emission from metal-organic chemical vapor deposition grown fe:ingaas using 830 nm to 1.55 μm excitation," *Applied Physics Letters*, vol. 96, no. 19, p. 194104, 2010. doi: 10.1063/1.3427191

[76] R. J. B. Dietz, B. Globisch, M. Gerhard, A. Velauthapillai, D. Stanze, H. Roehle, M. Koch, T. Göbel, and M. Schell, "64 μw pulsed terahertz emission from growth optimized ingaas/inalas heterostructures with separated photoconductive and trapping regions," *Applied Physics Letters*, vol. 103, no. 6, p. 061103, 2013. doi: 10.1063/1.4817797

[77] R. J. Dietz, B. Globisch, H. Roehle, D. Stanze, T. Göbel, and M. Schell, "Influence and adjustment of carrier lifetimes in ingaas/inalas photoconductive pulsed terahertz detectors: 6 thz bandwidth and 90db dynamic range," *Opt. Express*, vol. 22, no. 16, pp. 19 411–19 422, Aug 2014. doi: 10.1364/OE.22.019411

[78] B. Globisch, R. J. B. Dietz, R. B. Kohlhaas, T. Göbel, M. Schell, D. Alcer, M. Semtsiv, and W. T. Masselink, "Iron doped ingaas: Competitive thz emitters and detectors fabricated from the same photoconductor," *Journal of Applied Physics*, vol. 121, no. 5, p. 053102, 2017. doi: 10.1063/1.4975039

[79] R. B. Kohlhaas, L. Liebermeister, S. Breuer, M. Amberg, D. d. Felipe, S. Nellen, M. Schell, and B. Globisch, "Fiber coupled transceiver with 6.5 thz bandwidth for terahertz time-domain spectroscopy in reflection geometry," *Sensors*, vol. 20, no. 9, 2020. doi: 10.3390/s20092616

[80] R. B. Kohlhaas, R. J. B. Dietz, S. Breuer, S. Nellen, L. Liebermeister, M. Schell, and B. Globisch, "Improving the dynamic range of ingaas-based thz detectors by localized beryllium doping: up to 70 db at 3 thz," *Opt. Lett.*, vol. 43, no. 21, pp. 5423–5426, Nov 2018. doi: 10.1364/OL.43.005423

[81] A. Mingardi, W.-D. Zhang, E. R. Brown, A. D. Feldman, T. E. Harvey, and R. P. Mirin, "High power generation of thz from 1550-nm photoconductive emitters," *Opt. Express*, vol. 26, no. 11, pp. 14 472–14 478, May 2018. doi: 10.1364/OE.26.014472

[82] U. Nandi, J. C. Norman, A. C. Gossard, H. Lu, and S. Preu, "1550-nm driven eras:in(al)gaas photoconductor-based terahertz time domain system with 6.5 thz bandwidth," *Journal of Infrared, Millimeter, and Terahertz Waves*, vol. 39, no. 4, pp. 340–348, Apr 2018. doi: 10.1007/s10762-018-0471-9

[83] C. Janke, M. Först, M. Nagel, H. Kurz, and A. Bartels, "Asynchronous optical sampling for high-speed characterization of integrated resonant terahertz sensors,"

Opt. Lett., vol. 30, no. 11, pp. 1405–1407, Jun 2005. doi: 10.1364/OL.30.001405

[84] A. Bartels and T. Dekorsy, "Terahertz-spektroskopie mit high-speed asops (thz spectroscopy based on high-speed asops):," *tm - Technisches Messen*, vol. 75, no. 1, pp. 23–30, 2008. doi: 10.1524/teme.2008.0845

[85] O. Kliebisch, D. C. Heinecke, and T. Dekorsy, "Ultrafast time-domain spectroscopy system using 10 ghz asynchronous optical sampling with 100 khz scan rate," *Opt. Express*, vol. 24, no. 26, pp. 29 930–29 940, Dec 2016. doi: 10.1364/OE.24.029930

[86] R. D. Baker, N. T. Yardimci, Y.-H. Ou, K. Kieu, and M. Jarrahi, "Self-triggered asynchronous optical sampling terahertz spectroscopy using a bidirectional mode-locked fiber laser," *Scientific Reports*, vol. 8, no. 1, p. 14802, Oct 2018. doi: 10.1038/s41598-018-33152-0

[87] Y. Kim and D.-S. Yee, "High-speed terahertz time-domain spectroscopy based on electronically controlled optical sampling," *Opt. Lett.*, vol. 35, no. 22, pp. 3715–3717, Nov 2010. doi: 10.1364/OL.35.003715

[88] J. Liu, M. K. Mbonye, R. Mendis, and D. M. Mittleman, "Measurement of terahertz pulses using electronically controlled optical sampling (ecops)," in *Conference on Lasers and Electro-Optics 2010*. Optical Society of America, 2010. doi: 10.1364/CLEO.2010.JWA107

[89] T. Hochrein, R. Wilk, M. Mei, R. Holzwarth, N. Krumbholz, and M. Koch, "Optical sampling by laser cavity tuning," *Opt. Express*, vol. 18, no. 2, pp. 1613–1617, Jan 2010. doi: 10.1364/OE.18.001613

[90] R. Wilk, T. Hochrein, M. Koch, M. Mei, and R. Holzwarth, "Oscat: Novel technique for time-resolved experiments without moveable optical delay lines," *Journal of Infrared, Millimeter, and Terahertz Waves*, vol. 32, no. 5, pp. 596–602, May 2011. doi: 10.1007/s10762-010-9670-8

[91] ——, "Terahertz spectrometer operation by laser repetition frequency tuning," *J. Opt. Soc. Am. B*, vol. 28, no. 4, pp. 592–595, Apr 2011. doi: 10.1364/JOSAB.28.000592

[92] M. Kolano, B. Gräf, S. Weber, D. Molter, and G. von Freymann, "Single-laser polarization-controlled optical sampling system for thz-tds," *Opt. Lett.*, vol. 43, no. 6, pp. 1351–1354, Mar 2018. doi: 10.1364/OL.43.001351

[93] M. Tani, S. Matsuura, K. Sakai, and M. Hangyo, "Multiple-frequency generation of sub-terahertz radiation by multimode ld excitation of photoconductive antenna," *IEEE Microwave and Guided Wave Letters*, vol. 7, no. 9, pp. 282–284, Sep. 1997. doi: 10.1109/75.622540

[94] O. Morikawa, M. Tonouchi, and M. Hangyo, "Sub-thz spectroscopic system using a multimode laser diode and photoconductive antenna," *Applied Physics Letters*, vol. 75, no. 24, pp. 3772–3774, 1999. doi: 10.1063/1.125451

[95] ——, "A cross-correlation spectroscopy in subterahertz region using an incoherent light source," *Applied Physics Letters*, vol. 76, no. 12, pp. 1519–1521, 2000. doi: 10.1063/1.126082

[96] O. Morikawa, M. Fujita, and M. Hangyo, "Improvement of signal-to-noise ratio of a subterahertz spectrometer using a continuous-wave multimode laser diode by single-mode fiber optics," *Applied Physics Letters*, vol. 85, no. 6, pp. 881–883, 2004. doi: 10.1063/1.1777800

[97] M. Scheller and M. Koch, "Terahertz quasi time domain spectroscopy," *Opt. Express*, vol. 17, no. 20, pp. 17 723–17 733, Sep 2009. doi: 10.1364/OE.17.017723

[98] R. B. Kohlhaas, A. Rehn, S. Nellen, M. Koch, M. Schell, R. J. B. Dietz, and J. C. Balzer, "Terahertz quasi time-domain spectroscopy based on telecom technology for 1550 nm," *Opt. Express*, vol. 25, no. 11, pp. 12 851–12 859, May 2017. doi: 10.1364/OE.25.012851

[99] A. Rehn, M. Mikerov, S. Preu, M. Koch, and J. C. Balzer, "Enhancing the performance of thz quasi time-domain spectroscopy systems by low duty cycle laser operation," *Opt. Express*, vol. 26, no. 25, pp. 32 758–32 764, Dec 2018. doi: 10.1364/OE.26.032758

[100] A. Rehn, R. Kohlhaas, B. Globisch, and J. C. Balzer, "Increasing the thz-qtds bandwidth from 1.7 to 2.5 thz through optical feedback," *Journal of Infrared,*

Millimeter, and Terahertz Waves, vol. 40, no. 11, pp. 1103–1113, Dec 2019. doi: 10.1007/s10762-019-00630-z

[101] D. Molter, M. Kolano, and G. von Freymann, "Terahertz cross-correlation spectroscopy driven by incoherent light from a superluminescent diode," *Opt. Express*, vol. 27, no. 9, pp. 12 659–12 665, Apr 2019. doi: 10.1364/OE.27.012659

[102] K. A. Williams, M. G. Thompson, and I. H. White, "Long-wavelength monolithic mode-locked diode lasers," *New Journal of Physics*, vol. 6, pp. 179–179, nov 2004. doi: 10.1088/1367-2630/6/1/179

[103] E. U. Rafailov, M. A. Cataluna, and W. Sibbett, "Mode-locked quantum-dot lasers," *Nature Photonics*, vol. 1, no. 7, pp. 395–401, Jul 2007. doi: 10.1038/nphoton.2007.120

[104] J. Renaudier, R. Brenot, B. Dagens, F. Lelarge, B. Rousseau, F. Poingt, O. Legouezigou, F. Pommereau, A. Accard, P. Gallion, and G.-H. Duan, "45 ghz self-pulsation with narrow linewidth in quantum dot fabry-perot semiconductor lasers at 1.5 μm," *Electronics Letters*, vol. 41, pp. 1007 – 1008, 10 2005. doi: 10.1049/el:20052173

[105] R. Rosales, K. Merghem, A. Martinez, A. Akrout, J.-P. Tourrenc, A. Accard, F. Lelarge, and A. Ramdane, "Inas/inp quantum-dot passively mode-locked lasers for 1.55-mum applications," *IEEE Journal of Selected Topics in Quantum Electronics*, vol. 17, no. 5, pp. 1292–1301, 2011. doi: 10.1109/JSTQE.2011.2116772

[106] R. Rosales, S. G. Murdoch, R. Watts, K. Merghem, A. Martinez, F. Lelarge, A. Accard, L. P. Barry, and A. Ramdane, "High performance mode locking characteristics of single section quantum dash lasers," *Opt. Express*, vol. 20, no. 8, pp. 8649–8657, Apr 2012. doi: 10.1364/OE.20.008649

[107] K. Merghem, S. F. Busch, F. Lelarge, M. Koch, A. Ramdane, and J. C. Balzer, "Terahertz time-domain spectroscopy system driven by a monolithic semiconductor laser," *Journal of Infrared, Millimeter, and Terahertz Waves*, vol. 38, no. 8, pp. 958–962, Aug 2017. doi: 10.1007/s10762-017-0401-2

[108] S. P. O. Duill, S. G. Murdoch, R. T. Watts, R. Rosales, A. Ramdane, P. Landais, and L. P. Barry, "Simple dispersion estimate for single-section quantum-dash and

quantum-dot mode-locked laser diodes," *Opt. Lett.*, vol. 41, no. 24, pp. 5676–5679, Dec 2016. doi: 10.1364/OL.41.005676

[109] D. A. Reid, S. G. Murdoch, and L. P. Barry, "Stepped-heterodyne optical complex spectrum analyzer." *Opt. Express*, vol. 18, no. 19, pp. 19 724–19 731, Sep 2010. doi: 10.1364/OE.18.019724

[110] L. Mandel and E. Wolf, "The measures of bandwidth and coherence time in optics," in *Proceedings of the Physical Society*, vol. 80, no. 4. IOP Publishing, oct 1962. doi: 10.1088/0370-1328/80/4/311

[111] A. Reisinger, C. David, K. Lawley, and A. Yariv, "Coherence of a room-temperature cw gaas/gaalas injection laser," *IEEE Journal of Quantum Electronics*, vol. 15, no. 12, pp. 1382–1387, 1979. doi: 10.1109/JQE.1979.1069944

[112] D. Jahn, S. Lippert, M. Bisi, L. Oberto, J. C. Balzer, and M. Koch, "On the influence of delay line uncertainty in thz time-domain spectroscopy," *Journal of Infrared, Millimeter, and Terahertz Waves*, vol. 37, no. 6, pp. 605–613, Jun 2016. doi: 10.1007/s10762-016-0250-4

[113] A. Rehn, D. Jahn, J. C. Balzer, and M. Koch, "Periodic sampling errors in terahertz time-domain measurements," *Opt. Express*, vol. 25, no. 6, pp. 6712–6724, Mar 2017. doi: 10.1364/OE.25.006712

[114] D. Molter, M. Trierweiler, F. Ellrich, J. Jonuscheit, and G. V. Freymann, "Interferometry-aided terahertz time-domain spectroscopy," *Opt. Express*, vol. 25, no. 7, pp. 7547–7558, Apr 2017. doi: 10.1364/OE.25.007547

[115] S. Takagi, S. Takahashi, K. Takeya, and S. R. Tripathi, "Influence of delay stage positioning error on signal-to-noise ratio, dynamic range, and bandwidth of terahertz time-domain spectroscopy," *Appl. Opt.*, vol. 59, no. 3, pp. 841–845, Jan 2020. doi: 10.1364/AO.378756

[116] C. A. Balanis, "Antenna theory : analysis and design," Hoboken, NJ, 2005.

[117] A. Rivera-Lavado, L. E. García-Muñoz, G. Dohler, S. Malzer, S. Preu, S. Bauerschmidt, J. Montero-de Paz, E. Ugarte-Muñoz, B. Andrés-García, V. Izquierdo-Bermúdez, and D. Segovia-Vargas, "Arrays and new antenna topologies for increasing thz power generation using photomixers," *Journal of Infrared, Millimeter,*

and Terahertz Waves, vol. 34, no. 2, pp. 97–108, Feb 2013. doi: 10.1007/s10762-013-9954-x

[118] R. Reese, E. Polat, H. Tesmer, J. Strobl, C. Schuster, M. Nickel, A. B. Granja, R. Jakoby, and H. Maune, "Liquid crystal based dielectric waveguide phase shifters for phased arrays at w-band," *IEEE Access*, vol. 7, pp. 127 032–127 041, 2019. doi: 10.1109/ACCESS.2019.2939648

[119] P.-Y. Chen, C. Argyropoulos, and A. Alù, "Terahertz antenna phase shifters using integrally-gated graphene transmission-lines," *IEEE Transactions on Antennas and Propagation*, vol. 61, no. 4, pp. 1528–1537, 2013. doi: 10.1109/TAP.2012.2220327

[120] A. Moffet, "Minimum-redundancy linear arrays," *IEEE Transactions on Antennas and Propagation*, vol. 16, no. 2, pp. 172–175, 1968. doi: 10.1109/TAP.1968.1139138

[121] M. Ishiguro, "Minimum redundancy linear arrays for a large number of antennas," *Radio Science*, vol. 15, no. 06, pp. 1163–1170, 1980. doi: 10.1029/RS015i006p01163

[122] C. Chambers, T. C. Tozer, K. C. Sharman, and T. S. Durrani, "Temporal and spatial sampling influence on the estimates of superimposed narrowband signals: when less can mean more," *IEEE Transactions on Signal Processing*, vol. 44, no. 12, pp. 3085–3098, 1996. doi: 10.1109/78.553482

[123] D. King, R. Packard, and R. Thomas, "Unequally-spaced, broad-band antenna arrays," *IRE Transactions on Antennas and Propagation*, vol. 8, no. 4, pp. 380–384, 1960. doi: 10.1109/TAP.1960.1144876

[124] A. Ishimaru and Y. . Chen, "Thinning and broadbanding antenna arrays by unequal spacings," *IEEE Transactions on Antennas and Propagation*, vol. 13, no. 1, pp. 34–42, 1965. doi: 10.1109/TAP.1965.1138378

[125] J. Robinson and A. Bernstein, "A class of binary recurrent codes with limited error propagation," *IEEE Transactions on Information Theory*, vol. 13, no. 1, pp. 106–113, 1967. doi: 10.1109/TIT.1967.1053951

[126] M. Gardner, "Mathematical games," *Scientific American*, vol. 226, no. 6, pp. 114–121, 1972.

[127] A. Sheikholeslami and Z. Atlasbaf, "Novel phase distributions for large electronically beam-scanning reflectarrays," *Scientific Reports*, vol. 11, no. 1, p. 21877, Nov 2021. doi: 10.1038/s41598-021-00883-6

DOI: 10.17185/duepublico/76092
URN: urn:nbn:de:hbz:465-20220624-150041-4